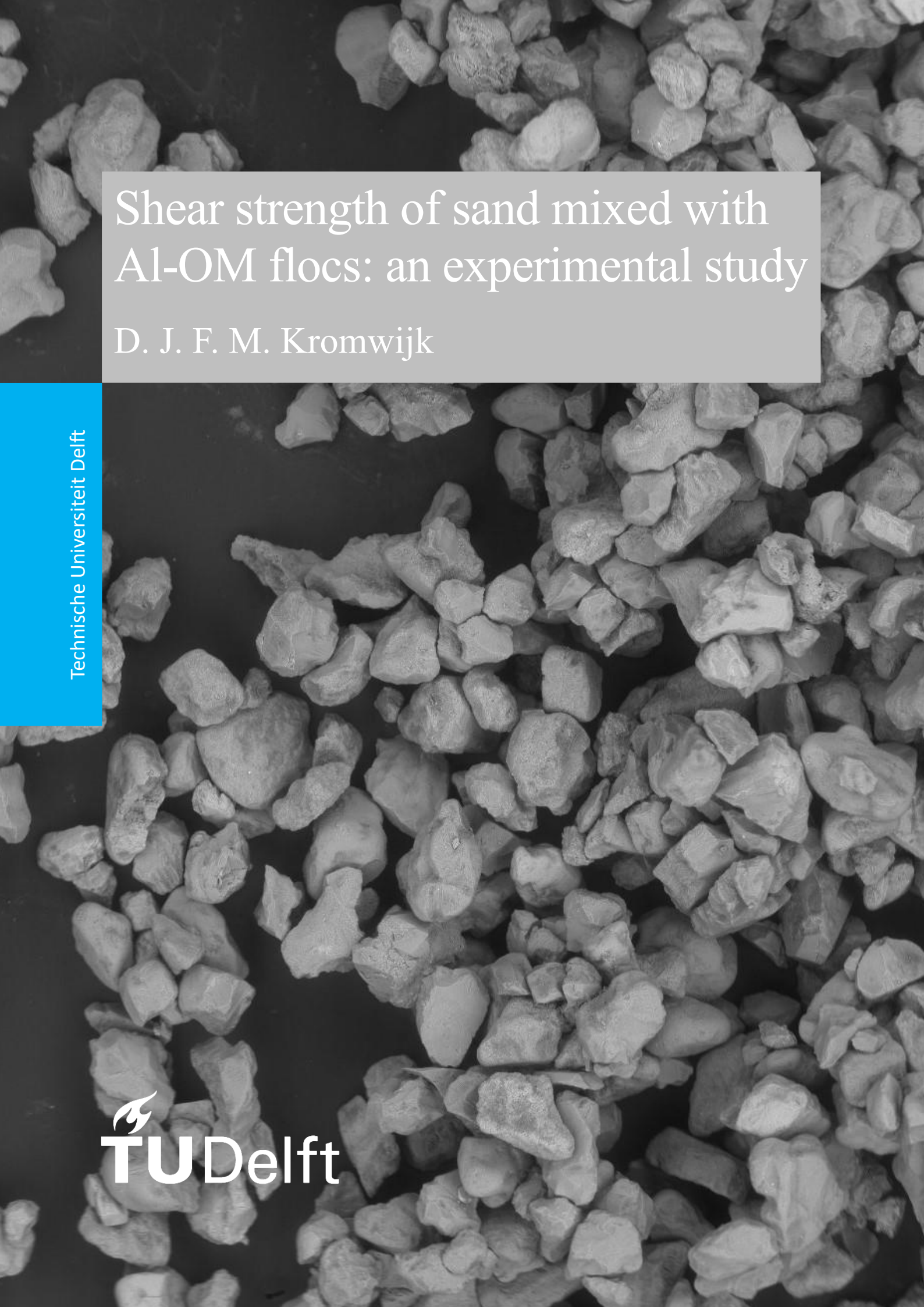

Shear strength of sand mixed with Al-OM flocs: an experimental study

D. J. F. M. Kromwijk

Technische Universiteit Delft

TU Delft

Shear strength of sand mixed with Al-OM flocs: an experimental study

by

D. J. F. M. Kromwijk
Student number: 4651790

In partial fulfillment of the requirements for the degree of

Master of Science
In Civil Engineering (Geo-Engineering track)
Faculty of Civil Engineering and Geosciences
Delft University of Technology

To be defended publicly on Tuesday January 16, 2024 at 13:30 AM.

Thesis committee:

Dr.ir. A.C. Dieudonné	TU Delft, supervisor
Prof.dr.ir. T. J. Heimovaara	TU Delft
Dr. J. P. Aguilar-López	TU Delft

TU Delft

Abstract

The integration of biological and (bio-)geochemical processes in soils is posed to become the next transformative practice in geotechnical engineering. Soil Sealing by Enhanced Aluminium and dissolved organic matter Leaching, also known as SoSEAL, is inspired by a natural soil formation process, called Podzolization. This process results in the formation of a nearly impermeable spodic B-horizon. A similar low-permeable layer is made by SoSEAL. The products of the chemical reaction between aluminium and organic matter generates organic precipitation, clogging the pore throats between sand grains. Past research on SoSEAL has primarily centered on its application as a low-permeable water retaining barrier used for dyke improvement. However, the broader impact of SoSEAL on the mechanical properties of soils beyond permeability remains largely unexplored.

Despite progress, gaps persist in understanding SoSEAL's influence on sand's mechanical properties, particularly on the shear strength. The primary objective in this research was to investigate the impact of different concentrations of Al-OM (Aluminum and Organic Matter) flocs on sand's mechanical characteristics through ex-situ mixing. This included the development of a testing procedure using a triaxial test apparatus, incorporating results from permeability tests and utilizing microscopy to analyze micro structural changes and the underlying mechanisms. The study aimed to deliver valuable insights into SoSEAL's potential as a nature-inspired geo-engineering solution for soil improvement.

Undrained triaxial tests were conducted on ex-situ mixed sand with different concentrations of Al-OM flocs, namely 0, 0.1, 0.5 and 1%. These concentrations were defined as dry mass of flocs based on a metal/carbon ratio of 0.06. Through a carefully executed test procedure, involving Proctor's test, permeability measurements and triaxial testing, the mechanical properties of the treated sand were investigated. Proctor's tests were utilized to determine the maximum dry density and its corresponding moisture content of the (un)treated sand. These parameters were used for molding the sand samples for the triaxial test series. The untreated sand did not show a clear peak in its Proctor curve, which is typical for uniform graded fine/medium sands. The porosities, derived from the optimum dry density and corresponding water content, were found to be ≈ 0.4 (-) for all samples. Indicating the minor impact of the Al-OM flocs to the porosity of the sand samples.

The undrained consolidated triaxial test procedure, consisting of saturation, consolidation, and shearing, provided insights into the mechanical properties of SoSEAL. Although the consolidation phase did not reveal significant differences in the presence of Al-OM flocs, elastic parameters, derived from the shearing phase, generally increased with higher Al-OM floc concentrations in sand. Young's Modulus, E, increased by a magnitude between 2.11-2.62 times the untreated sand, while the shear Modulus, G, increased by a magnitude between 2.09-2.18. Nonetheless, exceptions such as test CU05-1 and CU10-2 were observed. Strength parameters, measured by maximum deviatoric stress at failure, exhibited an overall increase with higher floc concentrations. Finally, the results show that an alteration in floc concentration in sand did not have a significant impact on its permeability, contrary to previous measurements obtained in the absence of confinement.

The results from the Proctor's test, permeability measurements and the triaxial tests highlighted differences and improved general knowledge of the impact of Al-OM flocs to the mechanical properties of sand. Variations in test results, seen when comparing test CU05-1 to CU05-2 and test CU10-1 to CU10-2, underscored the complexity of factors such as compaction challenges and localized failures. From microscale examination using scanning electron miscroscopy (SEM), the increase in strength properties can be attributed to the cohesion between sand grains, evident in the formation of grain clusters. As the concentration of Al-OM flocs in sands increased, so did the quantity of grain clusters. The potential of Al-OM flocs in sand for dyke improvement is found in the observed increase in elastic and strength properties, providing enhanced resistance against erosion.

Acknowledgement

I would like to express my gratitude to my thesis advisor, Anne-Catherine Dieudonné, for her guidance and invaluable insights throughout the entire process of conducting this research. Her expertise and encouragement played a crucial role in shaping the direction and quality of this thesis. Special appreciation goes to Cristina Cavero Panez for her technical guidance in the lab. She not only taught me the intricacies of utilizing the triaxial test apparatus, but also helped me navigate through the best approach in handling SoSEAL within this apparatus. Additionally, I extend my gratitude to Arjan Thijssen for his invaluable assistance in capturing captivating images of SoSEAL using the SEM. I would also like to extend my appreciation to all the other staff in the lab for their genuine interest and willingness to always lend a helping hand when needed. Their collective effort have fostered a collaborative and supportive atmosphere.

I am grateful towards the examination committee, including Timo Heimovaara, whose boundless knowledge and passion for the subject have been inspiring. And Juan Aguilar-López for his insightful, business-minded perspective. My gratitude extends to the entire committee for dedicating their time to evaluate this document and the interesting meetings and insights.

Finally, a heartfelt thank you to my family and friends, whose support, through laughter and kindness, kept me going through the entire process.

Delft, January 2024
Dominique Kromwijk

Contents

Nomenclature

Abbreviations

Al	Aluminium
BEP	Backward Erosion Piping
C	Carbon
Cl	Chloride
CU	Consolidated Undrained
DOM	Dissolved Organic Matter
Fe	Iron
GDS	Global Digital Systems
H	Hydrogen
HA	Humic Acid
HDSR	Hoogheemraadschap de Stichtse Rijnlanden
K	Kalium
M/C	Molar Metal to Carbon
Mg	Magnesium
MICP	Microbially Induced Calcite Precipitation
N	Nitrogen
OM	Organic Matter
OMC	Optimum Moisture Content
rpm	Rotation per minute
S	Sulfur
SEM	Scanning Electron Microscopy
Si	Silica
SoSEAL	Soil Sealing by Enhanced Aluminium and DOM leaching

Symbols

ν	Poisson's ratio
ϕ	Friction angle
σ_1	Major principal stress

σ_2	Intermediate principal stress
σ_3	Minor principal stress
σ_n	Normal stress
τ	Shear strength
τ_f	Shearing resistance
A	Cross-sectional area
B	Pore pressure coefficient
c	Cohesion
C_c	Coefficient of Curvature
E	Young's Modulus
e	Voids ratio
F	Force
G	Shear Modulus
G	Specific gravity
h	Head
H+	Proton
i	Mean hydraulic gradient
k_v	Hydraulic conductivity in vertical direction
L	Length
n	Porosity
p	Pressure
p'	Cambridge effective stress
Q	Discharge
q	Deviatoric stress
q	Rate of flow
t	Time
u	Pore pressure

List of Figures

List of Tables

1

Introduction

The field of geotechnical engineering has advanced steadily throughout history. The origins of the discipline can be traced back to Coulomb's influential work on earth pressures in 1776. This marked the formal beginning of the field, which was followed by subsequent progress in mechanics and water flow, with significant contributions including Darcy's law (1857) and Mohr's circle of strain (1885). The discipline experienced a transformative shift with the pioneering work of Karl Terzahgi in the 1920s, particularly in the development of the principle of effective stress and analyses related to foundation bearing capacity and soil consolidation. The ongoing work of many others have continued to evolve the domain of geotechnical engineering.

1.1. From traditional to nature-inspired geotechnical engineering

Utilizing biological processes in soils is poised to become the next transformative practice in the field of engineering. The influence of chemical processes that are mediated by biology are more broadly exploited. An example is plant roots' influence on slope stability, which has been acknowledged and exploited for numerous years (Dejong et al., 2013). The method of bio-inspired design begins by abstracting a biological solution, wherein a specific biological strategy is identified. Subsequently, the principle of the strategy is extracted, and the solution is reframed to ease its translation to the engineering domain (Martinez et al. 2022). The byproducts produced by these biological processes modify the engineering properties of soil. The processes can be broadly categorized into (*a*) inorganic precipitation, (*b*) organic precipitation and (*c*) gas generation. The byproducts can be considered as biomineralization, biofilm formation and biogas generation, respectively (DeJong et al., 2010). An overview is shown in Figure 1.1.

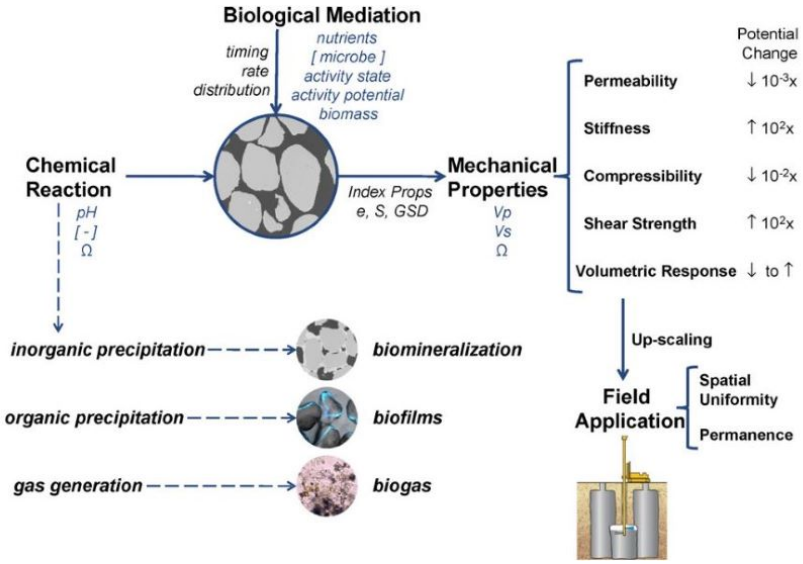

Figure 1.1: Overview of bio-mediated soil improvement systems (DeJong et al., 2010).

In the context of bio-geotechnical engineering, numerous studies have been carried out in the past years. Some biological techniques have been successfully implemented, while others are still being explored. An example is microbially induced calcite precipitation (MICP), in which biogeochemical processes induce carbonate precipitation and cement soil grains, consequently enhancing the mechanical properties of the material such as stiffness and strength. (Zhang and Dieudonné, 2023). This instance, showcases the potential benefits that bio-inspired design has to offer. However, the difference between the natural and engineered environments in terms of spatial and temporal scales and materials can be significant and must be taken into account. The improvement in soil properties cannot be achieved unless the byproducts are spatially located within the specific region of the soil matrix required to affect the soil behavior (Zhang and Dieudonné, 2023). In addition, biological strategies are often complex due to the multi-functionality and adaptability of these processes. Therefore, biological-inspired soil improvement practices require careful evaluation before it can be implemented to develop geotechnical solutions.

1.2. SoSEAL

In this study, a noval approach for soil improvement is explored. The SoSEAL project is meant to develop a new nature-inspired geo-engineering technology to reduce the permeability of soil layers. SoSEAL stands for Soil Sealing by Enhanced Aluminium and Dissolved Organic Matter (DOM) leaching. The technology is inspired by the natural soil formation process Podzolization, which leads to the formation of a nearly impermeable spodic B-horizon. While there is still a lot of ongoing research to the formation of this horizon, it is widely accepted that it is caused by the complexation of organic matter (OM) with polyvalent metals like iron (Fe) or aluminium (Al), followed by the precipitation of these organo-metallic complexes at deeper levels of the soil profile (Zhou et al., 2018). This phenomenon is typically seen in coniferous forests. The progressive accumulation of the Al/Fe complexes ultimately causes a reduction in permeability (Lundström et al., 2000). Other mechanical properties can also be affected by metal-OM interactions. For instance, during Podzolization, the localised precipitation and accumulation of organo-metallic precipitates result in a distinct soil horizon that is notably stiffer (Sauer et al., 2007).

1.2.1. Principles

The idea of the SoSEAL technology is to form a low-permeability barrier by precipitating aluminium (Al) and dissolved organic matter (DOM). Aluminum and organic matter chemically interact with each other, forming flocs that tend to precipitate. These precipitates subsequently clog the pore space or pore throat between sand grains, resulting in a decrease in permeability of this porous medium (Zhou et al., 2018).

The first SoSEAL project aimed to reduce the infiltration loss or the seepage burden caused by flow of water through highly permeable layers in the subsurface (NwO, 2014). This project endured till January 2020 and is referred to as SoSEAL-1. Since its initiation, scientific research has been done exploring the concept. Within the framework, Popma (2017) studied the mixing process of OM and Al and found that 85% of the organic matter is able to form precipitates by binding aluminium ions. Other investigations were primarily focused on the efficacy of SoSEAL to permeability reduction. In particular, within the initial SoSEAL project, the technology was applied in two field-scale tests in which different approaches for applying Al-OM complexes to reduce soil permeability were examined. In the first test, Al and OM solutions were mixed in-situ, this indicated a creation of a vertical flow barrier reducing the permeability of the sand by 2% of its original value (Zhou et al., 2019). The second field experiment, using direct injection of Al-OM flocs, also revealed significant reduction of permeability. However, the precipitation had a high spatial variability, from which the exact magnitude of reduction could not be determined. Experimental laboratory research explored several factors influencing the hydraulic conductivity reduction (Bonfiglio, 2017, Sanna, 2020, Kaptein, 2021). In particular, Sanna (2020) examined the relation between the injection flow rate and the hydraulic conductivity reduction, showing that an increase in the flow rate implies an increase in Al-OM floc transport. On the other hand, Bonfiglio (2017) investigated the influence of the used porous media. Furthermore, the concept of critical metal-carbon (M/C) ratio has been explored. From the titration curve it was found that a critical M/C ratio to be able to form flocs is between 0.023- 0.031 (Kaptein, 2021).

1.2.2. Potential to mitigate backward erosion piping (BEP)

Following SoSEAL-1, since 2022, the potential of SoSEAL barriers to mitigate Backward Erosion Piping (BEP) has been investigated. This is referred to as SoSEAL-2. Backward erosion piping is an internal erosion mechanism in which pipes are formed underneath a water-retaining structure as a result of removal of soil by the action of water. Initially, driven by

a hydraulic head gradient, water flows through porous media below the dyke and flows out at an exit caused by a defect in an overlying low-permeability cohesive layer (*initiation*). If the water flow into the exit is great enough, dislocated sand particles can be transported away from the exit. The particles are removed, and the soil is fluidized, transporting eroded particles to the surface where they are deposited (*progression*). The formed pipe can lengthen towards the upstream side of the dyke and, when it reaches this, fast water flow causes deepening and widening of the pipes (*continuation*). Eventually, a dyke breach forms due to macro instability of the dyke (*breach*). The different phases involved are depicted in Figure 1.2 (Beek, 2015). This failure mechanism cannot exist without the following conditions: an exit is required where the dislocated sand can be deposited; the hydraulic gradient should be large enough to induce sand erosion and thus overcome a certain shear strength between sand particles; lastly, a low-permeability cohesive layer must exist to prevent the collapse of the formed pipe and cause a concentration of flow lines near the exit. With this knowledge, engineering solutions to eliminate one or more of these conditions can be formed.

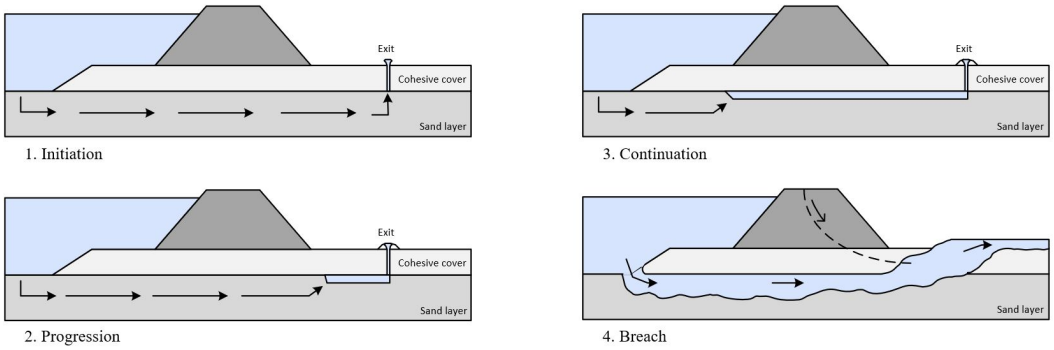

Figure 1.2: Backward erosion piping inducing dyke breach (Semmens and Zhou, 2021).

In the Netherlands, the geology near rivers is typically characterized by alluvial deposits overlying older strata. This results in a highly heterogeneous subsurface near river systems, featuring alternating deposits of clay, sand or silt which are intersected by old river channels (Fookes, 1997). Dykes, built near river beds, are commonly constructed from local impermeable materials. In the Western part of the Netherlands, Holocene layers of alluvial deposits often overlay and generally conceal a Pleistocene sandy layer extending to a considerable depth. Moreover, in coastal regions and the eastern part of the country, man-made dykes are directly built upon sand layers (Beek, 2015). The situation in which a cohesive top layer is overlying a sandy aquifer, or a cohesive clay dyke is located directly on a sandy aquifer, is therefore very common in the Netherlands. Hence, there is significant interest in implementing mitigation measures for the BEP failure mechanism.

1.3. Scope and objectives

With the past research, the focus has been on using SoSEAL as a low-permeability water-retaining barrier, in which the pipe development is hindered by the decrease in flow rate by lengthening the flow path. However, much is still unknown regarding the influence of SoSEAL to other mechanical properties of sand, such as strength. The strength of soil is typically defined as resistance to shear stress in terms of the effective internal friction angle and effective cohesion. If the use SoSEAL would increase the strength properties of sand, this can have great influence on the design criteria for using SoSEAL as a dyke improvement measure. Since an increase in strength would indicate a better resistance against erosion and thus against BEP, it can prevent an overestimation of design parameters. Alternatively, if SoSEAL would show an increase in cohesion compared to the non-cohesive sand, SoSEAL can also infer to the other condition which is needed for the BEP failure mechanism. Namely, a non-cohesive soil covered by a low-permeability cohesive soil. Granting that the treated sand shows cohesive characteristics, it would eliminate this condition, because the sand would no longer be non-cohesive. Therefore, this research will be focused on how the strength properties of sand are altered as a response of the formation of aluminum-organic matter precipitates. By experimentally testing samples with the triaxial test setup, the following research question will be answered:

How do different concentrations of Al-OM flocs impact the mechanical characteristics of sand when ex-situ mixed?

In order to answer the research question, the following subquestions are formulated:

- What are the steps involved in developing a test procedure for evaluating the mechanical properties of sand using a triaxial test apparatus?

- How can permeability measurements be incorporated into the test procedure?
- How does microscopy contribute in analyzing the micro structural changes and illustrate the mechanisms driving these observations?

As previously mentioned, the assessment of the response of Al-OM flocs in sand to shear involves the utilization of the triaxial test apparatus. In Chapter 2 the theory behind soil under compression is outlined and the triaxial test, with its different stages involved, is clarified. Subsequently, Chapter 3 provides insights into the interaction between aluminium and organic matter. In Chapter 4 the material properties of the sand and chemicals used in the experiments are described, followed by the sample preparation. Then, the experimental setup is elaborated in Chapter 5 and the results are analysed in Chapter 6. Subsequently, a thorough discussion is presented in Chapter 7. Finally, Chapter 8 highlights conclusions and recommendations fur further research.

2

Theoretical background

A soil response to loading is a complicated matter as it depends on a variety of factors such as initial stress state and load distribution. In this study, the triaxial test is utilized to examine soil behaviour under a specifically prescribed load. This Chapter begins with an elaboration on the overarching theory of soil under compression (Section 2.1). The concept of shear strength will be explained and a derivation of Mohr's circle of stress is given (Section 2.2). This circle becomes instrumental for the derivation of different shear strength parameters later on. Subsequently, in Section 2.3 the triaxial test is explained, expounding on its principles and various stages involved. The following Sections delve into the derivation of elastic parameters from the output of the triaxial test (Section 2.3.1 and 2.3.2).

Finally, it is necessary to analyse the influence of Al-OM flocs added to sand. Chapter 3 presents a literature review on the interaction between aluminium and organic matter (Al-OM). This review aims to enhance understanding of how the combination of sand and Al-OM flocs, known as SoSEAL, responds to compression differently than untreated sand.

2.1. Soil under compression

In Figure 2.1 a potential failure mechanism in an embankment is considered, indicated by the circle. The embankment is thought to be long in the out-of-plane direction, such that the situation can be regarded as plane strain. In the potential failure mechanism different modes of shearing can be observed (Brinkgreve, 2021):

1. In the sub-soil, in front of the toe of the embankment, a passive stress state emerges as the horizontal stress increases while the vertical stress remains constant. This stress development shares similarities with what is known as triaxial extension.
2. In the sub-soil beneath the embankment slope, a stress progression occurs that resembles simple shear, wherein the shear stress undergoes development without substantial changes in the vertical and horizontal stresses.
3. An active stress state emerges withing the sub-soil, positioned just behind the crest of the embankment. Here, the vertical stress increases while the lateral stress largely remains constant. This stress development is similar to the conditions observed in triaxial compression.

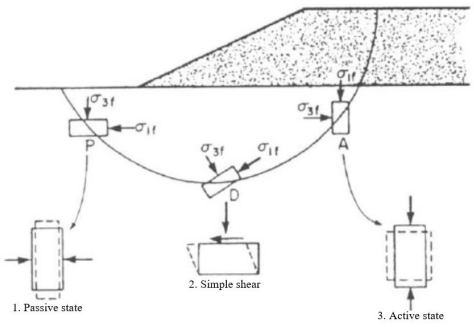

Figure 2.1: Different modes of shearing along a potential failure mechanism (Brinkgreve, 2021).

This research will be focused on the third shearing mode; an active stress state which is similar to the conditions observed in triaxial compression. Since SoSEAL will eventually be used in dykes to prevent piping and thus to enhance bank stability in the long term, triaxial tests can govern valuable information about the response of SoSEAL to a prescribed load.

2.1.1. Shear strength of sands

A theoretical foundation is required for comprehending the principles behind the triaxial test. Some basic concepts like force, stress, strain and shearing resistance are assumed to be prior knowledge and essential for understanding the procedure. With the use of Coulomb's equation, which relates shear strength to normal stress, the theory of shear strength in soils, with special attention to sands, is explained. However, it should be kept in mind that shear strength is not a fundamental property of a soil, but is related to the conditions prevailing in situ and can very with time. Therefore, the value for shear strength measured in the laboratory is dependent upon the conditions imposed during the test.

In 1772 Coulomb suggested the general relationship between shearing resistance, τ_f, and normal stress, σ_n, for soils to be in the form:

$$\tau_f = c + \sigma_n \cdot \tan(\phi) \tag{2.1}$$

In which c is known as the cohesion and ϕ as the friction angle. Generally, the shear strength of a soil cannot be assumed to be governed by the total normal stress, but rather by effective stress. The normal effective stress, σ'_n, can be determined by subtracting the pore water pressure, u, from the total stress (Verruijt, 2001):

$$\sigma'_n = \sigma_n - u \tag{2.2}$$

Substituting this in the Coulomb equation gives:

$$\tau_f = c' + \sigma'_n \cdot \tan(\phi') \tag{2.3}$$

with:
c' = effective cohesion
ϕ'= effective angle of internal friction
τ_f = shear resistance
σ'_n = effective normal stress on the shear plane

From this equation it can be seen that the shearing resistance consists of two components: (1) friction, denoted by $\tan(\phi')$, due to the interlocking of particles and the friction between them when subjected to normal effective stress, (2) cohesion, denoted by c', due to internal forces holding particles together in a solid mass (Head, 1994).

2.2. Mohr's circle of stress

In this section the Mohr's circle of stress will be derived and an explanation of the Mohr-Coulomb failure envelope is given. While this stress circle is commonly associated with Otto Mohr (1882), it was Culmann (1866) who initially conceived this graphical method for representing stress (Parry, 2004). Mohr, on the other hand, made a significant contribution by extensively studying its application for both two-dimensional and three-dimensional stresses. Next to this, Mohr developed a strength criterion that was based on the stress circle concept (Parry, 2004). Before elaborating on the graphical representation of stress by the means of a circle, a good understanding of principal stresses is needed.

2.2.1. Principal stresses

In a cylindrical compression test, e.g. the triaxial test, a specimen is subjected to compressive stresses acting in three directions at right angles to each other. One stress will act in the axial direction while the other two stresses act laterally. The planes on which these three stresses act on are known as principal planes. These stresses are referred to as principal stresses (Head, 1994). There are no shear stresses on the planes where principal stresses occur. However, on planes inclined at angles other than 90° to the principal planes, the shear stresses are not zero, and the normal stresses differ from the principal stresses but never exceeds the largest (major principle stress) of them. On the other hand the normal stress is also never lower than the minor principal stress. The principal stresses can be categorized as follows:

- Major principal stress (σ_1)
- Intermediate principal stress (σ_2)
- Minor principal stress (σ_3)

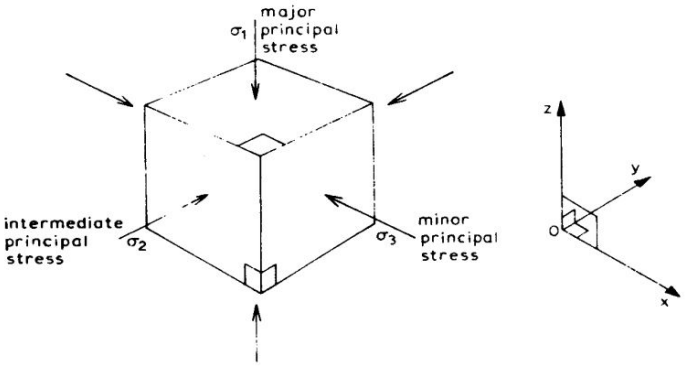

Figure 2.2: A graphical representation of principal stresses and principal planes (Head, 1994).

The stresses are given in order of descending magnitude and are shown acting on a cube in Figure 2.2. In most cases the major principle stress acts in the vertical direction and the minor and intermediate principle stresses act in horizontal direction perpendicular to each other (Figure 2.2). In the case of cylindrical compression, as used in the triaxial test setup, the intermediate and minor principal stresses are equal. This is referred to as axial symmetry.

2.2.2. Derivation of Mohr's circle

A simple axial two-dimensional stress situation is considered. When a cylindrical test specimen is subjected to an axial compressive force (F), as shown in Figure 2.3, the stresses on planes PQ and PR can be expressed. If the cross-sectional area (A), is known, the stress (σ_n), on plane PQ is given by:

$$\sigma_n = \frac{F}{A} \tag{2.4}$$

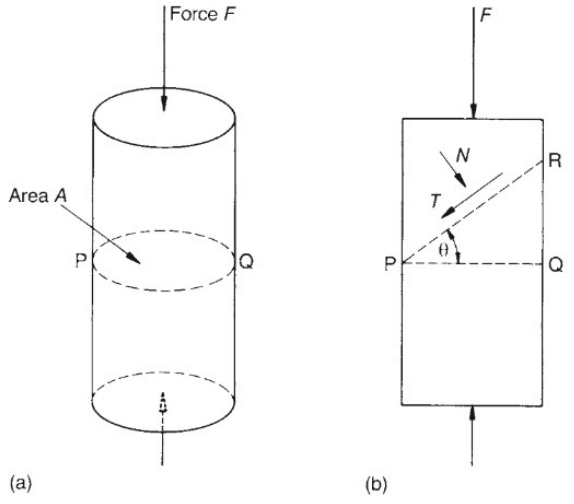

Figure 2.3: Cylindrical test specimen subjected to an axial force F (Parry, 2004).

Because σ_n is the only stress acting across plane PQ and is perpendicular to this plane, σ_n is a principal stress. Now, a plane labeled PR (Figure 2.3.b) is considered. The plane is positioned at an angle θ, relative to the radial planes on which σ_n works. The force F, can be divided into two components: N, which acts perpendicular (normal) to the plane, and T, which acts parallel to the plane in the direction of the steepest inclination (θ). Such that:

$$N = F \cdot \cos(\theta) \tag{2.5}$$

$$T = F \cdot \sin(\theta) \tag{2.6}$$

The area of the inclined plane PR is an ellipse with surface area equal to $A/\cos(\theta)$. The stress normal to the plane and the shear stress along the plane are then given by:

$$\sigma_{n_{PR}} = \frac{N}{\frac{A}{\cos(\theta)}} = \frac{F}{A} \cdot \cos^2(\theta) \tag{2.7}$$

$$\tau_{PR} = \frac{T}{\frac{A}{\cos(\theta)}} = \frac{F}{2A} \cdot \sin(2\theta) \tag{2.8}$$

The maximum value of the shear stress τ can be found by differentiating Equation 2.8 and setting it equal to zero:

$$\frac{d\tau}{d\theta} = \frac{F}{A} \cdot \cos(2\theta) \tag{2.9}$$

$$\frac{F}{A} \cdot \cos(2\theta) = 0 \tag{2.10}$$

From this Equation it can be concluded that the maximum shear stress τ_{max} is equal to $\frac{F}{2A}$ and occurs under an angle (θ) of 45° (Parry, 2004).

When a cylindrical specimen is not only subjected to a axial major principal stress (σ_1), but also a minor radial principal stress (σ_3), a biaxial stress system is considered. Such a diagram is shown in Figure 2.4. The stresses σ_n and τ on a plane inclined at an angle θ to the direction of the plane on which the major principal stress acts can be found be considering the forces acting on a triangular element as shown in Figure 2.4.b. When the triangular thickness is considered to be unity, the areas on which the stresses act are numerically equal to the lengths of the sides (Table 2.1). The forces acting on the three faces can then be obtained by multiplying the stress by the length of each wedge (Table 2.2).

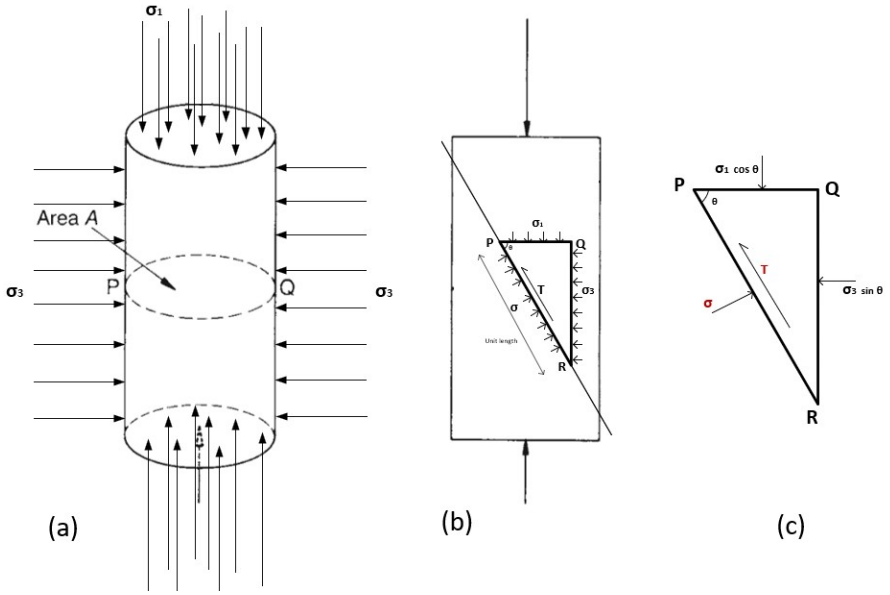

Figure 2.4: Stresses on a cylindrical sample subjected to triaxial compression: (a) external stress, (b) stresses on wedge element PQR, (c) forces on wedge element PQR.

Plane	*Normal stress*	*Shear stress*
PQ	σ_1	0
QR	σ_3	0
PR	σ	τ

Table 2.1: Stresses acting on wedge PQR.

Plane	*Normal force*	*tangential force*
PQ	$\sigma_1 \cdot \cos(\theta)$	0
QR	$\sigma_3 \cdot \sin(\theta)$	0
PR	σ	τ

Table 2.2: Forces acting on wedge PQR.

Because the wedge shown in Figure 2.4 is in equilibrium, the four forces listed in Table 2.2 must form a closed polygon, shown in red in Figure 2.5 (Head, 1994). The horizontal axis represents the normal stress σ and the vertical axis represents the shear stress τ. With this polygon the relationship between the four forces can be derived. The line OSQ is extended to point R to make the length SR equal to $\sigma_1 - \sigma_3$. The angle OVS is a 90° angle and therefore SV equals $\sigma_3 \cdot \cos(\theta)$ and OS equals σ_3. Furthermore, it can be proven that angle RPS must be a 90° angle, for any value of θ:

$$\begin{aligned} \mathrm{PS} &= \mathrm{PV} - \mathrm{SV} \\ &= \sigma_1 \cdot \cos(\theta) - \sigma_3 \cdot \cos(\theta) \\ &= (\sigma_1 - \sigma_3) \cdot \cos(\theta) \\ &= \mathrm{SR} \cdot \cos(\theta) \\ \frac{\mathrm{PS}}{\mathrm{SR}} &= \cos(\theta) \end{aligned} \tag{2.11}$$

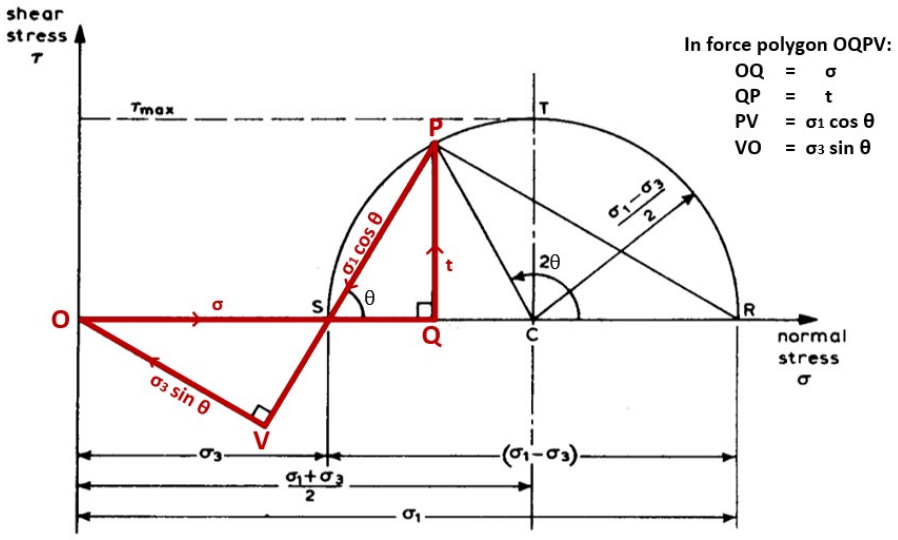

Figure 2.5: Polygon of forces for triaxial compression displayed on Mohr's circle of stress (Head, 1994).

Hence point P must always lie on a circle with diameter SR for any value of θ. The circle intersects the horizontal axis at σ_3 and σ_1, respectively. Therefore, in a specimen experiencing unequal compressive stresses σ_1 and σ_3 acting vertically and horizontally, the stresses on a plane inclined at any angle θ to the horizontal can be determined through graphical analysis. This is known as the Mohr circle of stress which was discovered by Culmann (1866) and developed in detail by Mohr (1882).

When a series of compression tests at different confining pressures is carried out on similar soil samples, the Mohr-Coulomb failure envelope can be drawn (Figure 2.6). This is a tangential line to the Mohr circles at different confining pressures representing failure (Head, 1994). If a Mohr circle corresponding to a specific state of stress in a soil is entirely positioned below the Mohr envelope, it indicates that the soil is in a stable condition. When the Mohr circle touches the envelope, it signifies that the soil has reached its maximum strength, indicating failure has occurred on a particular plane within the specimen. However, a circle intersecting the Mohr envelope and rising above it holds no physical significance because once the envelope is reached, failure occurs and the soil can no longer provide additional shear resistance.

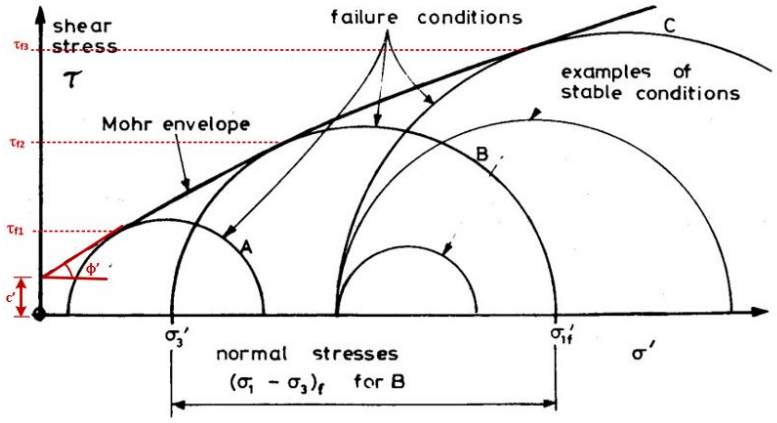

Figure 2.6: Mohr circles and the Mohr-Coulomb failure envelope (Head, 1994).

The Mohr envelope can be used to derive the effective shear strength parameters including cohesion (c') and friction angle (ϕ'). The cohesion is defined as the intersect between the Mohr envelope and the y-axis and the friction angle is the angle of the slope of the Mohr envelope (Figure 2.6). In sands, the primary factor governing shear strength is friction between the individual particles. Therefore, the friction angle (ϕ') is a key parameter used to describe the shear strength of sands. Sands are often referred so as cohesionless soils because their cohesion is usually null or negligible. The shear strength at failure is indicated as τ_f and is specified as the point of contact between the Mohr circle and the Mohr-Coulomb failure envelope, at a prescribed confining pressure. An elaboration of the triaxial test used to derive the failure envelope and shear strength parameters is given in the following section.

2.3. Triaxial compression test

In this research the triaxial compression test is used to derive the elastic and strength parameters of sand treated with Al-OM flocs. It gives information about the ability of the soil skeleton to support load, also called the shear strength. In this test a cylindrical specimen of soil is subjected to a constant confining pressure and to strain-controlled axial loading until failure in the soil sample occurs. The loading of the cylindrical soil specimen happens in the following stages:

1. First, an all-round cell pressure is applied (σ_3). This stress acts uniformly in all directions, causing both the axial stress and radial stresses to be equivalent to the minor principal stress σ_3. Consequently, no shear stress is generated within the specimen.
2. Then an axial load, F, is applied from outside the cell which is progressively increased. The F-induced additional stress is solely in the axial direction and thus equal to $\frac{F}{A}$.
3. The total axial stress equals the major principal stress (σ_1) and can be expressed as:

$$\sigma_1 = \sigma_3 + \frac{F}{A} \tag{2.12}$$

The difference between the major and minor principal stress ($\sigma_1 - \sigma_3$) is known as the deviator stress (q) and is the stress which is applied to the specimen by means of a force from outside the cell. During the shearing phase of the test the cell pressure (σ_3) is maintained constant, while the deviator stress is increased until failure. In Figure 2.7 an overview of the different stages involved in the triaxial test is shown.

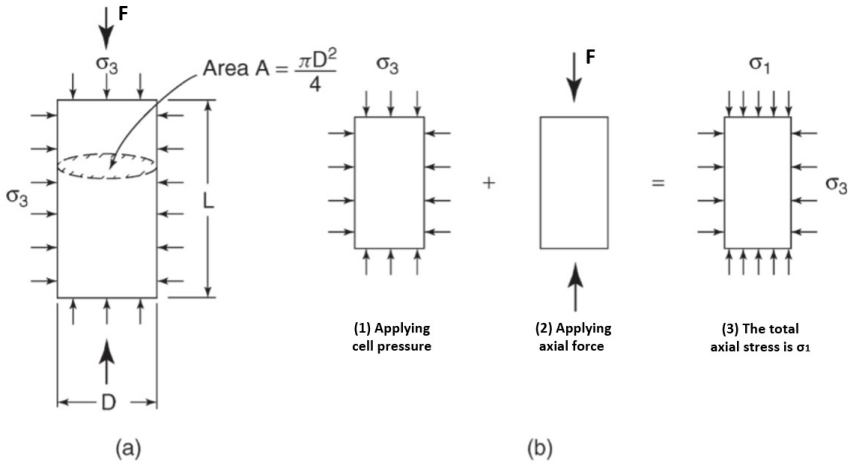

Figure 2.7: (a) Cylindrical specimen under triaxial compression; (b) loading stages of triaxial test.

Four sets of readings are observed while the triaxial test is executed: the cell pressure (σ_3); the axial load (deviator stress $\sigma_1 - \sigma_3$); the axial deformation or strain (ϵ); and the pore water pressure (u). With the above information the effective stresses can be calculated and elastic and strength parameters can be derived.

Triaxial compression tests are categorized in different groups. Both drained and undrained tests can be performed and a differentiation between unconsolidated and consolidated tests is made. Undrained means that there is no drainage permitted during the application of the deviatoric stress. This means that water cannot flow out of the pores. Because water has a very low compressibility, the specimen will not experience volumetric strain. This is because if the pores are completely filled with water (assuming a fully saturated specimen) that cannot escape from the pores, a change of pore volume cannot occur. In drained tests no excess pore pressure development takes place, as water can freely drain from the cell.

When a consolidated undrained triaxial test is performed, drainage is allowed to consolidate the specimen after applying the confining pressure. During the next stage (applying deviatoric stress) further drainage is prevented.

2.3.1. Derivation of elastic parameters

Elastic parameters describe the response of a soil to applied stress and strain. Specifically within the linear elastic range, which means that when you apply a load or stress to the soil, it deforms proportionally and elastically. When the load is removed, it returns to its original shape and size without any permanent deformation. The three primary elastic parameters are Young's Modulus (E), the shear Modulus (G) and Poisson's ratio (ν). These parameters are related to each other by the following equation:

$$E = 2G(1+\nu) \tag{2.13}$$

Since Young's Modulus, the shear Modulus and Poisson's ratio are related by the above equation, any two of these parameters are independent. They are obtained from the shearing phase of the triaxial test. Young's Modulus, or the modulus of elasticity, is a measure of the soil's resistance to deformation under a applied load. It quantifies the relationship between stress and strain in the linear elastic region of the stress-strain curve, which is given as the slope off the deviatoric stress (q) versus the axial strain (ϵ_a) (Latini and Zania, 2017):

$$E = \frac{\delta q}{\delta \epsilon_a} \tag{2.14}$$

The secant Young's Modulus (E_{50}) is derived from the slope at 50% of the maximum stress value:

$$E_{50} = \frac{\delta q_{max,50}}{\delta \epsilon_a} \tag{2.15}$$

The shear Modulus describes the shear stiffness, which represents the resistance to shear deformation. It is given as the slope of the deviatoric stress (q) versus the shear strain (ϵ_q) (Latini and Zania, 2017):

$$3G = \frac{\delta q}{\delta \epsilon_q} \tag{2.16}$$

Poisson's ratio characterizes the ratio of radial (transverse) strain to axial (longitudinal) strain. It quantifies how a material responds to deformation in terms of changes in shape (Latini and Zania, 2017):

$$\nu = -\frac{\delta \epsilon_r}{\delta \epsilon_a} \tag{2.17}$$

Poisson's ratio falls within a range of -1 to 0.5. A value of 0.5 corresponds to undrained test conditions, where there is no volume change in the sample. A Poisson's ratio higher than 0.5 is thermodynamically impossible as this would mean that when the material is stretched in axial direction it would expand to such an extend in the lateral direction that its volume and mass increases. Furthermore, Poisson's ratio cannot be derived from undrained triaxial tests, as no drainage is allowed and thus no volumetric strain occurs during the shearing phase of the test.

2.3.2. Derivation of strength parameters

Besides elastic parameters, also strength parameters can be obtained from triaxial tests. The experimental data extracted from the tests includes plots of deviatoric stress (q) as a function of mean effective stress (p'). These plots are also known as effective stress paths. A stress path is a way of representing the state of stress in a soil element. A familiar method of representing a soils stress state is the circle of Mohr, explained in Section 2.2. However, with this method, it is hard to represent changes of stress state. This is greatly clarified if circles are replaced by points, as is done with stress paths. In these plots, the mean effective stress (p') is equal to:

$$p' = \frac{\sigma'_1 + \sigma'_2 + \sigma'_3}{3} \tag{2.18}$$

Since two of the principal effective stresses are equal to the lateral effective stress in the triaxial test (axial symmetry), p' is equivalent to:

$$p' = \frac{1}{3}q + \sigma'_3 \tag{2.19}$$

The strength characteristics can be obtained by plotting the stress path in terms of p' and q and fitting the best failure line. The yield surface of Mohr-Coulomb criterion is presented with the following equation (Latini and Zania 2017, Chow et al. 2019):

$$q = M \cdot p' + d \tag{2.20}$$

in which M is the inclination of the failure envelope and d is the intercept of the failure line. The relation between M and the angle of shear resistance, ϕ', is given by the equation (Latini and Zania 2017):

$$M = \frac{6 \cdot \sin(\phi')}{3 - \sin(\phi')} \tag{2.21}$$

Details of the triaxial apparatus and its various features are described in Chapter 5.

3

Al-OM interaction

The proposed method for soil improvement is bio-inspired and relies on the interaction between aluminium (Al) and dissolved organic matter (DOM). This interaction results in the formation of flocs, which are subsequently mixed with sand, leading to modification of the mechanical properties. In this Chapter, Al-OM interaction will be evaluated to gain a deeper insight into the conditions conductive to floc formation and the potential variables influencing this process. The factors governing the formation of complexes are the type of metal used, pH levels, shear rate and the metal/carbon ratio (M/C ratio). In the following sections aluminium will be referred to as Al and organic matter as OM.

3.1. Coagulation and Flocculation of Al and OM

The interaction between organic compounds and aluminum, involving coagulation and flocculation, strongly depends on the chemical characteristics of both parties. Coagulation is a process in which colloids or particles in suspension are destabilized, which causes the formation of small aggregates of particles. In flocculation, these destabilized and aggregated particles further coalesce to form larger aggregates (Suopajärvi, 2015).

The solubility and ion-binding abilities of OM in water are highly dependent on the polarities of its functional groups (Zsolnay, 2003). Among these functional groups, the carboxylic and phenolic groups are commonly regarded as dominant binding sites, shown in Figure 4.2. These groups can protonate and deprotonate when interacting with other chemicals. Protonation and deprotonation reactions are fundamental chemical processes that involve the transfer of a proton (H^+) between chemical species. It is an important process which gives an indication of the reactivity of the carboxylic and phenolic groups.

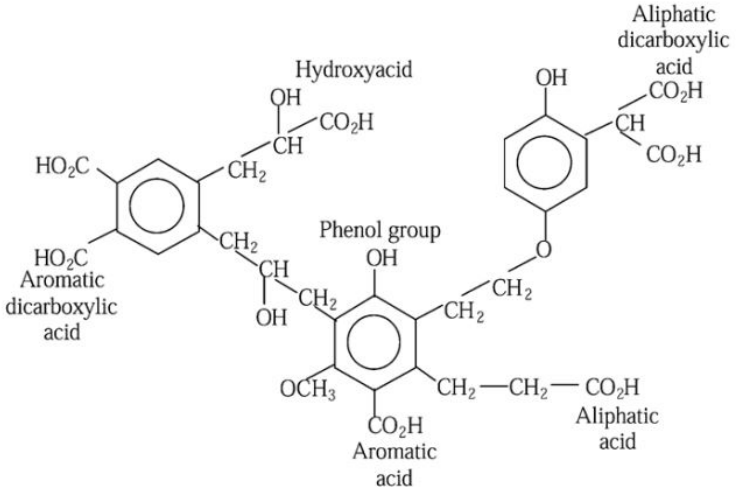

Figure 3.1: Hypothetical molecular structure of humic acid, showing the important functional groups (Duan and Gregory, 2003).

Equation 3.1 shows that deprotonation of the functional groups leads to a negative charge on the surface of OM molecules. Carboxylic groups are known to be a stronger acid than phenolic groups. Consequently, carboxylic groups tend to bind metals in a pH range from 3 to 5, while phenolic groups in a range of 7 to 9. This is because deprotonation of carboxylic groups takes place when the pH is higher than 4.4 while the phenolic group deprotonates at pH higher than 9.5 (Baalousha et al., 2006).

$$\begin{cases} \mathrm{RCOOH} \longleftrightarrow \mathrm{RCOO^- + H^+} & \text{Carboxylic} \\ \mathrm{ROH} \longleftrightarrow \mathrm{RO^- + H^+} & \text{Phenolic} \end{cases} \tag{3.1}$$

Al is known to create stable complexes with OM (Gone Droh et al., 2008). Due to their high valence they are able to bind multiple organic molecules simultaneously. When metals like Al are added to water, hydrolysis takes place, resulting in the formation of metal-hydroxide ions. The presence of Al dissolved in water is strongly connected to the pH level of the surroundings (Figure 3.2). Because the interaction of aluminium with organic matter to form complexes is influenced by its chemical state, it is thereby also influenced by pH levels. Under acidic conditions (low pH) Al^{3+} prevails and in more base conditions $Al(OH)_4^-$ predominates. Aluminium in the form of Al^{3+} has the highest positive charge and can therefore create the most binding sites with OM. On the other hand, the pH also influences the primary binding sites of the organic matter (OM). This implies that there is an optimum pH level for the formation of strong and stable Al-OM flocs.

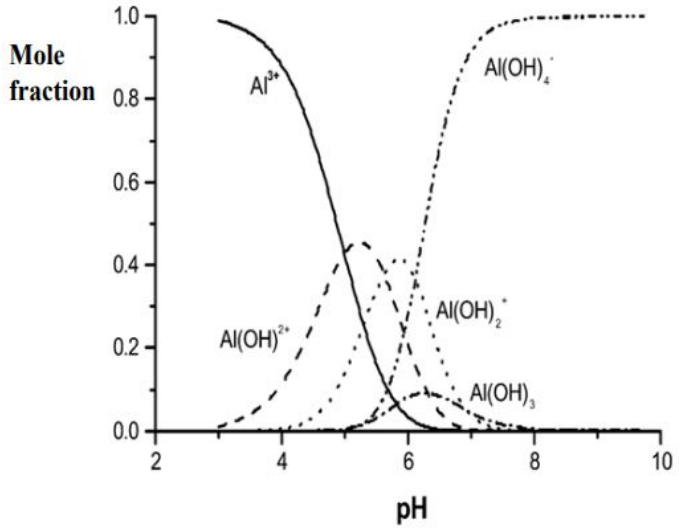

Figure 3.2: Mole fractions of aluminium dissolved hydrolysis products in equilibrium with amorphous hydroxides (Duan and Gregory, 2003).

3.1.1. Coagulation mechanisms

Flocs generated by coagulation mechanisms exhibit different sizes, strengths and structures (Li et al., 2006). Assuming that the particles are initially stable in the colloidal sense, then there are two steps in the flocculation process: (1) destabilization of particles and (2) collision of particles to form aggregates (Gregory, 2006). Hydrolysing coagulants, Al in this particular case, acts to destabilize and coagulate negatively charged colloids, OM. Firstly, OM is dissolved in water, leading to the presence of negatively charged colloidal particles, which exhibit repulsive forces between them. These charged colloids influence the distribution of the nearby ions in the water. Counter-ions present in the water accumulate on the colloids' surface, forming a dense layer known as the Stern layer (Suopajärvi, 2015). Beyond this layer, a more diffused layer of ions follows. The potential difference between the bound Stern layer and the diffused layer is referred to as the zeta potential (Figure 3.3). This zeta potential determines the electrical potential at the surface of the particle. A higher zeta potential indicates increased repulsion between colloids and, consequently, a more stable solution.

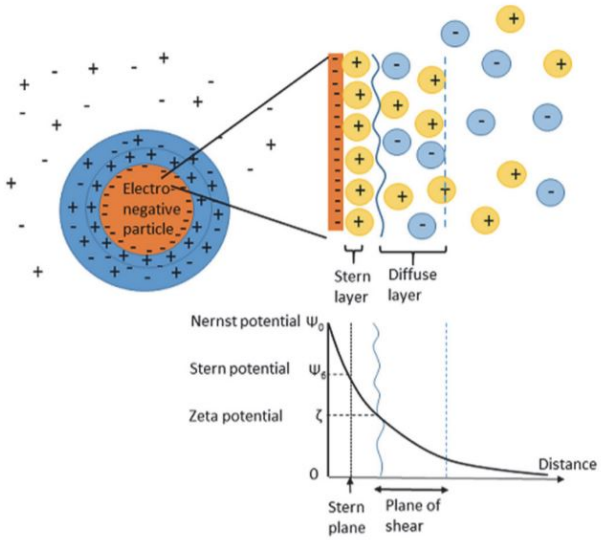

Figure 3.3: Conceptual representation of the electric double layer (Suopajärvi, 2015).

As stated above, the aggregation of the particles starts with the destabilization of the colloid particles with the use of a coagulant, followed by the aggregation of the destabilized particles. Essentially, there are three coagulation mechanisms which combine small particles into larger aggregates. The three coagulation mechanisms are (Figure 3.4):

- *Charge neutralization*: at low concentrations of coagulant (Al) and around a neutral pH, cationic hydrolysis products can absorb on the surfaces of negatively charged colloids (OM) and neutralize the particle charge.
- *Sweeping*: when higher doses of Al is added to the water, precipitation of metal hydroxide occurs, this is known as sweep flocculation. Colloidal particles can be tangled in these precipitates.
- *Bridging*: destabilization by bridging occurs when particles are linked together by segments of a polymer chain absorb on more than one particle (Li et al., 2006).

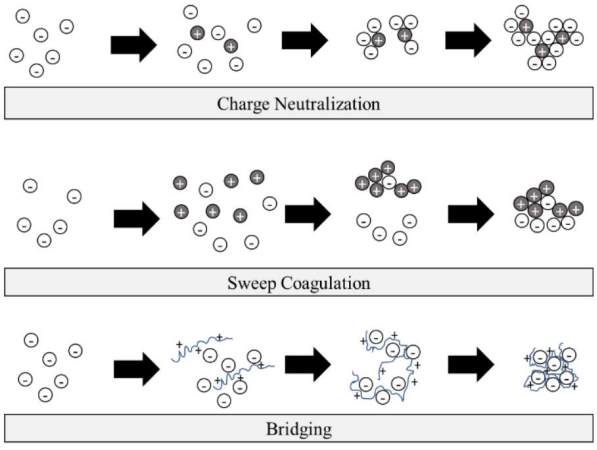

Figure 3.4: Conceptual representation of different flocculation mechanisms (Suopajärvi, 2015).

When the zeta potential value reaches the isoelectric point, e.g. a pH value at which the surface charge of the colloids is neutralized, the primary mechanism responsible for coagulation is charge neutralization (Wang et al., 2011). Sweep flocculation takes place when flocs exhibit a positive zeta potential, typically above 5 mV (Su et al., 2017). For the bridging mechanism, there should be a sufficient unoccupied surface on the particles for the attachment of segments of polymer chains already absorbed on other particles. When the pH is higher than the isoelectric point, colloids carry a negative net charge, and the polymer chain conformation becomes more extended, thereby promoting the bridging flocculation mechanism.

Sweep flocculation almost always leads to faster aggregation than charge neutralization and gives larger flocs. But bridging flocculation forms aggregates stronger than both sweep flocculation and charge neutralization, because polymer chains gives stronger bonds between particles than van der Waals forces (Gregory, 2006).

3.2. Regrowth potential

The usability of Al-OM flocs in sands is heavily dependent on the regrowth potential of the flocs after injection. This is because, from a practical point it is impossible to inject the floc solution in sand without subjecting it to shear forces. Shear rate is a parameter that strongly influences floc size. Literature indicates that shear forces reduce the size of metal-organic matter flocs and potentially hinder the regrowth potential of these flocs. Results of laboratory studies as part of the SoSEAL project demonstrate that Al-OM flocs exposed to an increased shear rate of 150, 300 to 400 rpm decreased the diameter from 750, 250 to 125 μm, respectively (Laumann et al., 2016). Since regrowth and floc size are shear dependent, Wiersma (2019) researched the effect of shear on regrowth potential of Al-OM flocs. He came up with a general growth curve of flocs subjected to shear rates as illustrated in Figure 3.5. After the coagulant is added to the DOM, floc development follows a certain pattern. Initially, a rapid growth phase can be seen, followed by the steady state and a breakage state. A steady state is reached again after the flocs are recovered. To what extend the flocs can grow back to their original state, depends on a couple of factors such as applied shear rate, dominant coagulation mechanism, breakage time, but also in what phase the flocs are broken. Yu et al. (2010b) found that broken flocs could completely regrow to their size before breakage when charge neutralization was the dominant coagulation mechanism. Flocs could even grow to sizes a little higher than that before breakage by adding a small dosage of aluminium to the suspension during the floc breakage period (Yu et al., 2010a). This is further elaborated in Section 3.2.2.

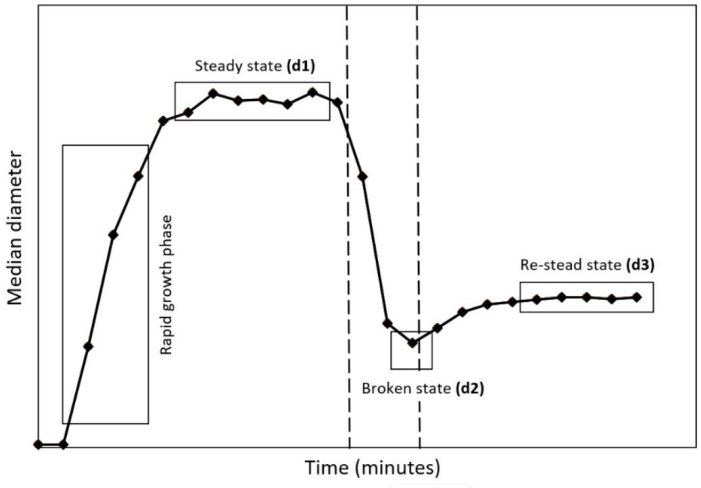

Figure 3.5: General pattern of the development of floc size (expressed as median diameter of volumetric particle size distribution) over time (Wiersma, 2019).

3.2.1. M/C ratio

The metal-carbon (M/C) ratio gives an inside to the amount of Al that needs to be added to the DOM in order to obtain flocculation. The Al predominantly used in SoSEAL experiments is in the form of aluminium chloride hexahydrate ($AlCl_3 * 6H_2O$) (Zhou, 2020 and Kaptein, 2021). When Al is added, the ions react with OM en form flocs that precipitate. After the binding sites of the OM molecules are saturated, any extra aluminium chloride hexahydrate will only result in more free ions. This increase in free ions results in a increase in electrostatic repulsion between the free ions and the residual positive charge left on the Al cations that are already bound to the OM. Which can lead to a decrease in particle size and precipitation observed. This rises the idea that there is an optimum value of the M/C ratio at which precipitation occurs and the size of the flocs is the highest (Gregory, 2006). From former laboratory experiments on SoSEAL it was found that an M/C ratio of 0.06 gives the largest flocs, the largest amount of precipitation and the strongest flocs (Zhou, 2020). Kaptein (2021) in her thesis researched the effect of the pH over an increasing M/C ratio for 5 grams of Al-OM (Figure 3.6). The resulting titration curve is used as a measure to monitor the flocculation process. The curve shows a decreasing pH over an increasing M/C ratio. A decrease in pH means an increase of the H^+ concentration. This is the result of the replacement of H^+ by Al^{3+} on OM. From the ionic charge it can be seen that for every mol Al^{3+} 3 mol of H^+ is released. According to the Figure, a critical M/C ratio was found between 0.025 - 0.031 and a pH of 4.5. At the

critical M/C ratio and pH, a sharp turning point is seen in the titration curve, which corresponds to the occurrence of flocculation. Although flocculation takes place starting from an M/C ratio of 0.025, in practice an M/C ratio of 0.06 is used to ensure the largest and strongest flocs.

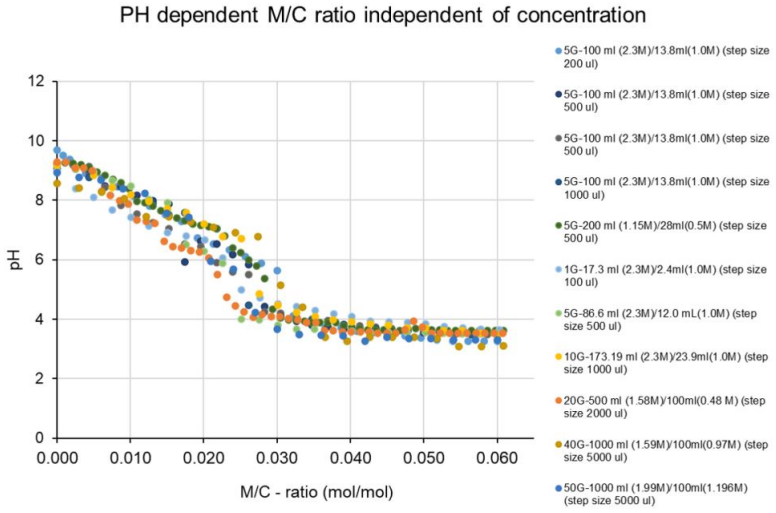

Figure 3.6: The relationship between an increasing M/C ratio and a dropping pH (Kaptein, 2021).

3.2.2. Second dosage of coagulant

The regrowth potential of flocs could be boosted by adding a second dosage of coagulant (Bo et al., 2011). Wiersma (2019) tested the effect of adding a second dosage of either Al or iron (Fe) shortly before breakage to the solution, in his study to the effect of shear stress on regrowth of Al-OM flocs. In an experiment with demi water a second dosage of Al did not increase the regrowth of flocs, as the strength and regrowth factors were very similar to those found for the standard dosage of 0.06 M/C ratio in this study. A comparable experiment was carried out with tap water. For both Al and Fe, the initial growth phase was larger with a higher M/C ratio. In Figure 3.7 the effect of an additional dosage of iron to both Al and Fe flocs can be seen. One can observe that adding Fe solution after breakage increases the size of the regrown flocs to values larger than the initial size. The limited regrowth with Al solution may be due to the low metal dosage, which is low compared to to other studies (Kim et al., 2013). A study by Su et al. (2017) looked at the regrowth ability of flocs when adding a second dosage of coagulant during the initial stage of flocculation instead of after flocs are already fully grown. It showed that an additional dosage of of coagulant could improve the flocs formation to larger sizes. This would suggest that the regrowth potential of Al-OM flocs could be increased when an extra dosage of Al is added under a lower M/C ratio than 0.06. As the flocs would not have reached a steady state yet.

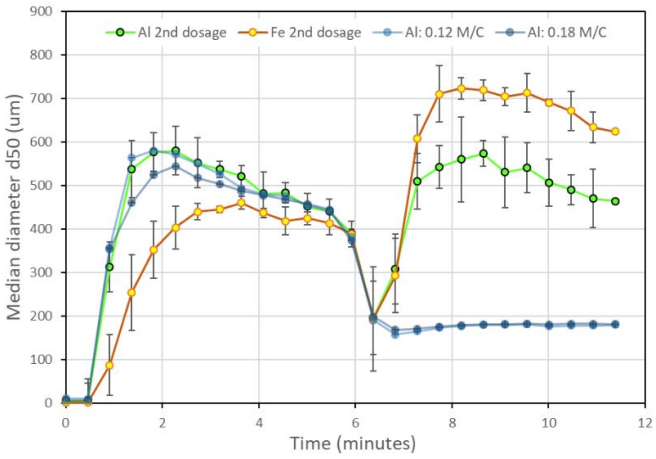

Figure 3.7: Development of average median diameter (μm) over time in tap water and with an additional 5 ml of iron solution shortly before the end of the breakage phase such that the M/C ratio increased from 0.12 to 0.18 Wiersma, 2019).

3.3. Colloid-porous medium interaction

Understanding the formation of flocs through coagulation and flocculation is crucial for comprehending the clogging potential of Al-OM flocs. As the formed flocs are mixed with sand, the interaction between the colloids and the porous medium is governed by various physical and physico-chemical processes. Physico-chemical interactions can be reversible and involve blocking and ripening. While mechanical filtration is typically an irreversible mechanism. Physical phenomena leading to deposition include both mechanical filtration and straining of individual particles as well ass aggregates. The later is also partly influenced by physico-chemical interactions as clarified below (Tosco et al., 2014):

- *Blocking*: this occurs particle-particle interactions are repulsive. Consequently, particles tend to interact with a clean porous medium initially, rejecting other particles. After the initial attachment of particles to the porous medium, further deposition is hindered.
- *Ripening*: this phenomenon arises when particle-particle interactions are attractive. Particles tend to interact with other particles within the porous medium, leading to an increase in attachment kinetics. This process continues until the porous medium is completely clogged.
- *Filtration*: this occurs when particles are larger than the size of the porous medium, impeding them from penetrating it.
- *Straining*: colloidal particles get trapped in down-gradient pore throats that are too small to allow particle passage. The irregularity of the porous medium's grain shape significantly influences this phenomenon.

All these phenomena, shown in Figure 3.8, involve the deposition of particles within the pore space. Clogging becomes particularly significant when examining processes like ripening, filtration and straining. In contrast, in the case of blocking, the decrease in porosity is typically minimal. The Al-OM colloids, used in this research, are particles that are bound by electrostatic attraction. The flocs are attracted to each other and consequently form bigger aggregates (Bonfiglio, 2017). It is thought that due to ground water flow these aggregates are transported towards the pore throats where they can clog and narrow the path for water flow, which leads to permeability reduction. This straining process is physical as well as a physico-chemical.

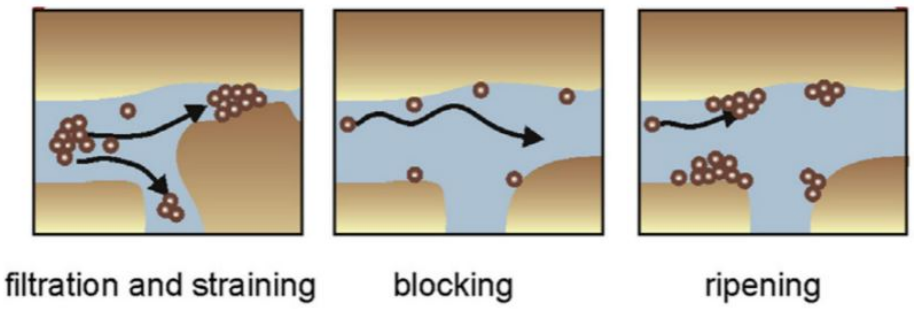

Figure 3.8: Conceptual representation of different colloid-porous medium interactions (Tosco et al., 2014).

4

Material properties and sample preparation

This chapter provides an overview of the materials used in the experiments, including aluminum (Al), organic matter (OM), and sand. First a description of the sand with its particle size distribution is given. Subsequently, the properties of the chemicals utilized in the experiments are presented. Lastly the sand/floc mixtures will be discussed.

4.1. Sand properties

For the experiments Baskarp (B15) sand is selected as the mixing material. The identical type of sand was used in the Sterkte Lekdijk project, in which the effectiveness of a SoSEAL barrier as a reliable solution to backward erosion piping was evaluated. Similar sand is also currently being used in a collaborative project at the TU Delft with TAUW and Heijmans. Here, the adhesion between the low permeability cohesive top layer and the SoSEAL barrier is tested on large scale. Therefore, it is chosen to use B15 sand in the experiments as in this way comparisons between different SoSEAL projects can be made more easily. The particle size distribution curve and characteristic grain sizes of B15 sand are shown in Figure 4.1 and Table 4.1. From the steep slope of the sieve curve it is evident that the B15 sand is very uniformly distributed. This is confirmed by the coefficient of curvature (C_c) which is ≈ 1.

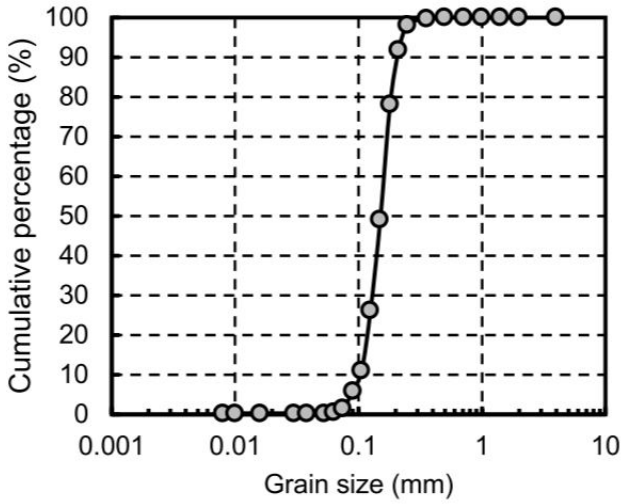

Figure 4.1: Sieve curve of B15 sand (Li et al., 2023a).

d_{10} (mm)	d_{15} (mm)	d_{50} (mm)	d_{60} (mm)	d_{60} / d_{10}	d_{90} / d_{10}	C_c
0.103	0.111	0.151	0.161	1.6	2.0	1.01

Table 4.1: Characteristic grain sizes of B15 sand (Li et al., 2023a).

4.2. Al-OM flocs

The organic matter (OM) used in the experiments is a humic acid called HUMIN-P 775, produced by Humitech Germany. HUMIN-P 775 is a selected leonardite material which has been carefully reacted with potassium compounds. In previous experiments within the SoSEAL research program, HUMIN-P 775 was chosen as the organic matter source due to its notable reactivity and solubility, making it as a suitable choice (e.g. Kaptein, 2021, Popma, 2017, Bonfiglio, 2017). The results of a CHNS analysis on the elemental composition of HUMIN-P 775 is shown in Table 4.2. Through this analysis, the quantity of organic carbon is assessed, impacting the M/C ratio. The molecular weight of the C compound in the OM is 28.87 g/mol (Kaptein, 2021).

Sample	N (%)	C (%)	H (%)	S (%)
$Humin_{01}$	1.05	41.81	3.12	0.83
$Humin_{02}$	1.00	42.54	3.83	0.88
Average	1.025	42.175	3.475	0.8545

Table 4.2: Composition of HUMIN-P 775 by CHNS analysis by the University of Amsterdam. Copied from Popma (2017).

The aluminium source used is aluminium chloride hexahydrate ($AlCL_3H_2O$), produced by Sigma Aldrich (CAS number 7784-13-6). The Al is produced in a solid crystal form and when dissolved it creates a colourless solution with a pH around 3.5. It has a molecular weight of 241.45 g/mol and it is a crystal powder.

4.3. Sand/flocs mixtures

The formation of Al-OM complexes is a key reaction for producing flocs used in the tests. Because of previous research in regard to the SoSEAL project, valuable information exists to optimize the formation of large and strong flocs. Therefore, in the experiments a M/C ratio of 0.06 is used, as this ratio results in the largest and strongest flocs (Zhou, 2020). The expected mass of dry flocs is 85% of the dry mass of OM (Popma, 2017). With this information Kaptein (2021) produced a table for the amounts in grams and mol of the materials per expected amount of dry flocs in grams in order to obtain a M/C ratio of 0.06, as shown in Table 4.3.

Flocculation	OM [g]	Al [g]	OM [mol]	Al [mol]
50	57.50	28.97	1.99	0.12
40	46.00	23.17	1.59	0.10
30	34.50	17.38	1.20	0.07
25	28.75	14.48	1.00	0.06
20	23.00	11.59	0.80	0.065
15	17.25	8.69	0.60	0.04
10	11.50	5.79	0.40	0.02
5	5.75	2.90	0.20	0.01
1	1.15	0.58	0.04	0.00

Table 4.3: The amount of chemicals for the expected flocculation. Copied from Kaptein (2021).

For the experiments a mix-and-place method is used, where the floc solution is made by adding the Al solution to the OM solution and set this to rest overnight. After 12 hours the floc solution is centrifuged at 2500 rpm for 25 minutes until the flocs are fully settled. The supernatant is decant from the solution, such that a high concentration of flocs solution is left over. Then the dry sand is mixed by hand with the concentrated floc solution until a homogeneous mixture has been formed.

4.3.1. Proctor's tests

Untreated as well as treated sand will be tested in triaxial test apparatus. Because sand is a non-cohesive media, samples cannot be tested without using a molt. Therefore, a certain the amount of compaction will be applied. To deduce the amount of compaction and moisture content of the samples to be tested, Proctor's test is used. The test is is utilized for the determination of optimum dry density and moisture content condition. When soil is compacted, the solid particles are packed more closely together by means of mechanical force, this in turn leads to an increase in dry density (Head, 1994). Compaction is achieved by the reduction of air voids in the soil, without reducing the water content. Under a given amount of compaction, there exist an optimum moisture content (OMC) at which the greatest value of dry density is reached. This works as follows; at a low moisture content the grains of soil are surrounded with a thin film of water.

This water tends to keep the grains apart even when compacted. When the moisture content increases the additional water enables the grains to be more easily compacted, because air is displaced. This increases the dry density. When the water content exceeds the maximum condition of dry density and moisture content, the additional water begins to push the particles apart, which in its turn reduces the dry density.

Table 4.4 lists the used proportions of sand and Al-OM flocs to get the concentrations 10, 5, 1 and 0 g/kg, respectively. These concentrations are chosen as higher concentrations of flocs are unlikely to occur in field conditions.

Floc concentration [g/kg]	**flocs [g]**	**sand [kg]**
10	100	10
5	50	10
1	10	10
0	0	10

Table 4.4: The proportions of flocs and sand used in the Proctor's tests.

The tests are performed according Eurocode 7 (EN 1997-2). Starting with an 8 % moisture content and building up with approximately 2-3 % per step a moisture content/dry density diagram can be made. For the test the cylindrical metal moult is used. The soil is placed in the mould in three layers, compacting each layer before placing a new layer, using 25 blows with a rammer. After this, the surface of the compacted soil is trimmed off. The mould with compacted soil is weighted. Then, the moisture content is determined by drying a sample of the compacted soil in the oven at 105 degrees for 24 hours.

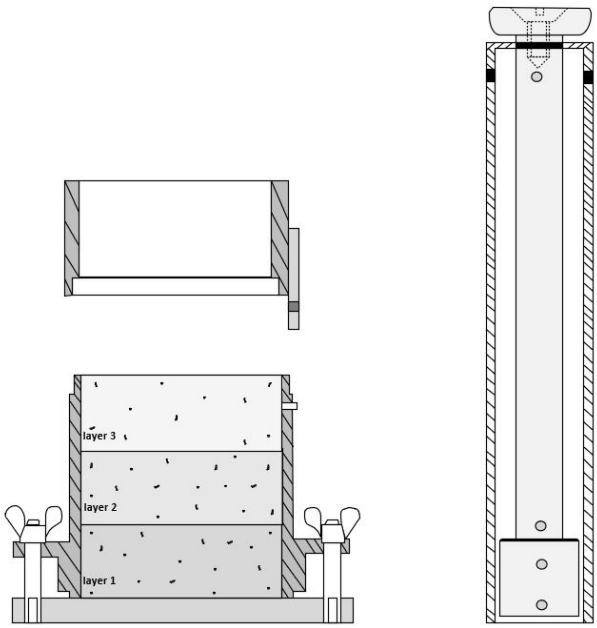

Figure 4.2: Equipment used for Proctor's test: (a) soil in mould after compaction, (b) hand rammer.

From the measured mass of pore water and mass of the soil solids with their corresponding densities, the porosity (n) and voids ratio (e) of each sample can be determined. The porosity is the ratio of the volume of voids (open spaces or pores) within a material to the total volume of the material. In which the total volume exists of the volume of the voids and the volume of the solid particles:

$$n = \frac{V_{voids}}{V_{total}} = \frac{V_{voids}}{V_{voids} + V_{solids}} \tag{4.1}$$

Since the volume of the voids is equal to the total volume minus the volume of the solids, this equation can be rewritten as:

$$n = \frac{V_{total} - V_{solids}}{V_{total}} \tag{4.2}$$

And the volume of the solids is equal to the mass of the solids divided by the specific gravity of solids ($G \approx 2.65 g/cm^3$), this gives the following:

$$n = 1 - \frac{m_{solids}}{G \cdot V_{total}} \tag{4.3}$$

With the porosity voids ratio (e) can be calculated. Voids ratio is a measure of volume of the void spaces (air and water) compared to the volume of the solid particles. It quantifies the amount of pore space existing in a soil sample:

$$e = \frac{n}{1 - n} \tag{4.4}$$

4.3.2. Test characteristics

The results of the Proctor's tests with different concentrations of Al-OM flocs are shown in Figure 4.3 and listed in Appendix A. With the tests the maximum dry densities with corresponding moisture contents are determined. The results are used for molding the samples for the triaxial tests.

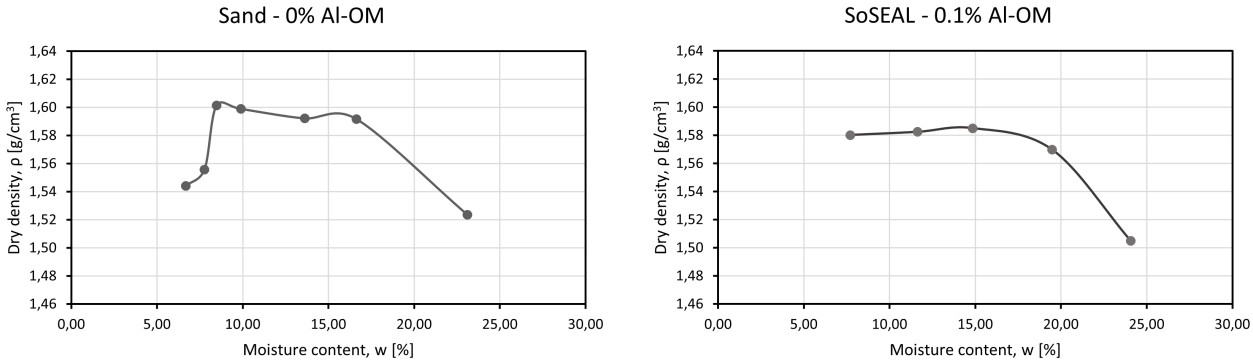

(a) Sand 0% Al-OM flocs.

(b) SoSEAL 0.1% Al-OM flocs.

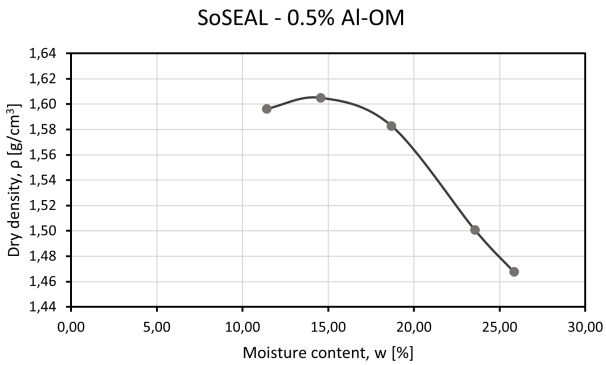

(c) SoSEAL 0.5% Al-OM flocs.

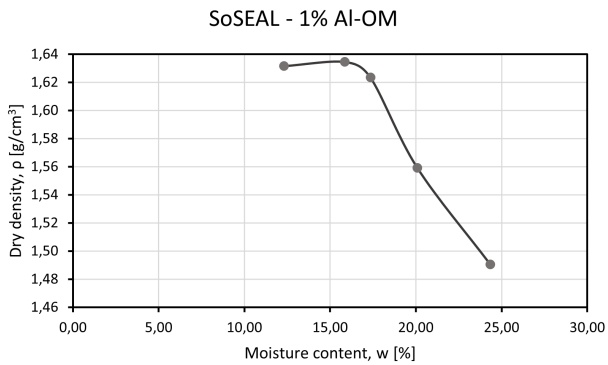

(d) SoSEAL 1% Al-OM flocs.

Figure 4.3: The measured dry density as function of moisture content obtained from the Proctor's tests for all samples.

A clear peak can be seen in the graphs from sand mixed with 1, 5, 10 g of Al-OM flocs. The untreated sand (Figure 4.3a) shows a much flatter compaction curve from which the optimum condition is less easy to define. This is often obtained from uniformly graded fine sands.

The peak provides the maximum dry density along with the corresponding moisture content, as listed in Table 4.5. For the triaxial tests 95% of the maximum dry density and optimal water content is taken as part of common Proctor's test procedure. Furthermore, with the measured moisture content, the mass of the soil solids and the specific gravity, the

porosity and the corresponding void ratio at 95% dry density are calculated. Here, it is assumed that the specific gravity is similar for all samples. A close alignment is seen in the porosity and voids ratio along the samples. This is in line with the similarities in moisture content and dry density. While a decrease in porosity would be expected with an increasing concentration of Al-OM flocs, given their role in clogging the pores between sand grains, the forces applied to compact the samples and release the air make the porosity and voids ratio less indicative of the presence of Al-OM flocs in this experimental setup.

Test No	ρ_d $[g/cm^3]$	$\rho_{d95\%}$ $[g/cm^3]$	w [%]	n [−]	e [−]
CU00	1.60	1.52	8.47	0.43	0.74
CU01	1.59	1.51	14.87	0.43	0.75
CU05	1.60	1.52	14.56	0.42	0.74
CU10	1.63	1.55	15.85	0.41	0.71

Table 4.5: The maximum dry density, 95% dry density and the corresponding moisture content derived from the Proctor's test results for different concentrations of Al-OM flocs in sand.

5

Experimental methods and protocols

The objective of this research is to assess the impact of Al-OM flocs on the mechanical characteristics of sand, employing the triaxial test apparatus. To establish the appropriate conditions for the triaxial test, preliminary experiments, outlined in Section 4.3, are conducted using Proctor's test. Subsequently, Section 5.1 details the triaxial test setup and explains the various stages involved. In Section 5.2 an exploration of Scanning Electron Microscopy (SEM), utilized for microscopic analysis of the soil samples, is given. The Chapter concludes with the testing program, providing an overview of the various tests, their characteristics, and labels (Section 5.3).

5.1. Triaxial test

For the purpose of testing the mechanical properties of the sand mixed with flocs, different proportions of Al-OM flocs are added. Table 5.4 lists the floc concentration and the confining pressure applied in the tests. All the specimens are tested under a confining pressure of 100 kPa as this gives an average value of overburden pressure applied on sands expected in dykes. The test series are duplicated to obtain a more reliable result. Besides this, the sand with 5 g/kg of Al-OM flocs is also tested under a confining pressure of 0.5 σ_v. With the results of the triaxial test under two different confining pressures, the Mohr-Coulomb failure envelope can be drawn, as explained in Section 2.2. From this the effective friction angle (ϕ') and cohesion coefficient (c') of the sand are derived. This gives inside in how the cohesion and friction angle are influenced by the addition of Al-OM flocs.

Floc concentration [g/kg]	**Confining pressure test No.1** σ_v **[kPa]**	**Confining pressure test No.2** σ_v **[kPa]**	**Confining pressure test No.3** $0.5\sigma_v$ **[kPa]**
10	100	100	–
5	100	100	50
1	100	100	–
0	100	100	–

Table 5.1: The triaxial test series with corresponding confining pressures and floc concentrations.

5.1.1. Test setup

This Section further explains the test-setup used during the experiments. For the experiments a triaxial test system of GDS Instruments is used. GDS instruments (a division of Global Digital Systems Ltd) designs, develops and manufactures material testing machines and software used for computer-controlled testing of soils and rocks (GDS, 2023). The system consists of a number of components listed in Table 5.2. The three main parts are the load frame, housing the triaxial cell, the pressure/volume chambers and the control acquisition software. The triaxial cell is placed in a velocity controlled load frame which is connected to a GDS control system and cell and back pressure/volume chambers (Figure 5.1). The data acquisition unit converts the analogue readings from the transducers to digital data which are then recorded by the acquisition software.

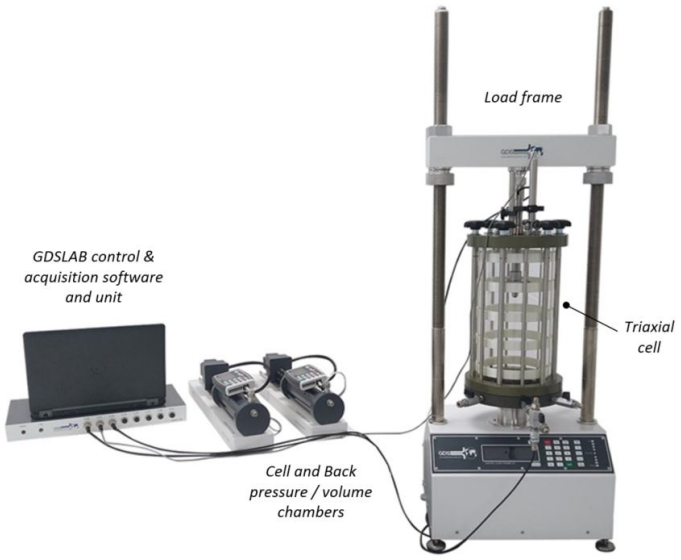

Figure 5.1: The triaxial test setup showing its major components: the triaxial cell, load frame, cell and back pressure/volume chambers and the control and aquisition software (GDS, 2023).

Component	**Main function**
Triaxial cell	House the specimen and cell fluid
Pedestal & top-cap	Provide specimen seating and drainage port
Rubber membrane, O-rings & porous discs	Seal the specimen from the cell fluid, allowing control over the effective stress and drainage
Cell pressure / volume controller	Apply confining stress to the specimen ($\sigma_c = \sigma_3$) by pressurising the cell fluid
Back pressure / volume controller	Apply back / pore pressure u to the specimen and measure the volume change ΔV
Velocity-controlled load frame	Shear the specimen through axial movement of a loading platen at a constant rate
Internal submersible load cell	Measure the change in axial load F applied to the specimen during shear
Pore water pressure (PWP) transducer	Measure the change in pore water pressure u within the specimen
Axial displacement transducer	Measure the change in height (and hence axial strain ϵ_a) of the specimen
Data acquisition unit	convert analogue readings from the load cell, PWP and axial displacement transducers to digital data
GDSLab control & acquisition software	Control test hardware and record digital readings taken from the data acquisition unit

Table 5.2: Primary components of a GDS triaxial automated system (GDS 2023).

Upon closer examination of the triaxial cell, the apparatus housing the soil samples, distinct components come into view. This cell consists of a cylindrical specimen chamber equipped with a piston assembly at the top and a base pedestal at the bottom, as illustrated in Figure 5.2.

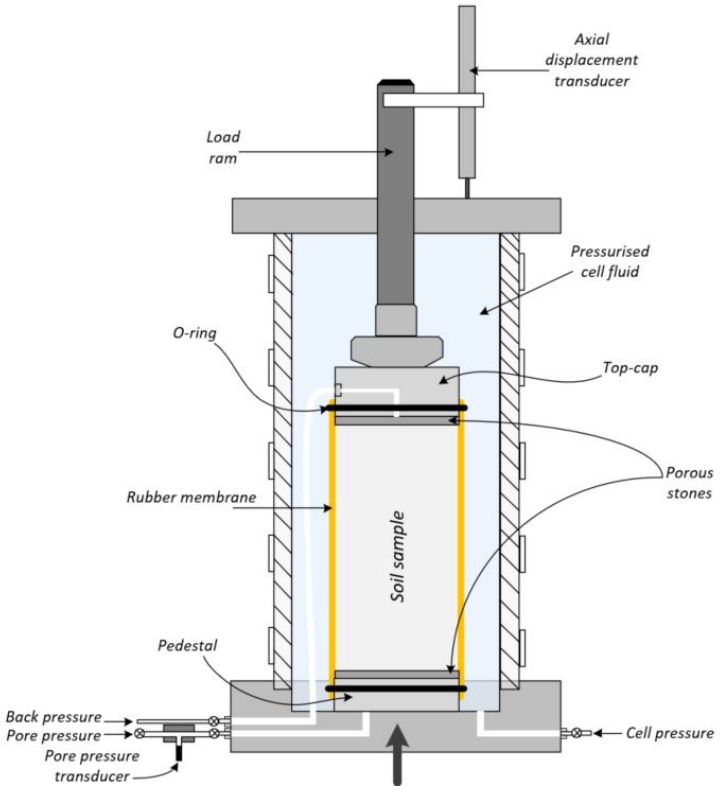

Figure 5.2: An overview of the triaxial cell with its various components.

Before starting the preparation of the apparatus, first all valves, connected to the cell and back pressure/volume chambers are de-aired. Then a small lens of water is formed on the base cap to prevent air bubbles. On top of the lens of water a saturated porous stone is placed covered by a filter paper cut in the same diameter. The soil sample is then carefully placed on the pedestal, while containing its shape. Subsequently a membrane suction stretcher is used to place a rubber membrane around the soil. On top of the sample another filter paper and porous stone are placed, followed by the top cap. The sample is sealed between the top cap and the pedestal by using O-rings. Once the sample is placed correctly, the triaxial cell is positioned around the sample and secured with 3 screws to the pedestal. Then the cell is filled with water, which can be pressurised with the cell pressure/volume controller, connected to the cell pressure valve. The back pressure controller is connected to the back pressure valve which is in turn connected to the top cap. The pore pressure valve and transducer is connected to the base of the specimen. With this, two separate systems can be distinguished; a confining pressure surrounding the soil sample driven by the cell pressure/volume system. And the pressure within the soil sample driven by the back pressure/volume system through the top-cap and the pore pressure system through the base. The systems are separated from each other by the rubber membrane.

Before starting the test, blocks are placed between the triaxial cell and the load ram to make sure the load cell does not apply any force to the soil sample yet. Once the triaxial cell is connected to the GDS control system, the software takes over this function.

5.1.2. Sample preparation

The soil sample needs to be prepared to fit on top of the pedestal within a rubber membrane. The samples are shaped in a cylindrical form with a height of 81.6 mm and a diameter of 38.6 mm by using a spilt-part mold (Figure 5.3b). First, the mold is coated with a lubricant in attempt to get the specimen out more easily. Then the (treated) sand is mixed with water to get to a dry density of 95% of the maximum dry density and water content (at maximum dry density), derived from Proctor's test results. The sand is divided in three equal parts and placed in the molt (Figure 5.3c). Every layer is compacted with a rammer. The top of each layer is notched in order to provide better adhesion between the layers (Figure 5.3d). Then the sample is carefully taken out of the mold by placing the mold on a pedestal and milling the sample out of the mold (Figure 5.3f). After this, the sample is placed on the pedestal on top of the cut filter paper in the triaxial cell.

(a) Materials for preparing the soil sample. (b) Spilt-part mold. (c) One layer of soil placed in the mold.

(d) Notched layer of soil. (e) Compacted soil in the mold. (f) Sample after milling it out of the mold.

Figure 5.3: Visualisation of the different steps of the sample preparation for the triaxial tests.

5.1.3. Test procedure

Once the setup is ready and the triaxial cell is connected to the software, the test can start. As explained in Section 2.3 the test consists of two stages. First an all-round pressure is applied (σ_3), after which an axial load is exerted from outside the cell. But before these stages can start, the soil sample should first be saturated. This is necessary to provide accurate measurements of pore water pressure. When dealing with partially saturated soils there is an added complication of pore air pressure which differs from the pore water pressure. Saturation is achieved by elevating the back and pore pressure to a sufficiently high level, allowing the air in the voids to be forced into solution. Synchronously, the cell pressure is increased to sustain a minimal positive effective stress within the specimen. Both pressures are raised simultaneously, maintaining a consistent difference between them. The back and pore pressure are intentionally kept slightly lower than the confining pressure to ensure that the effective stress remains positive ($\Delta\sigma = 10kPa$). Then the sample is set to rest for 48 hours, allowing the sample to saturate. After this the sample is flushed by creating a flow of water from bottom to top in the test specimen. Subsequently, the back pressure valve is closed and the back pressure controller is de-aired. Because the sand used in the tests is a very fine uniform graded sand, flushing was proved to be essential to get the samples sufficiently saturated ($B \geq 0.95$). Since a pressure difference is applied during flushing, this phase is used to do permeability measurements in test series 2. This is further explained in Section 5.1.4. The value of the pore pressure coefficient, B, can be calculated by rising the cell pressure by 50 kPa. The cell pressure increase causes an increase of pore pressure within the specimen, which should be observed until an equilibrium value is reached (Figure 5.4a). If the pore pressure coefficient has reached a value of ≥ 0.95 the sample is sufficiently saturated. The B-value can be calculated as follows:

$$B = \frac{\Delta u}{\Delta \sigma_3} = \frac{u_1 - u_0}{\Delta \sigma_3} \tag{5.1}$$

In which Δu is the measured difference in pore pressure before and after raising the cell pressure. When a B-value of ≥ 0.95 is reached, the effective stress in the sample must be brought to the value required for the test. This is achieved by adjusting the cell pressure and the back pressure so that their difference is equal to the desirable confining pressure (Table 5.4). And then allowing the resulting pore pressure in the soil sample to dissipate by the process of consolidation.

As the triaxial tests are Consolidated Undrained tests (CU), drainage is allowed during the consolidation phase. Drainage of water results in a decrease in volume and an increase in effective stress. Once the pore pressure is equal to the back pressure and has reached a steady-state, the sample is consolidated (Figure 5.4b) and ready for the shearing phase.

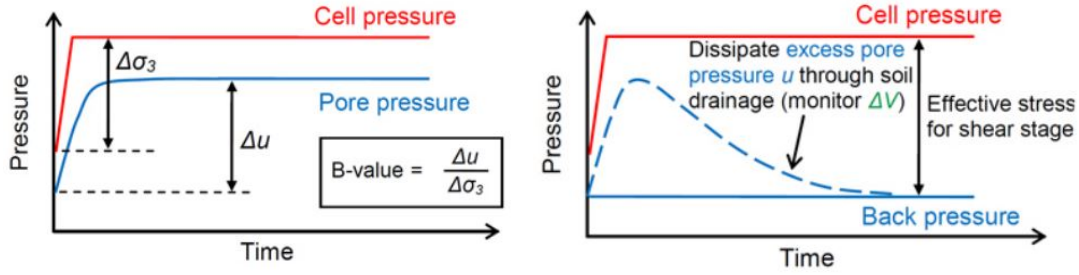

(a) B-check to confirm specimen saturation.

(b) Consolidation of the test specimen.

Figure 5.4: Graphs showing the different pressures in the soil sample during saturation and consolidation (GDS 2023).

Subsequently the sample is sheared to failure be gradually increasing the axial force while maintaining a constant cell pressure. A shearing rate target of 20% of the original height of 81.6 mm in 150 min is used. Which comes done to 0.16 mm/min. In Appendix B an overview of the specifications for each test can be found. It is notable that for test CU10-1 a higher back and cell pressure was needed to get to full saturation.

5.1.4. Permeability measurements

Besides the derivation of elastic and strength properties, the triaxial test can be used for permeability measurements. Permeability measurements are performed during the flushing of the sample and after consolidation in series 2 of the triaxial test series.

Permeability is a property that characterizes how easily water can flow through a medium, in this case (un)treated sand. The arrangement in the cell is similar to the one described in Section 5.1.1, except that a drainage connection to each end of the specimen is needed for these measurements. Which means an extra controller is connected to the bottom part of the soil sample; the base pressure/volume controller. With a drainage connection to the top of the sample (back pressure/volume controller) and the bottom of the sample (base pressure/volume controller) a flow of water through the soil sample under a known pressure difference is enabled from which the permeability (k_v) is derived (Figure 5.5).

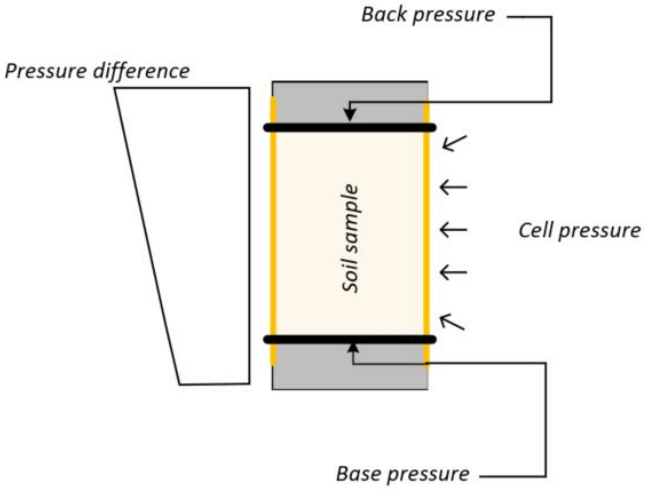

Figure 5.5: A conceptual figure of the sample setup for permeability measurements.

The test setup is similar to a constant head test in which the permeability of a soil can be determined by measuring the volume of water Q passing through the soil in a known time interval:

$$k_v = \frac{Q \cdot L}{t \cdot A \cdot \Delta h} \tag{5.2}$$

Here, the head difference (Δh) between the top and bottom of the sample is known and kept constant. Furthermore, the length (L) and cross sectional area (A) of the sample are known.

The same principle is used in the triaxial tests only that instead of a constant head difference, a constant pressure difference, is applied. A flow within the soil sample from top to bottom or vise versa is induced. For the flushing phase the direction of flow is chosen to be upwards to be able to de-air the back pressure/volume controller. For the permeability measurements after consolidation, a downwards flow is chosen, as this simulates a constant head test. The readings of the volume-change indicators from the back and base pressure controllers are taken at time intervals. From this the cumulative flow of water, Q (mm^3), from each volume-change indicator can be calculated. Then the the cumulative flow is plotted against the time. From the slope of this graph the rate of flow, q (mm^3/min), is deduced:

$$q = \frac{\delta Q}{\delta t} \tag{5.3}$$

If the effect of head losses in the pipelines and connections is neglected the pressure difference across the specimen is equal to the difference between the back pressure and the base pressure. The permeability k_v (m/s) in vertical direction is calculated as follows (Head 1994):

$$k_v = \frac{q}{60 \cdot A \cdot i} \tag{5.4}$$

In which A is the cross sectional area of the sample (mm^2), i is the mean hydraulic gradient across the sample and q is the rate of flow (mm^3/min). The mean hydraulic gradient is the difference in head per unit length. Since a pressure difference of 1 kPa is equivalent to a head of water 1/9.81 m, i can be calculated (Head 1994):

$$i = \frac{102}{L} \cdot \Delta p \tag{5.5}$$

Where L is the length of the sample, which is equal to 81.6 mm. During the flushing phase, a pressure difference of 7 kPa is applied and after consolidation, a pressure difference of 8 kPa is used. The second is based on hydraulic conductivity measurements of SoSEAL in previous research, where permeabilities in the range of 1E-6 to 1E-8 m/s were measured (Li et al., 2023b). Maximum hydraulic gradients recommended in ASTM D 5084 are as follows:

Soil permeability (m/s)	**Maximum hydraulic gradient**
10E-5 to 10E-6	2
10E-6 to 10E-7	5
10E-7 to 10E-8	10
10E-8 to 10E-8	20
Less than 10E-9	30

Table 5.3: Recommended maximum hydraulic gradient in ASTM D 5084 (Head, 1994).

An overview of the back an base pressure and direction of flow in both the flushing phase and after consolidation is shown in Figure 5.6.

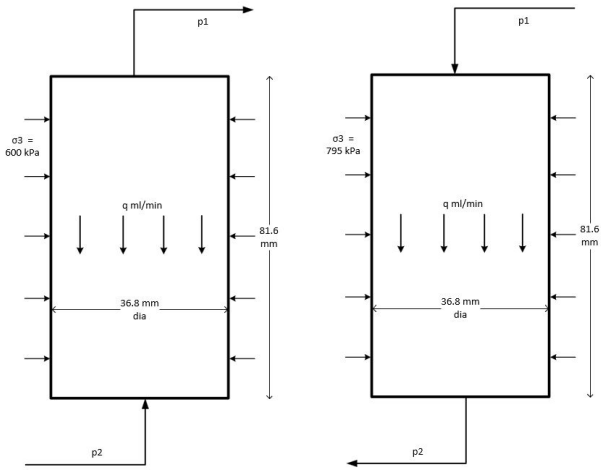

(a) Flushing phase. (b) Consolidation phase.

Figure 5.6: A conceptual figure of the pressures and dimensions used for the permeability measurements.

5.2. Scanning Electron Microscopy (SEM)

For the purpose of analysing the micro structural changes caused by Al-OM flocs added to sand, the Scanning Electron Microscope (SEM) is used. The SEM is an advanced instrument used to obtain highly detailed images of the surface of samples. It uses a beam of electrons rather than lights to illuminate the sample. Resulting in images with much higher magnifications and resolutions than optical microscopes, due to its smaller wavelength. This allows for extensive zooming in to the grains and examination the interaction with Al-OM flocs. Additionally, a component distribution diagram can be created. The SEM instrument is divided into three main components: the electron column, the specimen chamber and the computer/electronic controls (Figure 5.7). The uppermost part of the electron column consists of an electron gun responsible for generating an electron beam. Electromagnetic lenses within the column focus the beam into a small-diameter probe, typically a few nanometers wide. The scan coils in the column move the probe in a raster pattern across the sample surface situated in the chamber at the column's end. The gun, column, and specimen chamber are maintained under vacuum conditions. As the electron beam penetrates a few microns into the surface of a bulk sample, it interacts with the sample's atoms, generating various signals, including secondary and backscattered electrons, as well as characteristic x-rays. These signals are collected and processed to produce images and reveal the chemistry of the specimen surface. The ultimate lateral resolution of the SEM image corresponds to the diameter of the electron probe (Ul-Hamid, 2018).

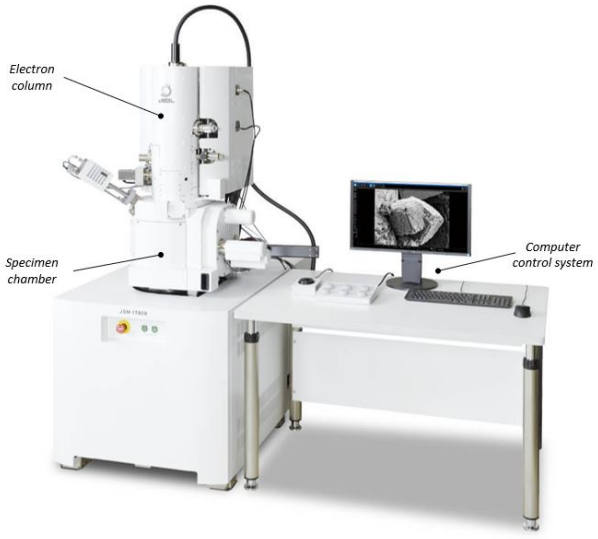

Figure 5.7: The SEM setup showing the three major sections of the SEM: the electron column, specimen chamber and computer control system (Jeol, 2023).

Sand samples with different concentrations of Al-OM flocs, corresponding with Table 5.4, are examined with the SEM. Samples are examined in both wet and vacuum conditions. The samples tested under vacuum conditions are provided with a carbon sticker. This carbon coating is helpful for the elemental analysis as it does not interfere with the detection of other elements (Ul-Hamid, 2018). The carbon sticker is placed on a metal cap. Subsequently, a very small amount of sample (approximately 5 mg) is applied onto the carbon sticker. The cap is then inserted into the chamber of the SEM and scanned. This process is repeated for all the samples. Interaction of the primary electron beam with the specimen material results in the generation of characteristic x-rays and white radiation. This collectively form an x-ray signal, which is collected with an x-ray detector. It measures its energy and intensity distribution and analyzes it in a manner that elements can be identified (Ul-Hamid, 2018). From this, component distribution diagrams are created. Following the analysis at vacuum conditions, sand with 0% Al-OM flocs as well as sand treated with 1% flocs are tested under wet conditions. This is done to understand the effect of creating a vacuum on the sand samples treated with Al-OM flocs. These samples are not applied on a carbon sticker. The operation of the SEM is handled by a technician at Delft University of Technology: Arjan Thijssen.

5.3. Testing program

The following table provides a summary of the various triaxial tests along with their corresponding test characteristics and labels. "CU" denotes a Consolidated Undrained test, and the subsequent numbers signify the floc content followed by the tests series. Test series 2 is a replication of test series 1, utilizing the same samples. Test series 3 is conducted under a reduced confining pressure to determine the Mohr-Coulomb failure envelope later on.

Test series	**Test No**	**Floc concentration** [%]	**Confining pressure** [**kPa**]	**Permeability measurements**
1				
	CU00-1	0	100	no
	CU01-1	0.1	100	no
	CU05-1	0.5	100	no
	CU10-1	1	100	no
2				
	CU00-2	0	100	yes
	CU01-2	0.1	100	yes
	CU05-2	0.5	100	yes
	CU10-2	1	100	yes
3				
	CU05-3	0.5	50	yes

Table 5.4: An overview of the triaxial test series.

In Table 5.5, the samples, along with their respective labels and floc concentrations, that were subjected to SEM are enumerated. Additionally, the table indicates whether the samples underwent testing under vacuum or wet conditions.

Test No	**Floc concentration** [%]	**Vacuum conditions**	**Wet conditions**
CU00	0	yes	yes
CU01	0.1	yes	no
CU05	0.5	yes	no
CU10	1	yes	yes

Table 5.5: An overview of the SEM analysis.

6

Experimental results and analysis

This Chapter delves into the experimental findings, starting with the presentation of the consolidation of the samples which is followed by the permeability measurements. In the second part of the Chapter the results of the shearing phase of the triaxial tests are displayed and analysed.

6.1. Sample consolidation

Once the test samples are placed in the triaxial cell and are sufficiently saturated, consolidation takes place. This is done by creating a difference of 100 kPa between the back pressure and the cell pressure. In test CU05-3 a pressure difference of 50 kPa is applied to establish the Mohr-Coulomb failure envelope for this test serie, requiring a minimum of two distinct confining pressures. When the resulting pore pressure in the soil sample is dissipated and is equal to the back pressure, the consolidation is done. In Figure 6.1 the cell, back and pore pressure against time are plotted for all tests. The graphs show that the pore pressure curves almost follow the back pressure curves immediately, indicating that the consolidation is done within a couple of minutes. From these graphs it appears that the consolidation phase does not provide information about the percentage of Al-OM flocs present in the sand.

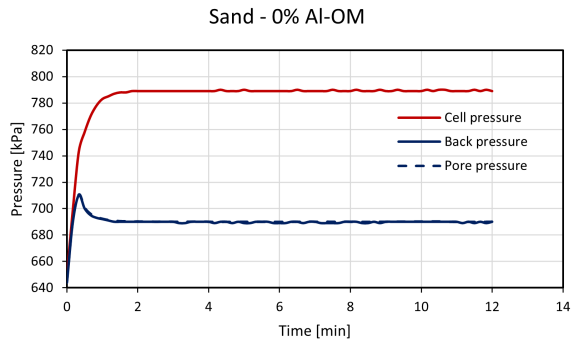

(a) Sand 0% Al-OM flocs series 1.

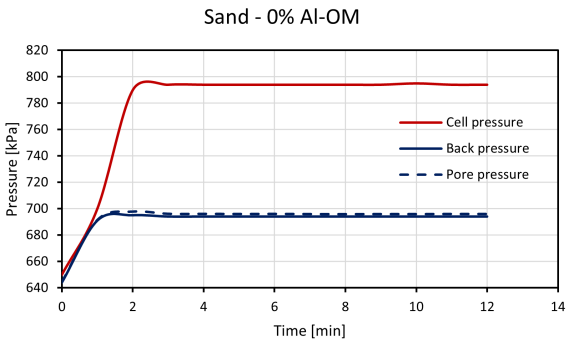

(b) Sand 0% Al-OM flocs series 2.

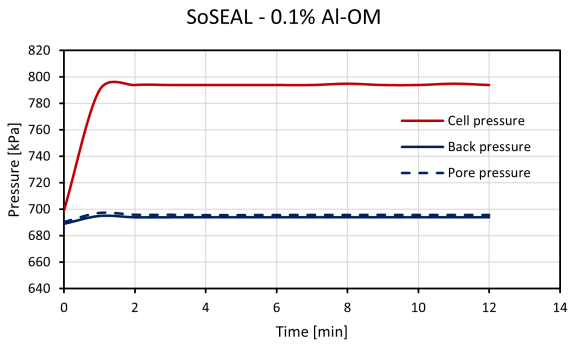

(c) SoSEAL 0.1% Al-OM flocs series 1.

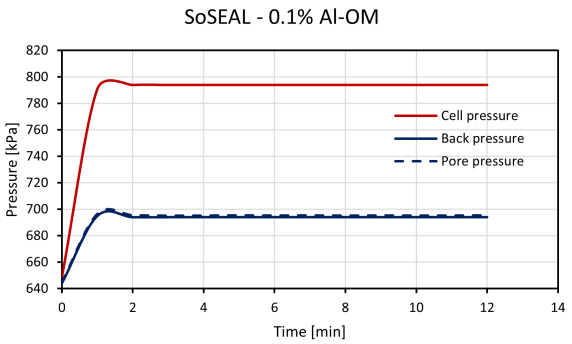

(d) SoSEAL 0.1% Al-OM flocs series 2.

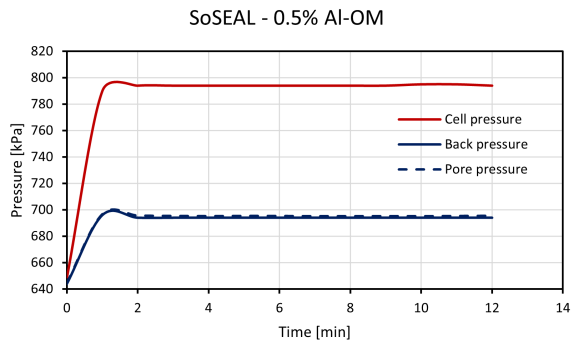

(e) SoSEAL 0.5% Al-OM flocs series 1.

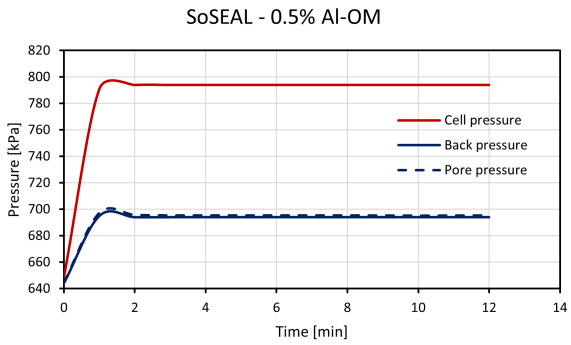

(f) SoSEAL 0.5% Al-OM flocs series 2.

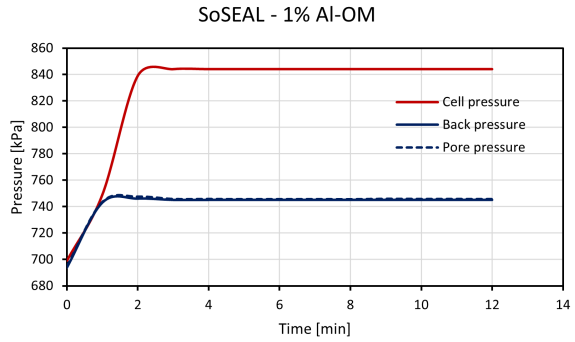

(g) SoSEAL 1% Al-OM flocs series 1.

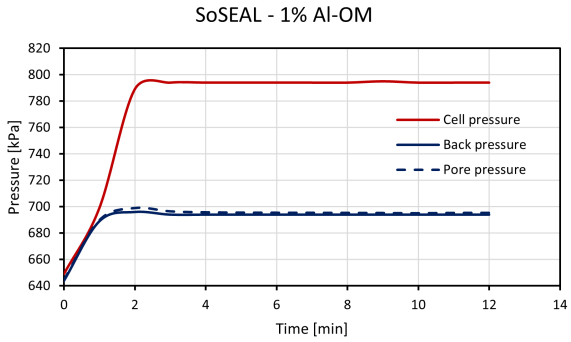

(h) SoSEAL 1% Al-OM flocs series 2.

Figure 6.1: The measured cell, back and pore pressure plotted against time for all samples during the consolidation phase of the triaxial test series.

6.2. Permeability measurements

Permeability measurements are incorporated in the test procedure to gather more information about the mechanical properties of the samples. Permeability measurements are performed during the flushing of the samples and after consolidation in series 2 of the triaxial tests. The mean hydraulic gradient, i, is calculated with the pressure difference between the top and the bottom of the soil sample. During the flushing phase, a pressure difference of 7 kPa is applied and after consolidation, a pressure difference of 8 kPa is used. Nevertheless, the pressure controllers for both back and base pressures strive to maintain the specified pressure differences (7 and 8 kPa, respectively). In practice, the actual pressure differences tend to be slightly lower due to the controllers' efforts to regulate the pressures. The mean hydraulic gradient (i) is calculated by averaging the real-time back and base pressures. Appendix C provides an overview of the average real-time pressures and the calculated mean hydraulic gradient. Notably, the controllers were having a harder time controlling a pressure difference after consolidation than during the flushing phase. Additionally, the height of each sample is adjusted based on the axial displacement measured at the beginning of each permeability test.

The rate of flow (q) can be derived from taking the slope of the graph of the volume (mm^3) plotted against the time (min) (Figure 6.2 and 6.3). In the graphs the grey line represents the base volume and the blue line represents the back volume. It can be seen that the back and base volume switched direction from the flushing phase and the consolidation phase. This is consistent with the direction of flow chosen for both situations.

When looking at the results from the flushing phase it is notable that the time to flush the sample, e.g. to get to a volume change of 9000 mm^3, increases with an increasing concentration of Al-OM flocs. This can be explained as an increasing amount of flocs is clogging the pore space in between the sand grains, making it more difficult for the water to pass. However, when looking at the highest concentration of flocs (1%) the time to reach this volume change is actually similar to the untreated sand. Which is confirmed when the permeability coefficients are compared. With the mean hydraulic gradient (i), the area (A) of 1170.21 mm^2 and the rate of flow (q), the permeability (k_v) in vertical direction is calculated in both m/s and m/d. The results are summarized in Table 6.1. Up to 0.5% flocs, the permeability is reduced compared to the untreated sand in the flushing phase. Additionally, it can be seen that the volume change in test CU05-3 is not linear (Figure 6.2c). With an increasing time, the slope is increasing simultaneously. It is plausible that this is caused by

an increasing degree of saturation over time. However, this phenomenon is not seen at the other samples.

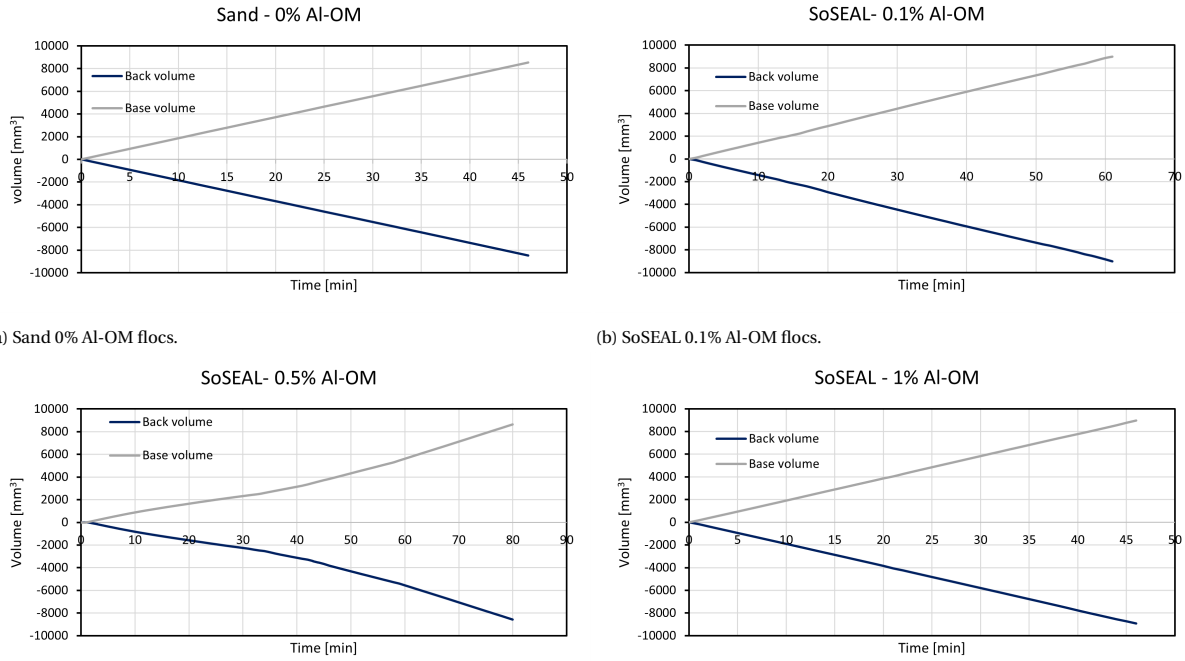

(a) Sand 0% Al-OM flocs.

(b) SoSEAL 0.1% Al-OM flocs.

(c) SoSEAL 0.5% Al-OM flocs.

(d) SoSEAL 1% Al-OM flocs.

Figure 6.2: The measured back and base volume plotted against time during the flushing phase for all samples of series 2 of the triaxial tests.

Test No	k_v $[m/s]$	k_v $[m/d]$
CU00-2	7.40E-7	6.39E-2
CU01-2	4.95E-7	4.27E-2
CU05-2	1.79E-7 - 4.69E-7	1.55E-2 - 4.06E-2
CU10-2	7.75E-7	6.70E-2

Table 6.1: Derived hydraulic conductivity, k_v, from the flushing phase for all samples of series 2 of the triaxial tests.

The volume changes in the back and base controllers from the permeability tests after the consolidation phase are shown in Figure 6.3. When comparing the permeability coefficient results from this phase (Table 6.2), to the results from the flushing phase (Table 6.1), it can be seen that the coefficient is higher in all cases. After consolidation the sample is fully saturated, whereas in the flushing phase the goal is to get the sample fully saturated. Hence complete saturation is not yet reached. As the saturation increases, the hydraulic conductivity generally increases, since the water does not have to find a path around air-bubbles. Additionally, the hydraulic conductivity is lower in all the samples treated with Al-OM flocs in comparison to the untreated sand (Figure 6.4b). However, from these results no correlation can be drawn between an increasing concentration of Al-OM flocs and a reduction in permeability as all the measured hydraulic conductivities are in the same range as the untreated sand (CU00-2). This might be due to the similarity in porosity's measured along all samples. Here two mechanisms are counteracting each other; on one hand the porosity should be reduced by an increasing percentage of Al-OM flocs, but on the other hand the higher the percentage of Al-OM flocs, the harder it is to compact the sand. Another contributing factor could be that the tests are performed under a stress state of 100 kPa; applied by the pressurized water surrounding the test samples. Permeability measurements on SoSEAL under a specifically prescribed load have not been executed before.

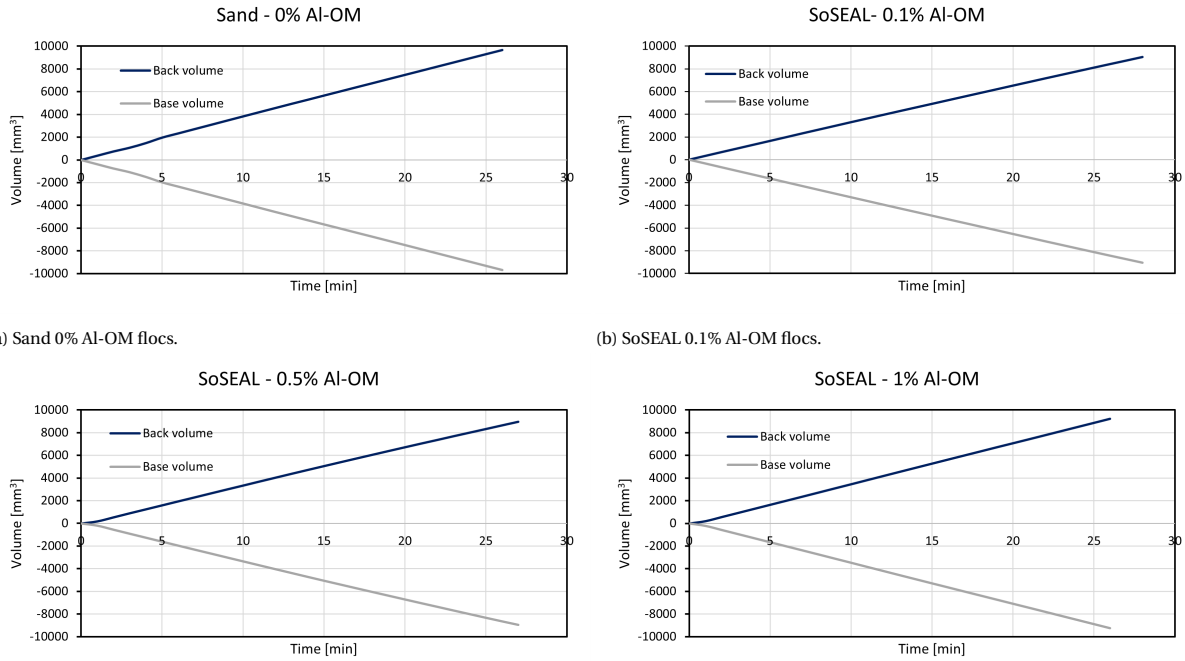

(a) Sand 0% Al-OM flocs.

(b) SoSEAL 0.1% Al-OM flocs.

(c) SoSEAL 0.5% Al-OM flocs.

(d) SoSEAL 1% Al-OM flocs.

Figure 6.3: The measured back and base volume plotted against time after consolidation for all samples of series 2 of the triaxial tests.

Test No	k_v $[m/s]$	k_v $[m/d]$
CU00-2	4.11E-6	3.55E-1
CU01-2	3.71E-6	3.21E-1
CU05-2	3.05E-6	2.63E-1
CU10-2	3.77E-6	3.26E-1

Table 6.2: Derived hydraulic conductivity, k_v, from after consolidation for all samples of series 2 of the triaxial tests.

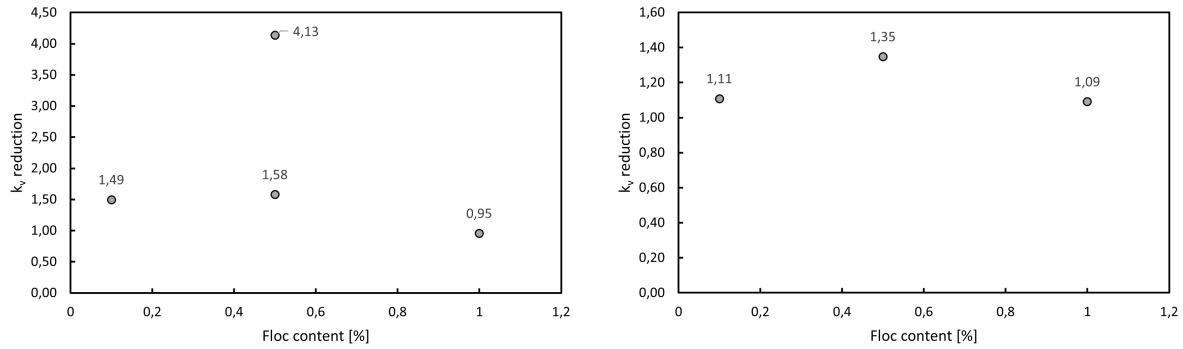

(a) Decrease in hydraulic conductivity, k_v, during the flushing phase.

(b) Decrease in hydraulic conductivity, k_v, after consolidation.

Figure 6.4: The hydraulic conductivity reduction over an increasing concentration of Al-OM flocs to sand. Derived from changes in back and base volumes during the flushing phase and post-consolidation of series 2 of the triaxial tests, in which the hydraulic conductivity values are normalized over the hydraulic conductivity of the sand with 0% Al-OM flocs.

6.3. Shearing

When the consolidation is complete and permeability measurements are performed the samples are ready to be sheared to failure. This is done by gradually increasing the axial force on the specimen. In most samples a very clear shear band from top to bottom can be seen (Figure 6.5). The shear band is marked yellow in Figure 6.5b. Furthermore, it stood out that the samples with a higher concentration of Al-OM flocs (e.g. ≥ 0.5%) contained their shape after the water was

removed from the cell. While the samples with no or a low percentage of Al-OM flocs clearly did not contain their shape (Figure 6.6). Additionally, in test CU01-1, CU10-1, CU01-2 and CU05-2 the set maximum load value of 1.8 kN of the triaxial test was reached. The boundary of this load value has been stretched to 2 kN for these tests. Even with a load value of 2 kN, sample CU05-2 could not reach failure.

After shearing the samples are dried in the oven for 24 hours to determine their moisture content, displayed in Appendix B. The moisture contents of all samples are in the range of 24-26 %. It was visible that the samples with a higher concentration of Al-OM flocs (e.g. $\geq 0.5\%$) kept their shape even after being dried in the oven (Figure 6.7). Test sample CU10-2 showed a clear crack at 1/3 of its height. This suggests that the sample failed on a connection line between two layers of compacted soil.

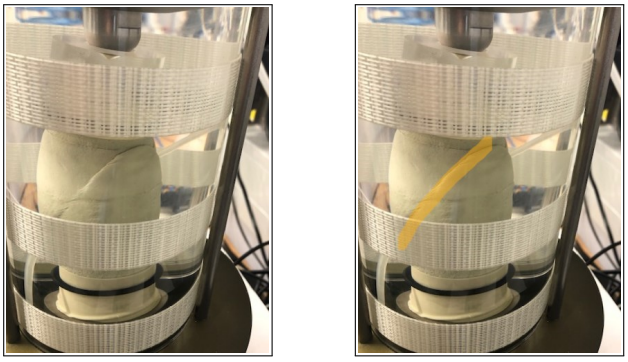

(a) A clear shearband is formed. (b) The shearband marked.

Figure 6.5: Test sample CU01-1 after shearing.

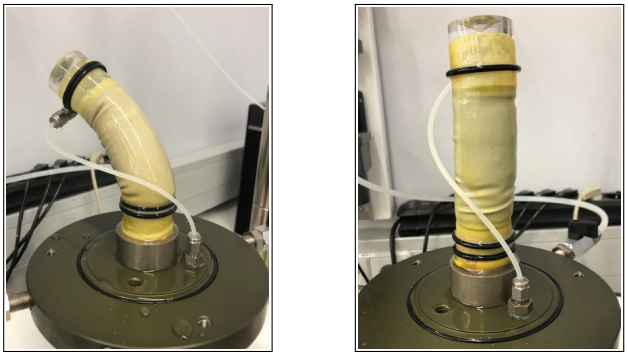

(a) Sample CU00-1. (b) Sample CU10-1.

Figure 6.6: Test samples CU00-1 and CU10-1 after water has been removed from the triaxial cell.

(a) Sample CU01-2. (b) Sample CU05-2.

Figure 6.7: Test samples CU01-2 and CU05-2 after drying in the oven for 24 hours.

The experimental data, derived from the shearing phase, includes plots of deviatoric stress and pore pressure versus axial strain shown in Figure 6.8 and 6.9. A trend of an increase in deviator stress is seen with a rising percentage of Al-OM flocs in both round 1 and round 2. The results from round 1 are similar to those of round 2. However, the maximum deviatoric stress from CU05-1 is lower than CU01-1. Where in round 2 these results lay very close together. It could due to a flaw in the setup in the first test serie, like an offset between the top cap and the load ram. A similar situation is seen when test CU10-1 and CU10-2 are compared. Here, the difference can be attributed to the local failure occurred in sample CU10-2.

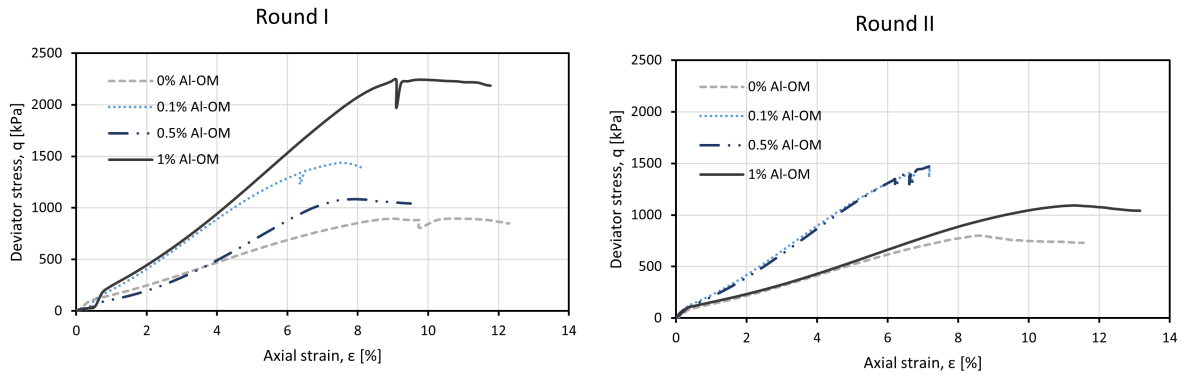

(a) Test series 1.

(b) Test series 2.

Figure 6.8: The measured deviatoric stress as a function of axial strain during the shearing phase of the triaxial test series for different concentrations of Al-OM flocs in sand.

When the pore pressure versus the axial strain is plotted, a phase transformation from contraction (increase in pore pressure) to dilation (decrease in pore pressure) at about 1-3 % axial strain is seen. It is apparent that the dilation is larger for the treated sands compared to the untreated sands (Figure 6.9).

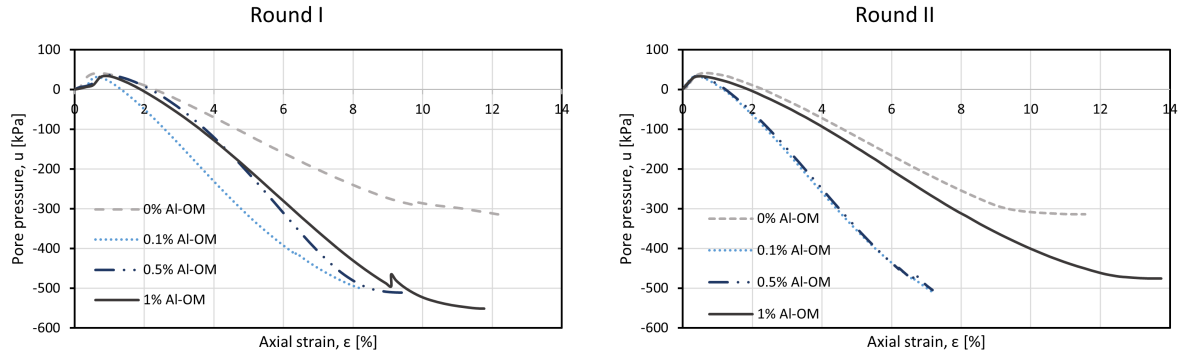

(a) Test series 1.

(b) Test series 2.

Figure 6.9: The measured pore pressure as a function of axial strain during the shearing phase of the triaxial test series for different concentrations of Al-OM flocs in sand.

Furthermore, different shearing properties are derived from this phase of the triaxial test. In the following subsections an overview of the elastic and strength parameters corresponding to different concentrations of flocs is given. Additionally, the derivation of the Mohr-Coulomb failure envelope for both test CU00-1 and CU05-1 is presented, enabling a comparative analysis of cohesion and friction angle based on these envelopes.

6.3.1. Estimation of elastic parameters

The elastic parameters of the soil samples are obtained from the shearing phase of the test. Depending on the plot the gradient in this phase will give the Young's Modulus (E) the secant Young's Modulus (E_{50}) or the shear Modulus (G).

The plots for the derivation of these elastic parameters can be found in Appendix D. The results are listed in Table 6.3. Poisson's ratio (ν) cannot be derived from these tests as the shearing phase is performed under undrained conditions.

Test No	E $[MPa]$	E_{50} $[MPa]$	G $[MPa]$
CU00-1	10.133	11.717	11.129
CU00-2	9.440	10.342	11.366
CU01-1	21.088	21.862	24.036
CU01-2	20.640	22.017	24.027
CU05-1	15.390	12.794	17.558
CU05-2	21.132	–	24.538
CU10-1	25.681	24.363	23.499
CU10-2	10.763	10.831	12.311

Table 6.3: The derived elastic parameters from the shearing phase of the triaxial test series for different concentrations of Al-OM flocs in sand.

The results show an increase of the elastic parameters with an increasing percentage of Al-OM flocs in the sand. Young's Modulus (E) and shear Modulus (G) are generally higher for higher percentages of flocs (Figure 6.10) . The exception is test CU10-2. Although the value for E and G are higher than for the untreated sand it is lower than CU01 and CU05. This is not in line with the results from the first round of tests and can be explained by the local failure which occurred in the attachment between two layers. In addition, it is noticed that the secant Young's Modulus E_{50} is very similar to Young's Modulus, E. The secant Young's Modulus of CU05-2 could not be derived, since the maximum load value of the triaxial cell had been reached before failure occurred.

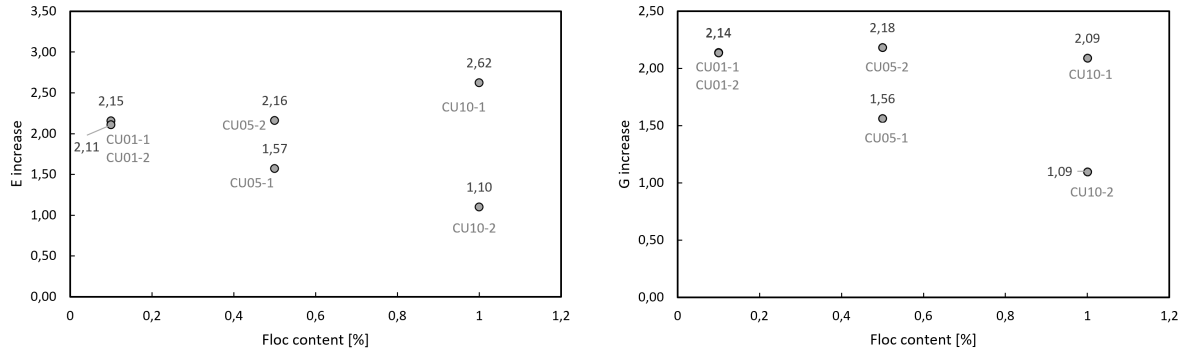

(a) Increase in Young's Modulus, E, compared to untreated sand.

(b) Increase in shear Modulus, G, compared to untreated sand.

Figure 6.10: The increase in elastic parameters E and G over an increasing concentration of Al-OM flocs to sand. Derived from the shearing phase of the triaxial test series, in which the values are normalized over the derived elastic parameters of the sand with 0% Al-OM flocs.

6.3.2. Estimation of strength parameters

In Figure 6.11 the deviatoric stress (q) is illustrated with respect to the mean effective stress (p') for test series 1 and 2. Since the tests are performed under undrained conditions, the samples are kept at a constant volume during the shearing phase. It is seen that the stress path in $p'-q$ space very quickly deflects to the critical state line and follows this line until failure occurs. The critical state of a soil describes a specific condition, where the soil has reached a state of constant volume and maximum shear strength under a range of applied stresses. Therefore, the slope of the failure line (M) and the corresponding derived friction angle (ϕ') are referred to as Critical State Parameters and listed in Table 6.4. The derivation of these parameters can be found in Appendix E. Furthermore, it can be seen that the stress paths of all the samples start at mean effective stress level of 100 kPa , as this is the confining pressure applied in the tests.

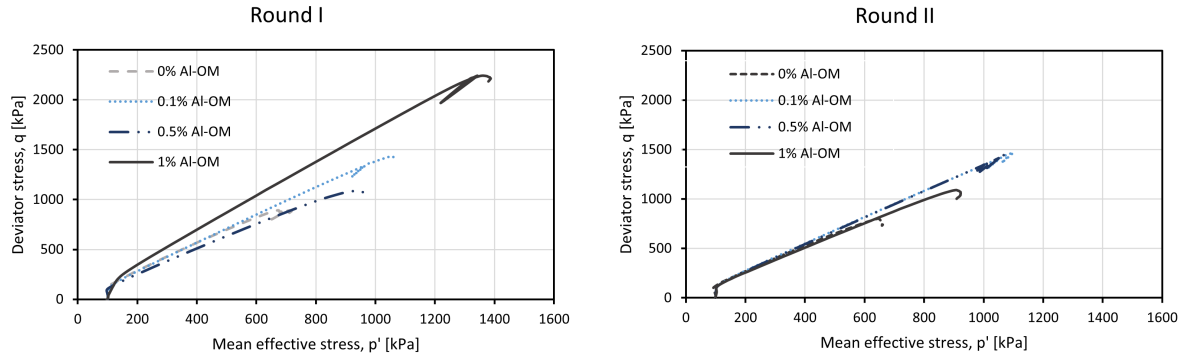

(a) Test series 1.

(b) Test series 2.

Figure 6.11: The measured deviatoric stress as function of mean effective stress during the shearing phase of the triaxial test series for different concentrations of Al-OM flocs in sand.

Test No	M_{cs} [−]	ϕ'_{cs} [°]
CU00-1	1.35	33.44
CU00-2	1.26	31.38
CU01-1	1.40	34.58
CU01-2	1.35	33.44
CU05-1	1.24	30.92
CU05-2	1.37	33.89
CU10-1	1.66	40.55
CU10-2	1.24	30.92

Table 6.4: The derived Critical State Parameters from the shearing phase of the triaxial test series for different concentrations of Al-OM flocs in sand.

The failure states in terms of p and q are used to determine the strength of the soil. The deviatoric and mean effective stress (q_p, p'_p) at failure are listed in Table 6.5. These results show that the deviatoric stress at failure increases with an increasing percentage of Al-OM flocs, with exception for test CU05-1 and CU10-2 (Figure 6.12). The peak stresses for test CU05-2 could not be determined, since the maximum load value of the test was exceeded before failure occurred.

Test No	σ'_{3p} $[kPa]$	σ'_{1p} $[kPa]$	p'_p $[kPa]$	q_p $[kPa]$
CU00-1	374.30	1267.79	672.10	893.49
CU00-2	376.40	1176.85	643.22	800.45
CU01-1	573.82	2008.83	1052.20	1435.01
CU01-2	609.52	2077.89	1098.98	1468.37
CU05-1	578.45	1664.41	940.44	1085.96
CU05-2	(−)	(−)	(−)	(−)
CU10-1	615.98	2857.80	1363.25	2241.81
CU10-2	545.54	1635.66	908.91	1090.12

Table 6.5: The measured failure line parameters from the shearing phase of the triaxial test series for different concentrations of Al-OM flocs in sand.

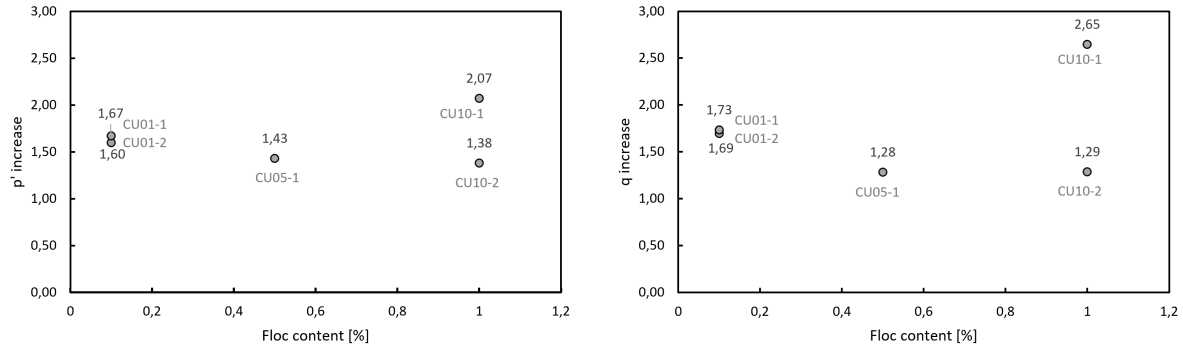

(a) Increase in mean effective stress, p', compared to untreated sand.

(b) Increase in deviatoric stress, q, compared to untreated sand.

Figure 6.12: The increase in strength parameters p' and q over over an increasing concentration of Al-OM flocs to sand. Derived from the shearing phase of the triaxial test series, in which the values are normalized over the derived strength parameters of the sand with 0% Al-OM flocs.

6.3.3. Derivation of the Mohr-Coulomb failure envelope

When a series of compression tests at different confining pressures is carried out on an identical soil sample, the Mohr-Coulomb failure envelope can be drawn. This is a tangential line to the Mohr circles at different confining pressures representing failure. The envelope is used to derive the effective shear strength parameters cohesion, c', and friction angle, ϕ'.

The Mohr-Coulomb failure envelope of CU00-1 is compared to the envelope of CU05-01. It is chosen to compare the results from series 1 because in series 2 failure did not occur for sample CU05-02 and therefore it is not possible to derive the circles of Mohr for this particular test. Since sands are considered to be non-cohesive, a triaxial test at one confining pressure is enough to determine the friction angle for test CU00-1. In Figure 6.13 the total and effective stress circles of Mohr for test CU00-1 are shown, based on the minor and major principal stresses at failure. The Mohr-Coulomb failure envelope is drawn tangent to the effective stress circle and through the origin. The envelope follows the Critical state failure line which means that the effective friction angle (ϕ') is equal to the Critical state friction angle (ϕ'_{cs}). Additionally, the effective stress circles at a confining pressure of 50 kPa and 100 kPa, for sand treated with 0.5% of Al-OM flocs, are shown in Figure 6.14. The Mohr-Coulomb failure envelope, tangent to both circles, is drawn in the same Figure. It can be seen that this line passes the y-axis at 60 kPa. This indicates a cohesion of 60 kPa of sample CU05-1. The effective friction angle of 25.87 ° is determined from the slope if the Mohr-Coulomb failure envelope and listed in Table 6.6. The derived friction angle is lower than of test CU00-1. This could be do to a flaw in test CU05-1 as mentioned in Section 6.3.

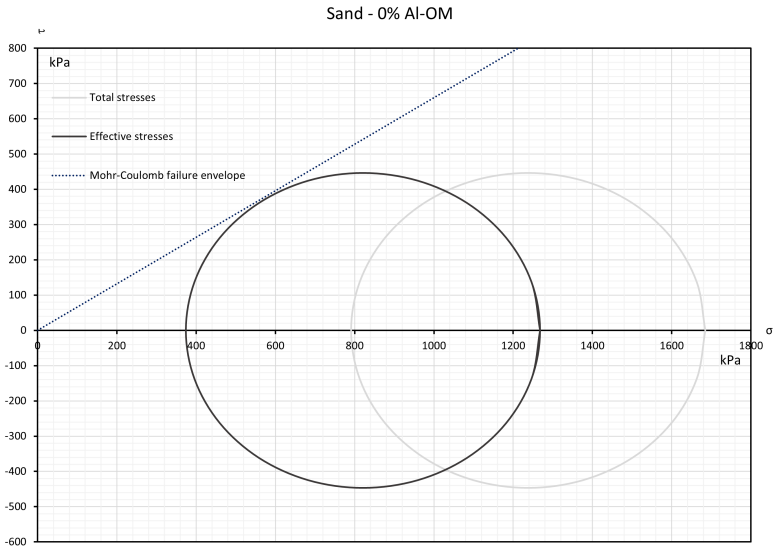

Figure 6.13: The Mohr-Coulomb failure envelope from sample CU00-1. Derived by drawing a line tangent to the effective stress circle and through the origin.

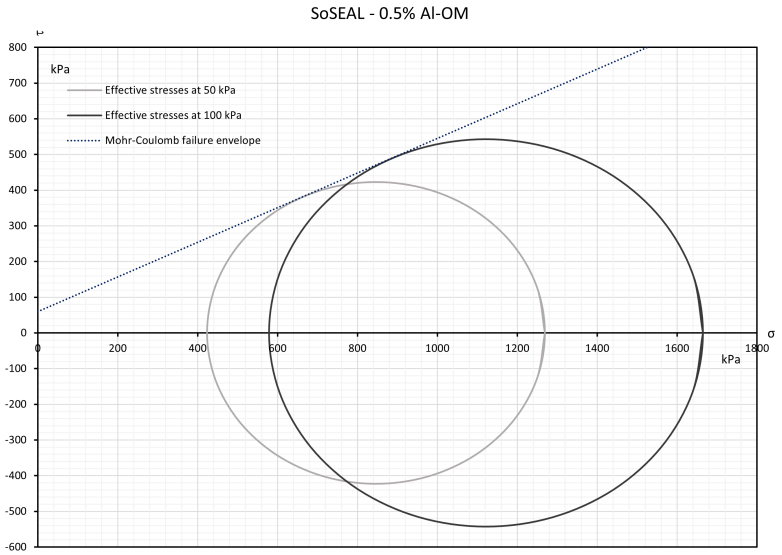

Figure 6.14: The Mohr-Coulomb failure envelope of sample CU05-1. Derived by drawing a line tangent to the effective stress circle at 50 kPa and 100 kPa.

Test No	c' $[kPa]$	ϕ' [°]
CU00-1	(−)	33.44
CU05-1	60	25.87

Table 6.6: The shear strength parameters derived from the Mohr-Coulomb failure envelopes of test CU00-1 and CU05-1.

The Mohr circles from the other tests are listed in Appendix F. Considering that these test are only executed under one confining pressure, the Mohr-Coulomb failure envelopes are not drawn.

6.4. Microscopy Examination

Lastly, a micro scale examination is performed to directly observe the characteristics of particles as well as the degree and composition of bonding between particles and porous medium. Scanning Electron Microscopy (SEM) is used to make images and develop component distribution diagrams. Samples in both vacuum and wet conditions are analyzed.

6.4.1. Effect of SoSEAL flocs on sand grains aggregation

In Figure 6.15 images made in vacuum conditions of samples with rising concentrations of Al-OM flocs are shown. B15 sand without Al-OM flocs is depicted in Figure 6.15a. Here, grains of similar sizes and shapes are evident, which corresponds with the steep curve in its particle size distribution diagram (Figure 4.1). The presence of small asperities, which serve as potential nucleation sites for Al-OM flocs, are also visible. In the left hand corner of Figure 6.15b a distinct cluster of grains is visible, seemingly held together by gravity. This aggregation phenomenon becomes more pronounced in samples with a higher percentage of Al-OM flocs. Figure 6.15d reveals additional clusters and individual sand grains are no longer discernible.

Upon closer inspection of an individual aggregate of grains (Figure 6.16), one can observe that the grains are coated with layer in a darker shade of grey. This coating is evident on the surface of the sand grains and appears to have a crust-like nature (Figure 6.16b). While many particles are connected, it is not really clear how the Al-OM flocs function at particle contacts, as the "crust" seems to be cracked. This cracking may be attributed to the vacuum conditions inside the SEM. The coating is not observed when looking at pure sand grains (Figure 6.15a). This observation suggests that the crust formed on the grains may be the result of Al-OM flocculation and precipitation onto grains.

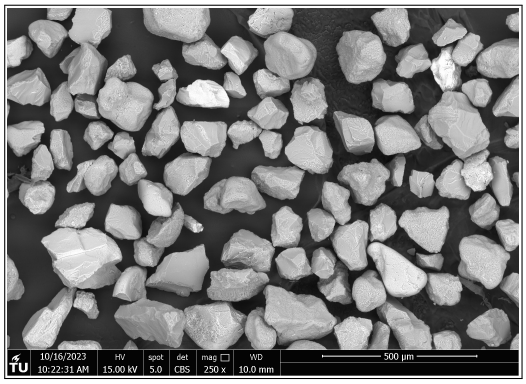

(a) Sand 0% Al-OM flocs.

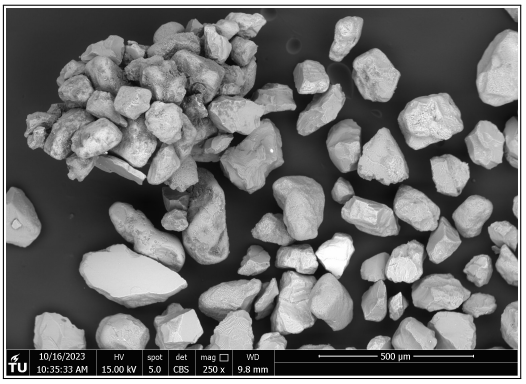

(b) SoSEAL 0.1 % Al-OM flocs.

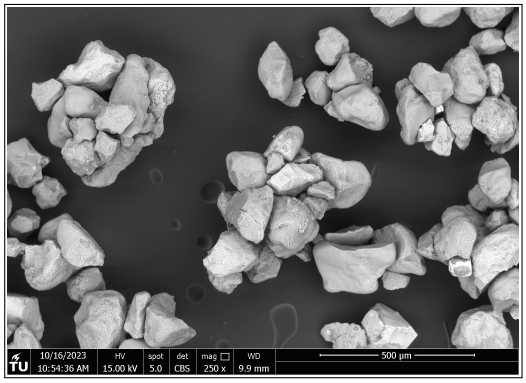

(c) SoSEAL 0.5 % Al-OM flocs.

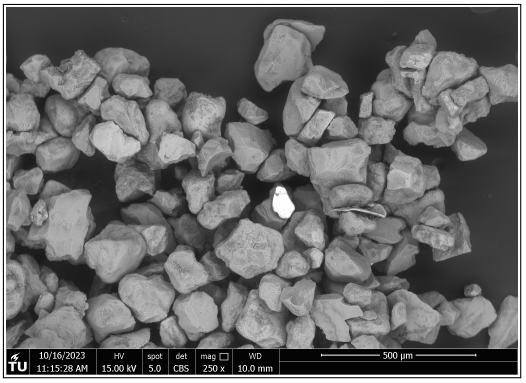

(d) SoSEAL 1 % Al-OM flocs.

Figure 6.15: SEM images of samples with different concentrations of Al-OM flocs in sand.

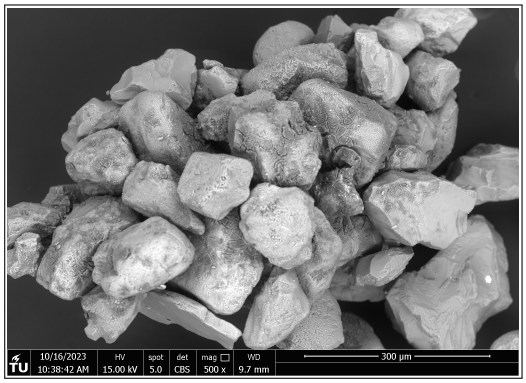

(a) A cluster of grains at 300 μm.

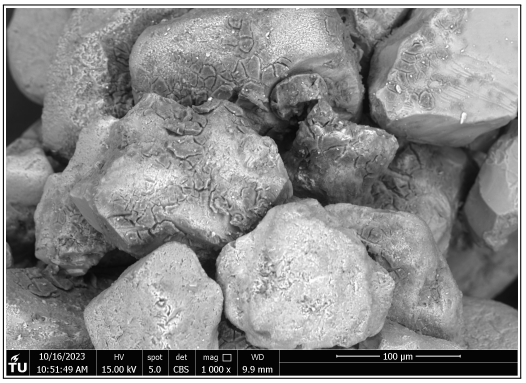

(b) A cluster of grains at 100 μm.

Figure 6.16: A cluster of grains retrieved from sample CU01.

It can be confirmed when examining the component distribution diagram of the sample without Al-OM flocs and comparing it to the samples with flocs. The component distribution diagrams of all samples are given in Appendix G. From this it is seen that the pure sand mostly consists of silica (Si). Other elements such as magnesium (Mg), aluminium (Al), iron (Fe), kalium (K) and carbon (C) are found in very small fractions. In the samples with Al-OM flocs, higher percentages of aluminium and also chloride (Cl) are detected. This is unsurprising, given that the flocs are formed through the reaction of organic material with aluminium chloride hexahydrate. But because chloride is predominantly present in the water, which is mostly evaporated in the SEM, its presence is much lower compared to aluminium. The diagrams also reveal that carbon is not indicative for detecting Al-OM flocs. Due to the carbon sticker used in sample preparation, carbon is present in all diagrams.

Test No	Compnd %		
	C	Al	Cl
CU00	13.66	0.98	–
CU01	25.13	2.88	0.12
CU05	11.38	6.01	0.13
CU10	27.22	4.56	0.33

Table 6.7: Component distribution of carbon, aluminium and chloride of samples with different concentrations of Al-OM flocs in sand.

As a result of the agglomeration of the sand grains, it is impractical to obtain SEM images and composition diagrams for individual grains, except for the sand sample without Al-OM flocs. Consequently, establishing a direct relationship between the percentage of Al-OM flocs and their composition diagram is not feasible. In all instances, the diagrams are derived from a cluster of grains. A summary of the distribution of carbon, aluminium and chloride is given in Table 6.7. The only discernible distinction is that samples with lower concentrations of flocs exhibit fewer visible clusters. Nevertheless, the diagrams allow for a differentiation between samples that don't contain Al-OM flocs and those who do contain Al-OM flocs.

6.4.2. Particle contact

A more detailed examination of the flocs and sand grains is conducted to analyse their interaction with each other. In Figure 6.17, 6.18 and 6.19 closer images of the particle contacts are shown. It is evident that the contact between grains is not smooth and is irregular in shape (Figure 6.17b and 6.19b). In Figure 6.18b, the darker shade of grey coating comes into contact between two grains. This coating exhibits its crusty nature and seems to be curled up. It almost appears that the contacts between grains is torn. This can be clarified by the fact that the samples are tested in vacuum. The water present in the samples is vaporized, resulting in the crusty and torn appearance of the Al-OM coating. Hence, the analysis of particle contact is also conducted under wet conditions.

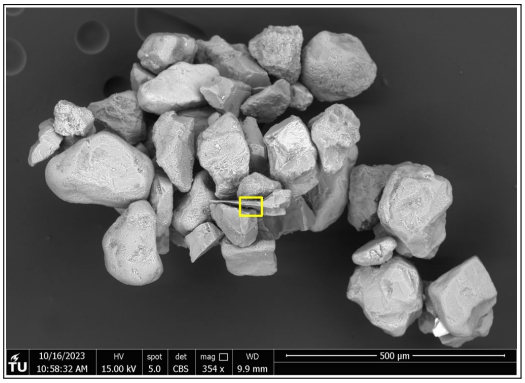

(a) A cluster of grains at 500 μm.

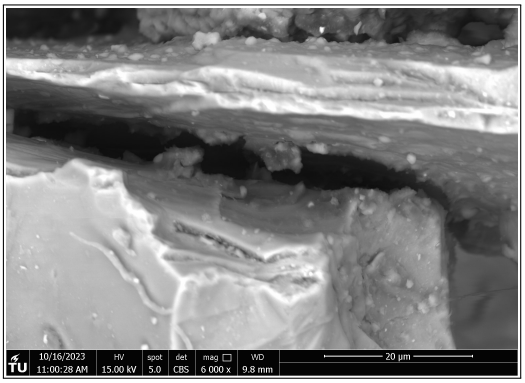

(b) Particle contact at 20 μm.

Figure 6.17: A cluster of grains retrieved from sample CU05.

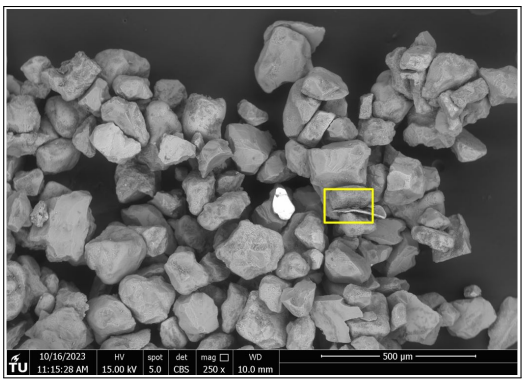

(a) Clusters of grains at 500 μm.

(b) Particle contact at 50 μm.

Figure 6.18: A cluster of grains retrieved from sample CU10.

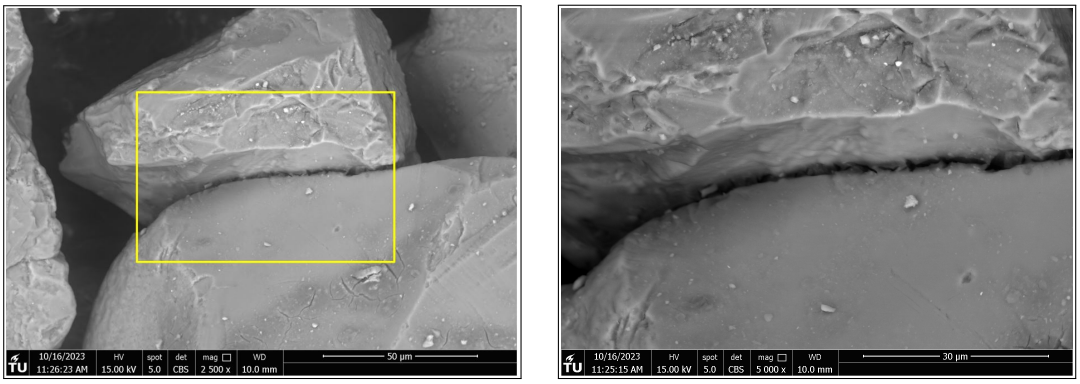

(a) Particle contact at 50 μm.

(b) Particle contact at 30 μm.

Figure 6.19: Particle contact retrieved from sample CU10.

To examine the impact of Al-OM flocs on the interaction between sand grains, an analysis under wet conditions is conducted. Images of samples of pure sand (CU00) and sand with 1 % Al-OM flocs (CU10) are made. In Figure 6.20, pure sand grains are observed under an increasing pressure in the SEM in the order of mbar. The black area surrounding the grains represents water. It is noticeable that as the pressure in the SEM rises, the presence of water around the grains intensifies.

A similar scenario is depicted in Figure 6.21c, although with a smaller quantity of water. Here, it is evident that the water originates primarily from the connections between the grains. In contrast, Figure 6.20 does not reveal this connection between grains, and the water appears more evenly distributed around the grains.

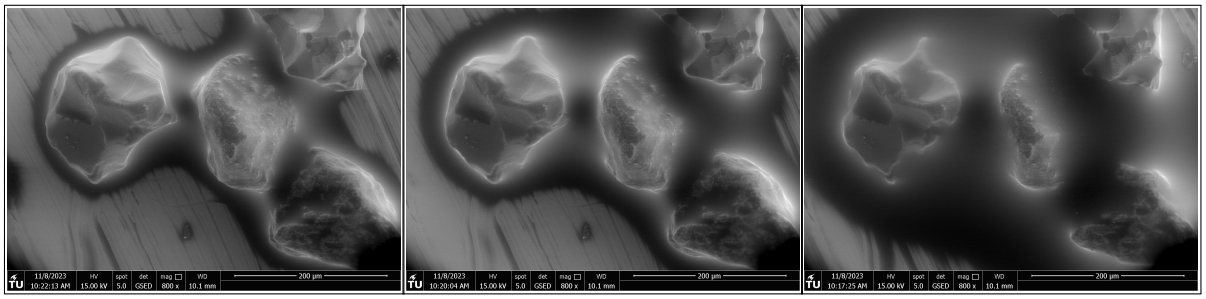

(a) .

(b) .

(c) .

Figure 6.20: Sand grains under an increasing pressure in the SEM. Retrieved from sample CU00.

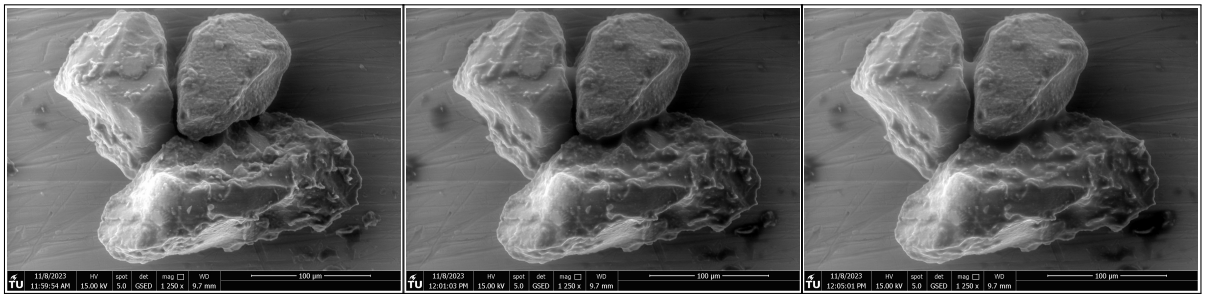

(a) .

(b) .

(c) .

Figure 6.21: Sand grains mixed with Al-OM flocs under an increasing pressure in the SEM. Retrieved from sample CU10.

In Figure 6.22 a closer examination of particle-particle interaction is depicted. The images reveal the highly irregular surface of the grains, contrasting with the crust-like nature observed in the dry samples. Additionally, the images show discernible connections between the grains.

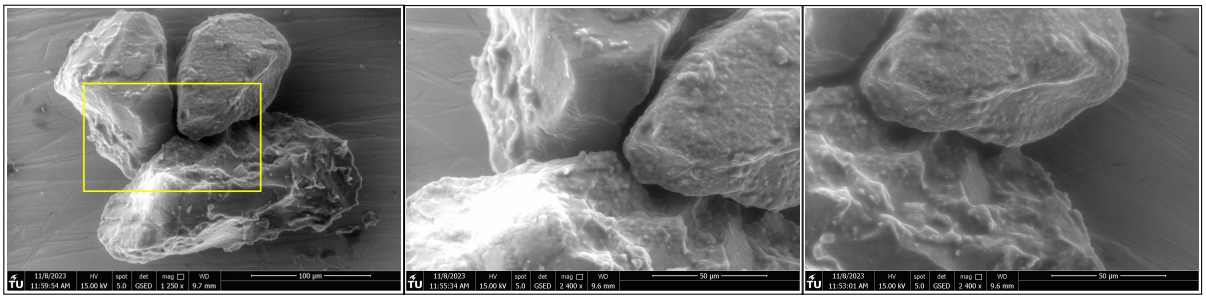

(a) . (b) . (c) .

Figure 6.22: Particle contact under wet conditions. Retrieved from sample CU10.

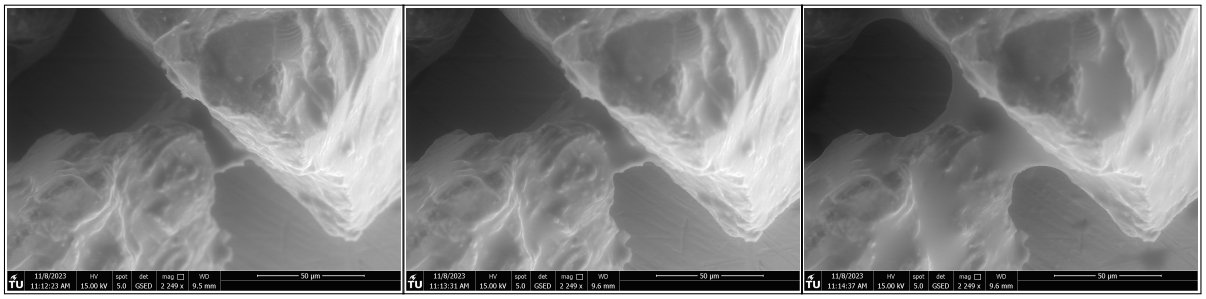

(a) . (b) . (c) .

Figure 6.23: Particle contact under wet conditions. Retrieved from sample CU10.

The detailed illustration of water expanding from particle contact is presented in Figure 6.23. This figure distinctly reveals a connection between two grains. As the pressure rises, the water volume in liquid state expands, progressing from Subfigure a to c. The images demonstrate the growth of water at the particle contact point between the grains, eventually surrounding the grains.

6.4.3. Comparison with a SoSEAL injected sample

Lastly, SEM images are made from a sample extracted during a full-scale laboratory experiment directed by Tauw and Heijmans. This particular sample undergoes SEM analysis to investigate how a specimen produced under 'real-life' conditions - such as injecting SoSEAL into sand rather than manual hand mixing - compares to the lab-made samples analyzed in this report. The exact percentage of Al-OM flocs in this sand is unclear, as by injecting the distribution of flocs differs. Figure 6.24 reveals the sand's cohesive clumping, resembling the patterns observed in the samples subjected to testing in this report. Closer inspection of an individual clod exposes its crusted nature, providing clear evidence of the presence of SoSEAL. Because the amount of clods is quite extended and not many single sand grains are seen, it is expected that the percentage of SoSEAL injected in this sand is > 0.1%.

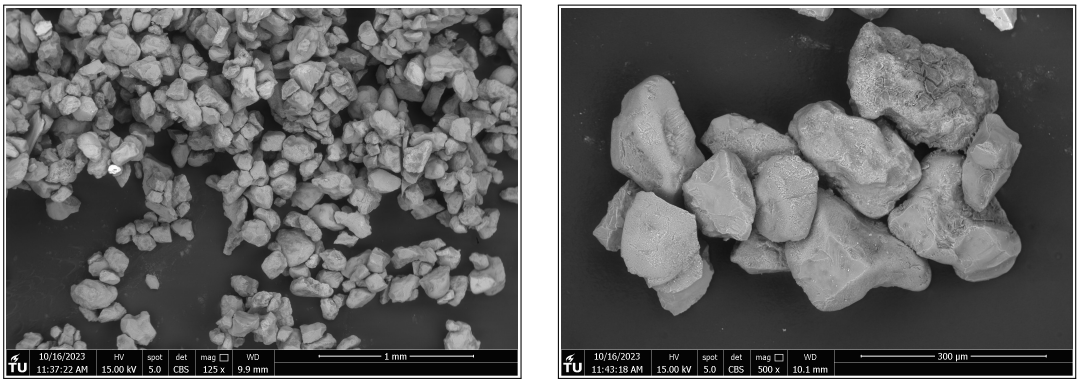

(a) Multiple clods at 1000 μm. (b) A clod of grains at 300 μm.

Figure 6.24: SEM images retrieved from a full-scale lab experiment at the TU Delft, directed by Tauw and Heijnams.

7

Discussion

While navigating through the complexities of the research results, attention is payed to the limitations encountered. In this Chapter, a comprehensive discussion of the findings obtained through this study will be provided. Different aspects of the experimental implementation and variations within the results are examined.

7.1. Test characteristics

Proctor's test was used to determine the maximum dry density and corresponding moisture content of the different samples tested with the triaxial test. Surprisingly, the porosity and voids ratio calculated from the results lay very close together as listed in Table 4.5. It was expected that an increasing percentage of Al-OM flocs in sand would lead to a reduction in both porosity and voids ratio. The expectation stems from the presumed clogging of the pore throats between sand grains by the introduced flocs. However, the observed proximity of maximum dry density and the related 95% values suggest that porosity and voids ratio remain within a similar range. The similarity in porosity across all samples could be the result of the force-induced air release. It is assumed that the untreated sand has reached optimal compaction, resulting in the lowest porosity. While the precise density of the Al-OM flocs remains unknown, it is evident that these flocs are significantly smaller than the sand grains. The addition of flocs is expected to influence the sand's porosity, but the observed effect appears to be relatively minimal. Additionally, higher percentages of flocs in sand may pose challenge in compacting the samples. The balance between the ease of compaction for samples with lower percentages of flocs, allowing for more significant air release, and the difficulty in compacting samples with higher floc percentages, may be the cause of the similar porosities and void ratios.

Another influencing factor is the assumption of a specific gravity of 2.65 g/cm^3 for all samples in porosity calculations. This assumption does not differentiate between varying floc percentages. In reality, specific gravity is a property of soil solids, and soils with a higher percentage of organic material may exhibit a lower specific gravity. A lower specific gravity would lead to a decrease in porosity. However, the added organic material has a maximum of $< 1\%$ of the soil solids. It is expected that this would have a negligible influence on the specific gravity and thus the porosity calculations.

7.2. Test procedure

During the execution of the tests, several challenges and considerations emerged. Firstly, the samples were molded using a spilt-part mold. This is a process which typically involves allowing the compacted samples to mature after compaction for equalization of pore pressure arises during the molding. However, due to the fragility of the samples, they were placed in the triaxial cell immediately after they were trimmed out of the mold. This immediate placement might have led to uneven distribution of pore pressure among the samples, causing difficulties in saturation the samples. This is resolved by flushing. One alternative to address the issue of complete saturation is using a soluble gas like CO_2 to displace air within the sample. Although this approach can introduce other unknown effective stresses in the sample.

Another notable issue involved failure occuring at connection points between layers. In the preparation of the test samples, soil is compacted in three layers and connections are made by nothing each layer. Unexpectedly, in test CU10-2, the sample did not fail along a diagonal shear plane, as observed in other tests, but exhibited a horizontal failure plane at approximately 1/3 of the sample's height as can be seen in Figure 7.1. This occurrence prompted a critical examination

to the used method in the sample preparation, as it seems that the weakest point in this sample was the connection between layers. The horizontal failure plane observed in the sample can be evident for the lower peak deviatoric stress observed in the test results.

Figure 7.1: Horizontal fracture at 1/3 of the samples height. Retrieved from sample CU10-2.

Furthermore, it was not possible to measure the shear angle of the shear plane in the samples when they were removed from the triaxial cell. The shear plane became non-visible as the grains filled the space once the pressure was reduced. Consideration for future experiments could involve implementing a raster on the outside of the membrane, which surrounds the samples. A picture of the shear plane can be made at the end of the test before reducing the pressures inside the cell. From this the shear plane and angle can be reconstructed later on.

In test CU01-1, CU10-1, CU01-2 and CU05-3, the maximum load value of the triaxial cell was reached, evident in the bumps seen in their graphs displayed in Figures 6.8, 6.9 and 6.11. In the case of test CU05-2, failure could not even occur before the load value was exceeded. These instances highlight the physical limitations of the triaxial cell used, suggesting that future research to strength and stiffness properties of SoSEAL may benefit from employing a larger triaxial cell with greater capacities.

Overall, it is imperative to acknowledge that shear strength is not a universal property of soil; rather, it depends on various factors. In the laboratory setting, shear strength is measured under defined conditions. Factors such as mineralogy of grains, particle shape, stress changes during sample preparation, shearing rate and drainage conditions collectively influence the shearing properties of the samples.

7.3. Permeability measurements

The analysis of permeability measurements did not reveal a relationship between floc concentration and hydraulic conductivity reduction. The hydraulic conductivity reduction after the consolidation phase is calculated with the value of 4.11E-6 m/s, obtained from the untreated sand, as a baseline. The reduction in permeability relative to this baseline is shown in Figure 6.4b. Notably, all three values hover around 1, showing that there is no significant reduction in permeability. When comparing the hydraulic conductivity values of SoSEAL with relevant research, it is observed that the values fall in the order of 1E-6 m/s. Figure 7.2a illustrates the outcomes of Ksat-tests conducted on various floc concentrations mixed with the same sand used in this study. For a floc content up to 0.01 g/g (e.g., 1% Al-OM flocs), the Ksat values measured are 2.10E-6 and 5.96E-6 m/s. This indicates that the variance in permeability reduction is not attributable to the measured permeability of the treated sand but rather to that of the untreated sand. In the Ksat-test conducted by Li et al. (2023b), the hydraulic conductivity of untreated sand is in the order of 1E-4 m/s, resulting in a reduction in hydraulic conductivity ranging from 10 to 100 up to 1% Al-OM flocs (see Figure 7.2b).

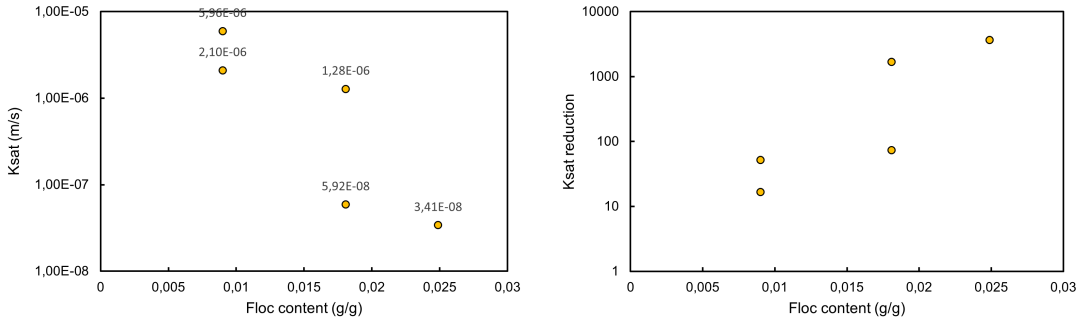

(a) Ksat (m/s) for different concentrations of Al-OM flocs.

(b) Ksat reduction for differenct concentrations of Al-OM flocs.

Figure 7.2: Ksat measurements for B15 sand treated with different concentrations of flocs. Copied from Li et al. (2023b).

Despite theoretical expectations on reduced permeability with an increased floc percentage, the observed results align with the calculated porosities from the Proctor's tests (Table 6.3). The consistent range of porosities support the credibility of the permeability measurements. It suggests that the sample preparation required for the triaxial tests renders it a less optimal method for conducting permeability measurements, especially for the untreated sand. Moreover, it was mentioned that the higher the concentration of flocs in sand, the harder it is to compact the sample. This could counteract the reduction of hydraulic conductivity, given that the height of the sample and, consequently, the flow path, becomes relatively longer with higher concentrations of Al-OM flocs in sand. This phenomenon is depicted in Figure 7.3, which illustrates the axial displacement at the end of consolidation for various floc contents of the samples. The graph indicates that untreated sand (0% Al-OM flocs) exhibits an axial displacement of 1.35 mm, while sand treated with 1% flocs shows a displacement of only 0.79 mm. This observation confirms that a higher concentration of flocs makes it more challenging to compact the sand.

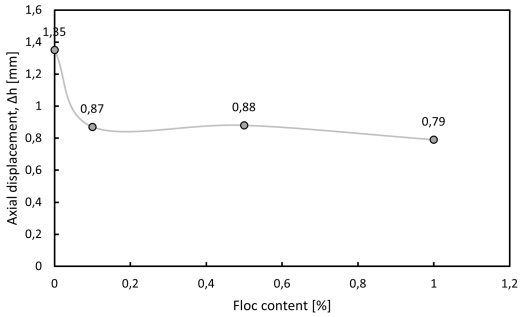

Figure 7.3: The axial displacement at the end of the consolidation over an increasing concentration of Al-OM flocs to sand.

Additionally, the uniform stress state applied to all samples during testing could contribute to the observed similarities in permeability measurements. This is the first experiment in which SoSEAL is tested under a prescribed load. The load applied on the SoSEAL might have a significant influence on the aimed permeability reduction. Nevertheless, given the various factors influencing the measurements and the fact that the measurements are conducted singularly, it is advisable not to place too much emphasis on the potential that permeability reduction is less significant at greater depth (e.g. a stress level of 100 kPa). To make an impression of the impact of confining pressure, the permeability measurements for test CU05-3 are incorpared, shown in Figure 7.4. The derived hydraulic conductivity at 50 kPa, half of that applied to the other samples, is 3.69E-6 m/s. This closely aligns with the hydraulic conductivity observed in test CU05-2, recorded at 3.05E-6 m/s. This outcome suggests that the applied pressure state may not be of big influence for the permeability reduction. Thorough and expanded research is required to determine whether this could be a cause for the similarities in permeability measured in this research and beyond.

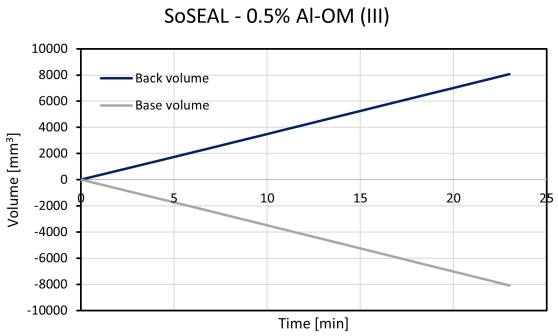

Figure 7.4: The measured back and base volume plotted against time after consolidation of test CU05-3.

Test No	k_v $[m/s]$	k_v $[m/d]$
CU05-3	3.69E-6	3.19E-1

Table 7.1: Derived hydraulic conductivity, k_v, of test CU05-3 after consolidation.

Another potential factor contributing to the observed similarities in results lies within the porous stones used in the triaxial tests. It is plausible that the grains and the Al-OM flocs clogged the voids of these porous stones, potentially causing the permeability of the clogged stones to be tested rather than the intended samples permeability. As a preventive measure, it is recommended to clean the porous stones thoroughly after each triaxial test by an ultrasonic cleanser to ensure that their permeability does not impact the accuracy of permeability measurements of the samples. Another option is to use multiple filter papers to prevent the fine particles' intrusion.

Lastly, it is important to note that the samples containing 1% Al-OM flocs were dried in the oven before molding. It is unclear what the effect of drying has on the interaction between aluminium and organic matter and if this effect is reversible. This could possibly explain the relative higher permeability measured in sample CU10-2 compared to sample CU01-2 and CU05-2, especially during the flushing phase.

7.4. Triaxial test results

7.4.1. Derivation of elastic parameters

With an increasing percentage of Al-OM flocs in sand, a parallel rise in elastic parameters is expected. This expectations align with the trends observed in Figure 6.10, affirming the correlation, particularly evident in Young's Modulus, E. The shear Modulus, G, seems to have a more stable increase of ≈ 2 times the untreated sand for all samples. However, noteworthy exceptions manifest in the results of test CU05-1 and CU10-2. An intriguing observation is the lower values of test CU05-1 compared to test CU01-1, paralleled by a similar pattern in test CU10-2 compared to test CU01-2 and CU05-2.

A noticeable pattern emerges in the graphs, indicating an increasing variability in results as the floc concentration rises. Test CU00-1 and CU00-2 exhibit closely aligned outcomes, as do test CU01-1 and CU01-2. Conversely, a rise in floc concentration corresponds with a notable divergence in results. Multiple factors could contribute to this phenomenon. Initial examination implicates potential variations in the test setup, with sample CU10-2 displaying a horizontal failure plane, indicative of failure at the connection between layers. CU05-1, on the other hand, may be influenced by an offset between the top cap and the load ram, resulting in uneven load distribution to the sample.

A second plausible factor is the time-dependent nature of SoSEAL. The continuous interaction between AL and OM forming flocs can involve processes of breakage and regrowth. In the duplicate test series, the use of the same samples as series 1 implies prolonged exposure, allowing the SoSEAL to "age" further. While this aging process seems to minimally impact lower concentrations, its effect on other samples remains unclear. Notably, a strength increase is observed in test CU05-2 compared to test CU05-1, while a decrease is evident in test CU10-2 relative to CU10-1. This supports the notion that a deviation in the test setup rather than the aging process of SoSEAL could be a contributing factor to the

observed differences. However, do to the inherent time intensity of the tests and the subsequent limitations to triplicate testing, drawing definitive conclusions remains challenging.

7.4.2. Derivation of strength parameters

From Figure 6.12 an evident increase is observed in the peak deviator stress, q, and the corresponding mean effective stress, p', across all samples compared to the untreated sand. Similar to the trend observed in elastic parameters, a rising floc percentage corresponds to an increased variability in results, potentially attributed to the factors mentioned earlier. The criterion of maximum or peak deviator stress is conventionally linked to failure. Instead of expressing the strength in terms of q, an alternative measure could be the principal stress ratio (σ'_1/σ'_3). The maximum value of this ratio does not necessarily occur at the same strain as the peak deviator stress. Furthermore, it is noteworthy that in tests where the outcomes deviate from expectations, e.g. test CU05-1 and CU10-2, the axial strain at failure is higher for sample CU05-1 compared to sample CU05-2, and for sample CU10-2, it aligns closely with sample CU10-1.

In addition a factor of interest is the necessity to dry the samples of test CU10-1 and CU10-2 before molding. This requirement stems from the manner that Al and OM are mixed with each other in solution, causing an automatic rise in the sand's water content once mixed. With an increase in the floc percentage, more water is introduced, surpassing the optimal water content and dry density required for soil compaction when the samples are molded. Consequently, in tests CU10-1 and 2, where the floc addition exceeded the optimum water content, the sand adhered to the mold's side, making it impossible to trim out the samples from the mold. Therefore, drying became imperative to get to the optimum water content in the samples. The question is how drying affects the Al-OM interaction with sand, particularly considering that test CU10-2 was executed later than test CU10-1. Drawing insights from Kaptein (2021), it is evident that different floc structures emerge when mixing flocs in a dry or wet state. Although the flocs in this study are not initially mixed dry, subsequent drying could influence the interaction between flocs and sand grains, as revealed in the SEM analysis. Moreover, it is not known if the phenomenon of drying is reversible. Meaning that it is not sure that once a dried sample is wetted again, it will show the same characteristics as before drying.

In cases where the specimen fails along a shear plane, the "wedging" effect resulting from the relative movement of the specimen's portions theoretically stretches the rubber membrane around it, potentially increasing the volume between the specimen and the membrane. In undrained tests, a negative pore pressure may develop, decreasing the pore pressure in the entire specimen and increasing the effective stress. This, in turn, could cause the shear strength to continue increasing with additional axial strain. However, since a decline in strength was observed in all specimens failing along a visible shear plane, this effect is not considered, and no membrane correction is applied for this.

7.4.3. Derivation of the Mohr-Coulomb failure envelope

In deriving the Mohr-Coulomb failure envelope for 0.5% Al-OM flocs added to sand, test series 1 is used. This choice was necessitated by the absence of failure in test series 2, making the derivation of the circle of Mohr and subsequent Mohr-Coulomb failure envelope impossible. However, the comparatively lower strength and stiffness properties exhibited by test CU05-1 compared to test CU05-2 raise questions about the accuracy of the derived effective shear strength parameters, c' and ϕ'. Although the results indicate an increase in cohesion compared to the non-cohesive untreated sand, there is a simultaneous decrease in the observed friction angle. To validate the drawn Mohr-Coulomb failure envelope, additional tests at higher confining pressures could be instrumental. Furthermore, is is advisable to conduct tests at different confining pressures for the remaining samples to verify the observed increase in cohesion.

7.5. SEM analysis

The component distribution diagrams made from clusters of grains presents a challenge in establishing a direct relation between the concentration of Al-OM flocs and their composition shown in the diagram. This difficulty arises because it is the amount of aggregates that variate with the concentration of flocs in sand, and not the clusters itself. An alternative approach, as depicted in Figure 6.15, involves creating diagrams from entire images, potentially avoiding the issue. However, this approach introduces a new challenge, the increased prominence of the carbon sticker in the composition diagram, making it also challenging to differentiate between samples with varying floc concentrations.

An additional challenge encountered during the wet testing of samples was the difficulty in creating a balance between wetting and drying. As pressure was increased, so did the water content in the sample. However, finding an equilibrium between adding water and allowing for evaporation proved to be challenging, making the establishment of a stable setup difficult. This is evident from Figure 6.20 and 6.21, where the amount of water presented in the images is not equal.

8

Conclusion and recommendations

8.1. Conclusion

The investigation into the effects of SoSEAL to the elastic and strength properties of sand has brought valuable insights. The main question: " *How do different concentrations of Al-OM flocs inpact the mechanical properties of sand when ex-situ mixed?*" is answered through a carefully executed test procedure involving Proctor's tests, permeability measurements and undrained consolidated triaxial tests. Firstly, the maximum dry density and corresponding moisture content were determined with Proctor's tests, essential for molding and compaction of the test samples. The Proctor's tests revealed a distinct peak in dry density with corresponding moisture content for sand mixed with Al-OM flocs, while the untreated sand prevailed a more flad peak from which the optimal condition was less easy to define. The porosities derived from the results of Proctor's test all hovered around 0.4 (-), indicating the minor impact of the Al-OM flocs to the porosity of the sand samples.

The undrained consolidated triaxial test procedure itself, involving saturation, consolidation and shearing, provided a detailed understanding of soil behaviour. The first phase, involved flushing the sample by creating a pressure difference between the top and bottom of the test specimen. This step was proved necessary to achieve sufficient saturation of the samples (B $\geq$0.95). Notably, the consolidation phase did not offer significant insights into the presence of Al-OM flocs, as all samples consolidated within a couple minutes.

Permeability measurements were added to the triaxial test procedure during the flushing phase and after the samples were consolidated. The measurements did not indicate a significant reduction in permeability with increasing percentage of Al-OM flocs. The vertical hydraulic conductivities are in the order of 10E-6 m/s. It is plausible that molding the samples had a great influence on the permeability measurements as the porosity of all samples are also within the same range. Another possible influence could be the stress level at which the samples were exposed or the fact that the tests were only performed singularly.

Elastic parameters, including Young's Modulus and shear Modulus, exhibited a general increase with an increasing concentration of Al-OM flocs to sand. The shear Modulus, G, increased by a magnitude between 2.09-2.18 compared to the untreated sand. Young's Modulus, E, increased by a magnitude between 2.11-2.62, although exceptions such as test CU05-1 and CU10-2 were observed. Strength parameters, determined through the maximum deviatoric stress, q, at failure, showed an overall increase with higher concentrations of Al-OM flocs, but expectations were noted in specific tests. Strength increase, in terms of q, by a magnitude of 1.38 - 2.07 compared to untreated sand have been found. Showing that the interaction of Al-OM flocs with sand grains has a significant effect on the strength and elastic properties. These findings contribute to the broader understanding of how Al-OM flocs influence the mechanical properties of sand. The variations observed in test results underline the complexity of influencing factors like compaction challenges and localized failures.

From microscale examination with the SEM, this observed strength increase can be attributed to the cohesion between sand grains, evident in the formation of grain clusters attributed to the rising percentage of Al-OM flocs. These flocs are presented as a dark-colored crust on the sand grains, effectively binding lose grains together into aggregates. A sample retrieved from a full-scale lab experiment involving the injection of SoSEAL confirm real-world conditions revealed a

comparable formation of clusters. This observation underscores the potential increase in strength and elastic properties in sand injected with SoSEAL, aligning with findings from laboratory-scale investigations.

As SoSEAL has the potential to improve strength properties of sand, it can impact design criteria for dyke improvement, providing enhanced resistance against erosion. Additionally, the observed increase in cohesion, as demonstrated with the Mohr-Coulomb failure envelope derived from test CU05-1 and CU05-3, suggest that SoSEAL influences other conditions necessary for Backwards Erosion Piping. Namely, a non-cohesive soil covered by a low permeable cohesive layer. Since the sand layer would not longer be non-cohesive, this condition is no longer valid.

8.2. Recommendations for further research

While this study provides valuable groundwork for understanding the influence of Al-OM flocs on sand properties, future research both within and beyond the current research scope is advisable. Within the scope of this particular triaxial test setup, it is recommended to expand the experimental trials, tripling tests to mitigate the variability observed in the current two sets of tests. Additionally, employing a larger triaxial cell with greater capacity is needed, given that the current cell's capacity was surpassed multiple times during the tests. To delve deeper into the impact of Al-OM flocs on the cohesion between grains, as observed in the SEM analysis, extended research into the Mohr-Coulomb failure envelopes of the different samples is suggested. This involves conducting tests under different confining pressures. In order to gain a deeper understanding of how the stress state affects permeability, it is recommended to carry out additional permeability measurements, ideally under varying confining pressures. This would contribute to the hypothesis that the permeability reduction observed with the introduction of SoSEAL is influenced by its stress state.

Expanding the scope, conducting triaxial tests on field-retrieved samples would provide valuable insights, verifying the strength and elastic improvement not only in laboratory conditions with homogeneously hand-mixed flocs and sand but also with injected flocs in sand. Exploring different soils, especially those with a broader range of grain sizes, could simulate a more real-life scenario. Exploring the impact of drying SoSEAL is another significant aspect for comprehending its mechanical properties. Observable shrinkage occurs when SoSEAL is exposed to heat, yet the implications on its mechanical properties remains unclear, and the reversibility of this process is uncertain.

Beyond the scope of this research, a deeper examination of the coagulation mechanism of Al and OM would be of interest. Understanding the zeta potential under different pH conditions could shed light on the dominant coagulation mechanisms; charge neutralization, sweeping and bridging. Investigation at which zeta potential and pH the bridging mechanism becomes predominant would be of interest, as bridging is known to be the strongest bonding of the three mechanisms mentioned. Moreover, exploring the regrowth potential of flocs is crucial. Previous research of Wiersma (2019) has investigated the regrowth after breakage by introducing and additional dosage of aluminium. But this was under conditions where the flocs were already fully grown. It would be valuable to explore the regrowth potential under lower M/C ratios, especially when the flocs are still in the growing phase when broken. A potential test procedure for a jar test setup is listed in Table 8.1. Here, the influence of M/C ratio, breakage phase and addition of second dosage would be explored.

Experiment	**M/C ratio** [-]	**breakage phase** [-]	**Second dosage Al**
1.	0.02	when fully grown	no
	0.03	when fully grown	no
	0.04	when fully grown	no
	0.06	when fully grown	no
2.	0.02	Initial phase	no
	0.03	Initial phase	no
	0.04	Initial phase	no
	0.06	Initial phase	no
3.	0.02	To be determined	yes
	0.03	””	yes
	0.04	””	yes
	0.06	””	yes

Table 8.1: Potential test procedure for a jartest setup.

Bibliography

Baalousha, M. and Motelica-Heino, M. and Le Coustumer, P., . Conformation and size of humic substances: Effects of major cation concentration and type, ph, salinity, and residence time. *Colloids and Surfaces A: Physicochemical and Engineering Aspects*, 272:48–55, 2006. doi: 10.1016/j.colsurfa.2005.07.010.

Beek, V.M., . *Backward Erosion Piping: Initiation and Progression.* doctoral thesis, Delft University of Technology, 2015.

Bo, X. and Gao, B. and Peng, N. and Wang, Y. and Yue, Q. and Zhao, Y., . Coagulation performance and floc properties of compound bioflocculant-aluminum sulfate dual-coagulant in treating kaolin-humic acid solution. *Chemical Engineering Journal*, 173:400–406, 2011. doi: 10.1016/j.cej.2011.07.077.

Bonfiglio, C., . Hydraulic conductivity reduction induced by precipitation of aluminium-organic matter flocs in porous media, 2017.

Brinkgreve, R.B.J., . Soil behaviour under compression. Lecture slides, 2021. [Online: accessed on May 10, 2023].

Chow, S. and Roy, A. and Herduin, M. and Heins, E. and King, L. and Bienen, B. and O'Loughlin, C.D. and Gaudin, C. and Cassidy, M.J., . *Characterisation of UWA superfine silica sand.* 2019. doi: 10.26182/5d8c185bcd366.

Dejong, J. T. and Soga, K. and Kavazanjian, E. and Burns, S. and Van Paassen, L. A. and AL Qabany, A. and Aydilek, A. and Bang, S. S. and Burbank, M. and Caslake, L. F. and Chen, C. Y. and Cheng, X. and Chu, J. and Ciurli, S. and Esnault-Filet, A. and Fauriel, S. and Hamdan, N. and Hata, T. and Inagaki, Y. and Jefferis, S. and Kuo, M. and Laloui, L. and Larrahondo, J. and Manning, D. A. C. and Martinez, B. and Montoya, B. M. and Nelson, D. C. and Palomino, A. and Renforth, P. and Santamarina, J. C. and Seagren, E. A. and Tanyu, B. and Tsesarsky, M. and Weaver, T., . Biogeochemical processes and geotechnical applications: Progress, opportunities and challenges. *Géotechnique*, 63(4):287–301, 2013. doi: 10.1680/geot.SIP13.P.017.

DeJong, J.T. and Mortensen, B.M. and Martinez, B.C. and Nelson, D.C., . Bio-mediated soil improvement. *Ecological Engineering*, 36(2):197–210, 2010. doi: 10.1016/j.ecoleng.2008.12.029.

Duan, J. and Gregory, J., . Coagulation by hydrolysing metal salts. *Advances in Colloid and Interface Science*, 100-102: 475–502, 2003. doi: 10.1016/S0001-8686(02)00067-2.

Fookes, P.G., . Geology for engineers: the geological model, prediction and performance. *Quarterly Journal of Engineering Geology*, 30:293–424, 1997. doi: 10.1144/GSL.QJEG.1997.030.P4.02.

GDS, . Part one: Introduction to triaxial testing, 2023. URL `https://www.gdsinstruments.com/gds-products/gds-quasi-dynamic-triaxial-system`. [Online: accessed on October 30, 2023].

Gone Droh, L. and Kamagate, B. and Ligban, R. and Seidel, J. and Batiot, C. and Biemi, J., . Coagulation-flocculation treatment of a tropical surface water with alum for dissolved organic matter (dom) removal: Influence of alum dose and ph adjustment. *Journal of International Environmental Application and Science*, 3:247–257, 2008.

Gregory, J., . *Particles in Water.* Taylor & Francis, 2006.

Head, K.H., . *Manual of Soil Laboratory Testing.* John Wiley Sons, 1994.

Jeol, . Scanning electrion miscroscopes (sem), 2023. URL `https://www.jeol.com/products/science/sem.php`. [Online: accessed on November 17, 2023].

Kaptein, M.P.A., . Mixed in place permeability reductive layer through al and om precipitation, 2021.

Kim, J.H. and Lee, C. and Lee, E. and Lee, K.H. and Kwon, S. and Park, H. and Kim, H. and Jang, A., . The effect of re-aggregated floc by additional coagulant on membrane. *Journal of The Taiwan Institute of Chemical Engineers*, 44: 802–807, 2013. doi: 10.1016/j.jtice.2013.01.026.

Latini, C. and Zania, V., . *Triaxial tests in Fontainebleau sand.* doctoral thesis, Technical University of Denmark, 2017.

Laumann, S. and Zhou, J. and Heimovaara, T.J., . Aluminium-organic matter precipitation as a geoengineering tool for in situ permeability reduction in a porous media. pages 1689–1689, 2016.

Li, L. and Dieudonné, A.A.M. and VanBeek, V. and Heimovaara, T.J., . Applicability of a soseal barrier to mitigate backward erosion piping. Technical report, Hoogheemraadschap De Stichtse Rijnlanden, 2023a.

Li, L. and VanBeek, V. and Heimovaara, T.J. and Dieudonné, A.C, . Applicability of low-permeability barriers to mitigate backward erosion piping. in preparation. 2023b.

Li, T. and Zhu, Z. and Wang, D. and Yao, C. and Tang, H., . Characterization of floc size, strength and structure under various coagulation mechanisms. *Powder Technology*, 168(2):104–110, 2006. doi: 10.1016/j.powtec.2006.07.003.

Lundström, U.S. and VanBreemen, N. and Bain, D., . The podzolization process. a review. *Geoderma*, 94(2):91–107, 2000. doi: 10.1016/S0016-7061(99)00036-1.

Martinez, A. and Dejong, J.T., and Akin, I. and Aleali, A. and Arson, C. and Atkinson, J. and Bandini, P. and Baser, T. and Borela, R. and Boulanger, R. and Burrall, M. and Chen, Y. and Collins, C. and Cortes, D. and Dai, S. and Del Dottore, E. and Dorgan, K. and Fragaszy, R. and Frost, J.D. and Full, R. and Ghayoomi, M. and Goldman, D.I. and Gravish, N. and Guzman, I. L. and Hambleton, J. and Hawkes, E. and Helms, M. and Hu, D. and Huang, L. and Huang, S. and Hunt, C. and Irschick, D. and Lin, H.T. and Lingwall, B. and Marr, A. and Mazzolai, B. and McInroe, B. and Murthy, T. and O'Hara, K. and Porter, M. and Sadek, S. and Sanchez, M. and Santamarina, C. and Shao, L. and Sharp, J. and Stuart, H. and Stutz, H.H. and Summers, A. and Tao, J. and Tolley, M. and Treers, L. and Turnbull, K. and Valdes, R. and van Paassen, L. and Viggiani, G. and Wilson, D. and Wu, W. and Yu, X. and Zheng, J., . Bio-inspired geotechnical engineering: principles, current work, opportunities and challenges. *Géotechnique*, 72(8):687–705, 2022. doi: 10.1680/jgeot.20.P.170.

NwO, . Soil sealing by enhanced aluminium and dom leaching (soseal), 2014. URL `https://www.nwo.nl/en/projects/13883`. [Online: accessed on December 3, 2023].

Parry, R.H.G., . *Mohr Circles, Stress Paths and Geotechnics*. Spon Press, 2004.

Popma, J., . Engineering a horizontal layer of reduced permeability using al-dom precipitation, 2017.

Sanna, V., . Mobility of aluminium-om flocs in porous media and their ability to reduce the hydraulic conductivity, 2020.

Sauer, D. and Sponagel, H. and Sommer, M. and Giani, L. and Jahn, R. and Stahr, K., . Podzol: Soil of the year 2007. a review on its genesis, occurrence, and functions. *Journal of Plant Nutrition and Soil Science*, 170(5):581–597, 2007. doi: 10.1002/jpln.200700135.

Semmens, S. and Zhou, W., . Predicting backward erosion piping hazard, lower mississippi valley, usa. *Quarterly Journal of Engineering Geology and Hydrogeology*, 54(1):qjegh2020–035, 2021. doi: 10.1144/qjegh2020-035.

Su, Z. and Li, X. and Yang, Y., . Regrowth ability and coagulation behavior by second dose: Breakage during the initial flocculation phase. *Colloids and Surfaces A: Physicochemical and Engineering Aspects*, 527:109–114, 2017. doi: 10.1016/j.colsurfa.2017.05.034.

Suopajärvi, T., . *Functionalized Nanocelluloses in Wastewater Treatment Applications*. doctoral thesis, Univerisity of Oulu, 2015.

Tosco, T. and Papini, M.P. and Viggi, C.C. and Sethi, R., . Nanoscale zerovalent iron particles for groundwater remediation: a review. *Journal of Cleaner Production*, 77:10–21, 2014. ISSN 0959-6526. doi: https://doi.org/10.1016/j.jclepro.2013.12.026.

Ul-Hamid, A., . *A Beginners' Guide to Scanning Electron Microscopy*. 2018. doi: 10.1007/978-3-319-98482-7.

Verruijt, A., . *Soil Mechanics*. Vssd, 2001.

Wang, D. and Wu, R. and Jiang, Y. and Chow, C.W.K., . Characterization of floc structure and strength: Role of changing shear rates under various coagulation mechanisms. *Colloids and Surfaces A: Physicochemical and Engineering Aspects*, 379(1):36–42, 2011. doi: 10.1016/j.colsurfa.2010.11.048.

Wiersma, W., . Effect of shear stress on breakage and re-growth of aluminium- organic matter flocs, 2019.

Yu, W. and Gregory, J. and Campos, L., . The effect of additional coagulant on the re-growth of alum–kaolin flocs. *Separation and Purification Technology*, 74(3):305–309, 2010a. doi: 10.1016/j.seppur.2010.06.020.

Yu, W. and Gregory, J. and Campos, L.C., . Breakage and re-growth of flocs formed by charge neutralization using alum and polydadmac. *Water Research*, 44(13):3959–3965, 2010b. doi: 10.1016/j.watres.2010.04.032.

Zhang, A. and Dieudonné, A.C., . Effects of carbonate distribution pattern on the mechanical behaviour of bio-cemented sands: A dem study. *Computers and Geotechnics*, 154:105–152, 2023. ISSN 0266-352X. doi: https://doi.org/10.1016/j.compgeo.2022.105152.

Zhou, J., . *Development of a nature-based Geo-engineering solution to reduce soil permeability in-situ.* doctoral thesis, Delft Univeristy of Technology, 2020.

Zhou, J. and Laumann, S. and Heimovaara, T.J., . In situ precipitation of aluminum and organic matter as a geo-engineering tool to reduce soil permeability: A field test. *Geophysical Research Abstracts (online)*, 20, 2018. ISSN 1607-7962.

Zhou, J. and Laumann, S. and Heimovaara, T.J., . Applying aluminum-organic matter precipitates to reduce soil permeability in-situ: A field and modeling study. *Science of the Total Environment*, 662:99–109, 2019. doi: 10.1016/j.scitotenv.2019.01.109.

Zsolnay, A., . Dissolved organic matter: artefacts, definitions, and functions. *Geoderma*, 113(3):187–209, 2003. doi: 10.1016/S0016-7061(02)00361-0.

Appendices

A

Proctor's test results

		Determination No.						
0 % Al-OM	unit	1 (w=8%)	2 (w=10%)	3 (w=12%)	4 (w=14%)	5 (w=16%)	6 (w=18%)	7 (w=21%)
concentration flocs	g/kg	0	0	0	0	0	0	0
mass of mould + soil	kg	5.824	5.852	5.909	5.928	5.977	6.022	6.040
mass petri	g	47.75	46.02	43.30	51.73	45.89	45.49	45.89
mass petri + sand	g	76.54	79.31	73.40	88.52	93.23	86.24	115.27
mass sand	g	28.79	33.29	30.10	36.79	47.34	40.75	13.02
mass petri + sand after oven	g	74.74	76.91	71.05	85.21	87.56	80.43	102.25
mass of pore water	g	1.80	2.40	2.35	3.31	5.67	5.81	13.02
mass of soil solids	g	26.99	30.89	27.75	33.48	41.67	34.94	56.36
calculations								
mass compacted soil	g	1557	1585	1642	1661	1710	1775	1773
bulk density,	g/cm^3	1.647	1.677	1.737	1.757	1.809	1.857	1.876
water content, w	%	6.67	7.77	8.47	9.89	13.61	16.63	23.10
dry density, ρ_d	g/cm^3	1.54	1.56	1.60	1.60	1.59	1.59	1.52

Table A.1: Proctor's test results from sand 0% with Al-OM flocs.

		Determination No.				
0.1 % Al-OM	unit	1 (w=8%)	2 (w=11%)	3 (w=14%)	4 (w=17%)	5 (w=19%)
concentration flocs	g/kg	1	1	1	1	1
mass of mould + soil	kg	5.875	5.936	5.987	6.039	6.031
mass petri	g	43.34	46.55	45.51	51.75	44.81
mass petri + sand	g	83.29	85.50	82.00	94.70	103.31
mass sand	g	39.95	38.95	36.49	42.95	58.50
mass petri + sand after oven	g	80.43	81.44	77.28	87.7	91.96
mass of pore water	g	2.86	4.06	4.72	7.00	11.35
mass of soil solids	g	37.09	34.89	31.77	35.95	47.15
calculations						
mass compacted soil	g	1609	1670	1721	1773	1765
bulk density,	g	1.70	1.77	1.82	1.88	1.87
water content, w	g/cm^3	7.71	11.64	14.86	19.47	24.07
dry density, ρ_d	%	1.58	1.58	1.59	1.57	1.50

Table A.2: Proctor's test results from SoSEAL with 0.1% Al-OM flocs.

		Determinination No.				
0.5% Al-OM	unit	1 (w=8%)	2 (w=11%)	3 (w=14%)	4 (w=17%)	5 (w=19%)
concentration flocs	g/kg	5	5	5	5	5
mass of mould + soil	kg	5.947	6.004	6.042	6.019	6.012
mass of petri	g	51.75	45.97	44.82	49.56	45.48
mass of petri + sand	g	103.52	99.40	110.48	135.97	133.13
mass sand	g	51.77	53.43	65.66	86.41	87.65
mass of petri + sand after oven	g	98.22	92.61	100.14	119.49	115.13
mass of pore water	g	5.30	6.79	10.34	16.48	18.00
mass of soil solids	g	46.47	46.64	55.32	69.93	69.65
calculations						
mass compacted soil	kg	1.681	1.738	1.776	1.753	1.746
bulk density	g/cm^3	1.78	1.84	1.88	1.85	1.85
water content,w	%	11.41	14.56	18.69	23.57	25.84
dry density, ρ_d	g/cm^3	1.60	1.60	1.58	1.50	1.47

Table A.3: Proctor's test results from SoSEAL with 0.5% Al-OM flocs.

		Determination No.				
1% Al-OM	unit	1 (w=6%)	2 (w=8%)	3 (w=9%)	4 (w=11%)	5 (w=14%)
concentration flocs	g/kg	10	10	10	10	10
mass of mould + soil	kg	5.998	6.056	6.067	6.036	6.018
mass of petri	g	44.82	45.49	49.57	51.74	40.63
mass of petri + sand	g	73.77	97.25	111.73	111.69	88.70
mass sand	g	28.95	51.76	62.16	59.95	48.07
mass of petri + sand after oven	g	70.60	90.17	102.54	101.66	79.29
mass of pore water	g	3.17	7.08	9.19	10.03	9.41
mass of soil solids	g	25.78	44.68	52.97	49.92	38.66
calculations						
mass compacted soil	kg	1.732	1.790	1.801	1.770	1.752
bulk density	g/cm^3	1.83	1.89	1.91	1.87	1.85
water content,w	%	12.30	15.85	17.35	20.09	24.34
dry density, ρ_d	g/cm^3	1.63	1.63	1.62	1.56	1.49

Table A.4: Proctor's test results from SoSEAL with 1% Al-OM flocs.

B

Triaxial test specifications

Test No.	**Mass solids** [g]	**Mass water** [g]	**Mass after test** [g]	**Dry mass after test** [g]	**Moisture content** [g]	**Saturation pressure** [%]	**Consolidation pressure** [kPa]	**Confining pressure** [kPa]	**Comments:**
CU00-1	145.27	12.35	170.20	136.60	24.60	650	790	100	A clear shear band has been formed.
CU00-2	145.27	12.35	169.70	135.36	25.37	650	795	100	A clear shear band has been formed.
CU01-1	144.24	21.43	172.97	137.36	25.92	700	795	100	The test exceeded the maximum load value (1.8 kN).
CU01-2	144.24	21.43	176.55	141.62	24.66	650	795	100	The test exceeded the maximum load value (1.8 kN).
CU05-1	145.60	21.20	166.80	133.54	24.91	650	795	100	A clear shear band is visual and the sample is S-shaped. The sample contained its shape after the water has been removed from the cell. There is a small offset between the top cap and load ram.
CU05-2	145.60	21.20	179.10	144.15	24.25	650	795	100	The test exceeded the maximum load value (1.8 kN). The sample could not be tested until failure.
CU05-3	145.60	21.20	173.66					50	A clear shear band has been formed.
CU10-1	148.27	23.50	178.99	144.06	24.25	700	845	100	The sample took longer to saturate and a higher cell pressure was needed. The test exceeded the maximum load value (1.8 kN). The sample kept its shape after drying in the oven.
CU10-2	148.27	23.50	179.11	142.60	25.60	650	795	100	A localized shear band formed at 1/3 of the sample. The sample kept its shape after drying in the oven.

Table B.1: Triaxial test specifications.

C

Permeability measurements

C.1. Flushing phase

Test CU00-2		**unit**
Back pressure	541.84	kPa
Base pressure	544.63	kPa
Pressure difference, Δp	2.80	kPa
Axial displacement	1.26	mm
Heigth	80.34	mm
Diameter	38.6	mm
Area, A	1170.21	mm^2
discharge, q	184.33	mm^3/min
mean hydraulic gradient, i	3.55	[-]
Hydraulic conductivity, k_v	7.40E-7	m/s

Table C.1: Test specifications from permeability measurements during the flushing phase; sand 0% Al-OM flocs.

Test CU01-2		**unit**
Back pressure	591.23	kPa
Base pressure	594.62	kPa
Pressure difference, Δp	3.38	kPa
Axial displacement	0.81	mm
Heigth	80.79	mm
Diameter	38.6	mm
Area, A	1170.21	mm^2
discharge, q	148.42	mm^3/min
mean hydraulic gradient, i	4.27	[-]
Hydraulic conductivity, k_v	4.95E-7	m/s

Table C.2: Test specifications from permeability measurements during the flushing phase; SoSEAL 0.1 % Al-OM flocs.

Test CU05-2		**unit**
Begin		
Back pressure	590.59	kPa
Base pressure	595.47	kPa
Pressure difference, Δp	4.88	kPa
Axial displacement	0.77	mm
Heigth	80.83	mm
Diameter	38.6	mm
Area, A	1170.21	mm^2
discharge, q	77.53	mm^3/min
mean hydraulic gradient, i	6.16	[-]
Hydraulic conductivity, k_v	1.79E-7	m/s
End		
Back pressure	591.22	kPa
Base pressure	594.87	kPa
Pressure difference, Δp	3.64	kPa
Axial displacement	0.77	mm
Heigth	80.83	mm
Diameter	38.6	mm
Area, A	1170.21	mm^2
discharge, q	151.60	mm^3/min
mean hydraulic gradient, i	4.60	[-]
Hydraulic conductivity, k_v	4.69E-7	m/s

Table C.3: Test specifications from permeability measurements during the flushing phase; SoSEAL 0.5% Al-OM flocs.

Test CU10-2		**unit**
Back pressure	591.41	kPa
Base pressure	594.24	kPa
Pressure difference, Δp	2.84	kPa
Axial displacement	0.74	mm
Heigth	80.86	mm
Diameter	38.6	mm
Area, A	1170.21	mm^2
discharge, q	194.92	mm^3/min
mean hydraulic gradient, i	3.58	[-]
Hydraulic conductivity, k_v	7.75E-7	m/s

Table C.4: Test specifications from permeability measurements during the flushing phase; SoSEAL 1% Al-OM flocs.

C.2. After consolidation

Test CU00-2		**unit**
Confining pressure	100	kPa
Back pressure	690.76	kPa
Base pressure	689.73	kPa
Pressure difference, Δp	1.03	kPa
Axial displacement	1.35	mm
Heigth	80.25	mm
Diameter	38.6	mm
Area, A	1170.21	mm^2
discharge, q	377.22	mm^3/min
mean hydraulic gradient, i	1.31	[-]
Hydraulic conductivity, k_v	4.11E-6	m/s

Table C.5: Test specifications from permeability measurements after the consolidation phase; sand 0% Al-OM flocs.

Test CU01-2		**unit**
Confining pressure	100	kPa
Back pressure	690.79	kPa
Base pressure	689.81	kPa
Pressure difference, Δp	0.98	kPa
Axial displacement	0.87	mm
Heigth	80.73	mm
Diameter	38.6	mm
Area, A	1170.21	mm^2
discharge, q	323.02	mm^3/min
mean hydraulic gradient, i	1.24	[-]
Hydraulic conductivity, k_v	3.71E-6	m/s

Table C.6: Test specifications from permeability measurements after the consolidation phase; SoSEAL 0.1% Al-OM flocs.

Test CU05-2		**unit**
Confining pressure	100	kPa
Back pressure	690.94	kPa
Base pressure	689.69	kPa
Pressure difference, Δp	1.25	kPa
Axial displacement	0.88	mm
Heigth	80.72	mm
Diameter	38.6	mm
Area, A	1170.21	mm^2
discharge, q	337.5	mm^3/min
mean hydraulic gradient, i	1.58	[-]
Hydraulic conductivity, k_v	3.05E-6	m/s

Table C.7: Test specifications from permeability measurements after the consolidation phase; SoSEAL 0.5% Al-OM flocs.

Test CU10-2		**unit**
Confining pressure	100	kPa
Back pressure	690.77	kPa
Base pressure	689.69	kPa
Pressure difference, Δp	1.08	kPa
Axial displacement	0.79	mm
Heigth	80.81	mm
Diameter	38.6	mm
Area, A	1170.21	mm^2
discharge, q	360	mm^3/min
mean hydraulic gradient, i	1.36	[-]
Hydraulic conductivity, k_v	3.77E-6	m/s

Table C.8: Test specifications from permeability measurements after the consolidation phase; SoSEAL 1% Al-OM flocs.

Test CU05-3		**unit**
Confining pressure	50	kPa
Back pressure	645.54	kPa
Base pressure	644.47	kPa
Pressure difference, Δp	1.07	kPa
Axial displacement	1.06	mm
Heigth	80.54	mm
Diameter	38.6	mm
Area, A	1170.21	mm^2
discharge, q	351.69	mm^3/min
mean hydraulic gradient, i	1.36	[-]
Hydraulic conductivity, k_v	3.69E-6	m/s

Table C.9: Test specifications from permeability measurements after the consolidation phase; SoSEAL 0.5% Al-OM flocs, at 50 kPa confining pressure.

D

Derivation of elastic parameters

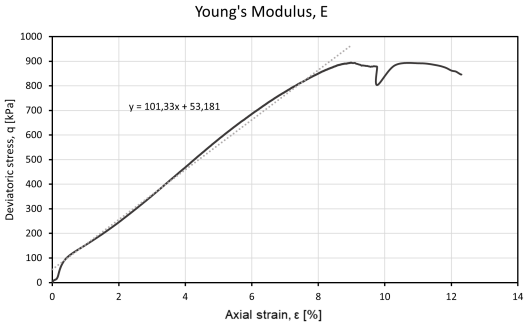

(a) Sand 0% Al-OM flocs serie 1.

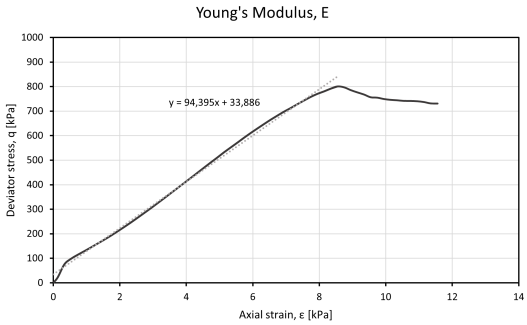

(b) Sand 0% Al-OM flocs serie 2.

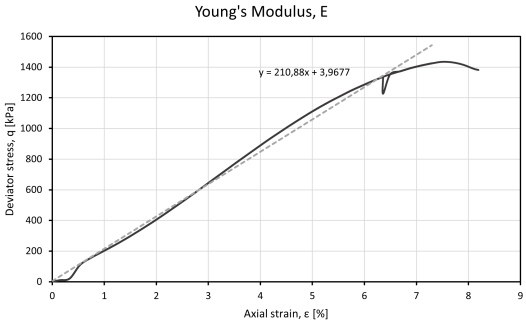

(c) SoSEAL 0.1% Al-OM flocs serie 1.

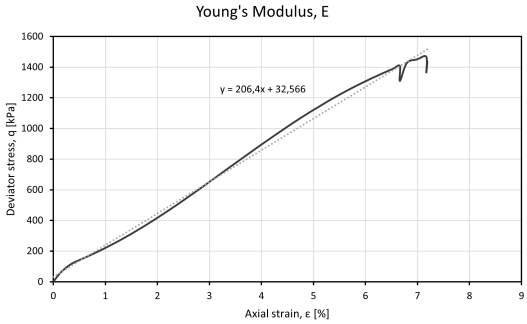

(d) SoSEAL 0.1% Al-OM flocs serie 2.

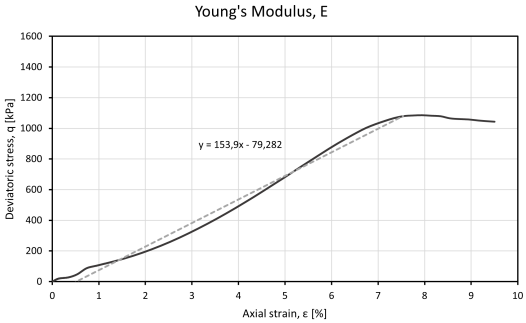

(e) SoSEAL 0.5% Al-OM flocs serie 1.

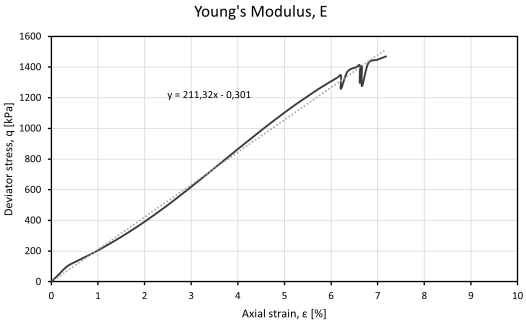

(f) SoSEAL 0.5% Al-OM flocs serie 2.

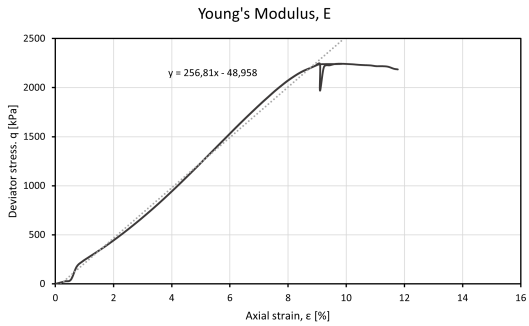

(g) SoSEAL 1% Al-OM flocs serie 1.

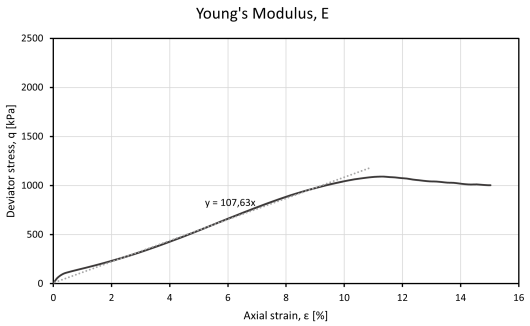

(h) SoSEAL 1% Al-OM flocs serie 2.

Figure D.1: Derivation of Young's Modulus, E, from the shearing phase of the triaxial test series.

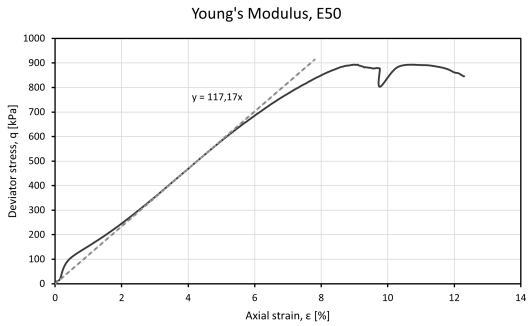

(a) Sand 0% Al-OM flocs serie 1.

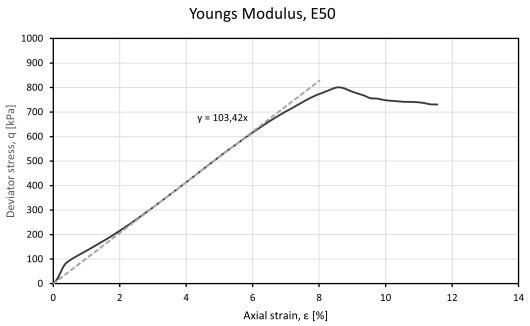

(b) Sand 0% Al-OM flocs serie 2.

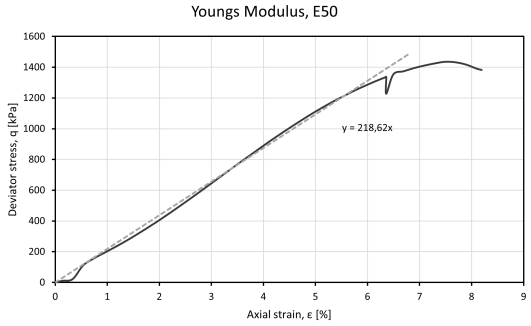

(c) SoSEAL 0.1% Al-OM flocs serie 1.

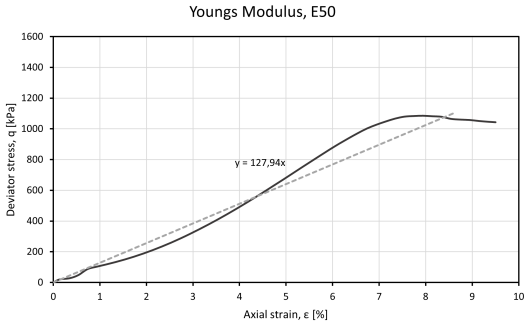

(d) SoSEAL 0.5% Al-OM flocs serie 1.

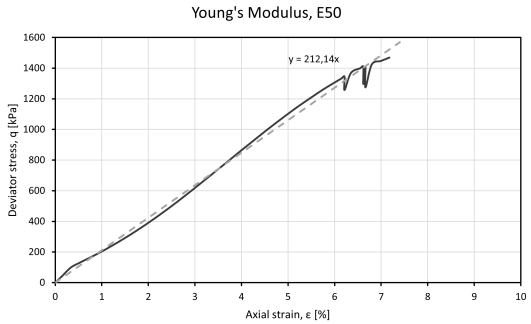

(e) SoSEAL 0.5% Al-OM flocs serie 2.

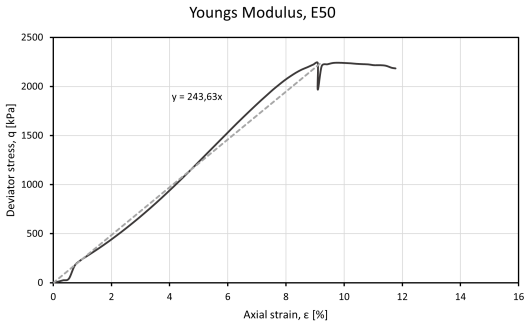

(f) SoSEAL 1% Al-OM flocs serie 1.

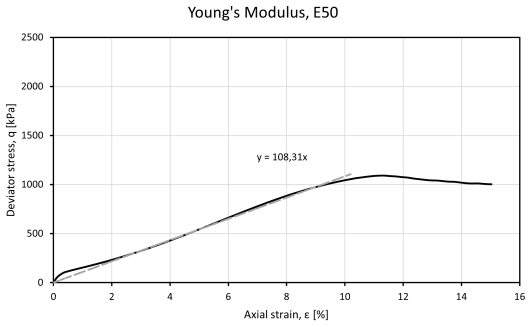

(g) SoSEAL 1% Al-OM flocs serie 2.

Figure D.2: Derivation of the secant Young's Modulus, $E50$, from the shearing phase of the triaxial test series.

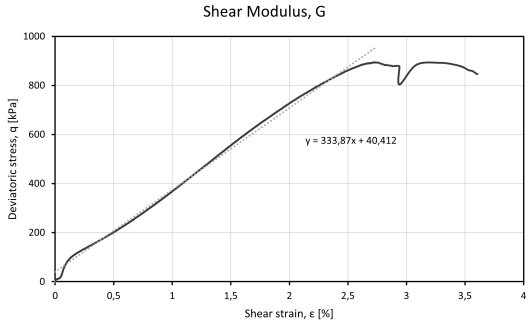

(a) Sand 0% Al-OM flocs serie 1.

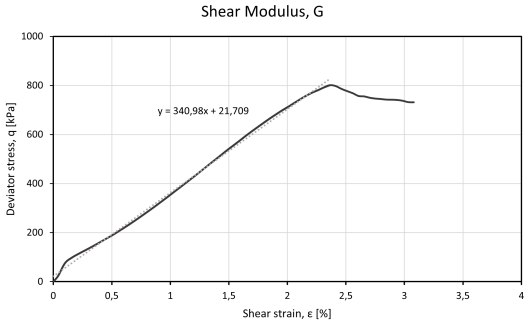

(b) Sand 0% Al-OM flocs serie 2.

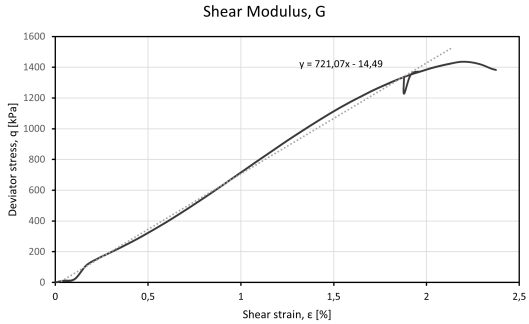

(c) SoSEAL 0.1% Al-OM flocs serie 1.

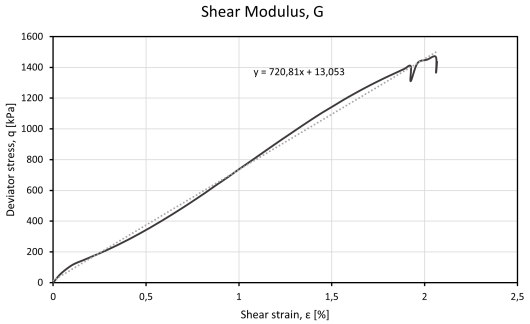

(d) SoSEAL 0.1% Al-OM flocs serie 2.

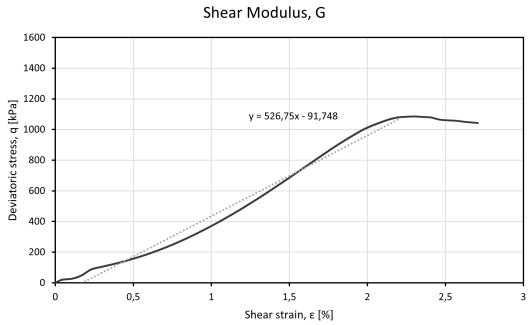

(e) SoSEAL 0.5% Al-OM flocs serie 1.

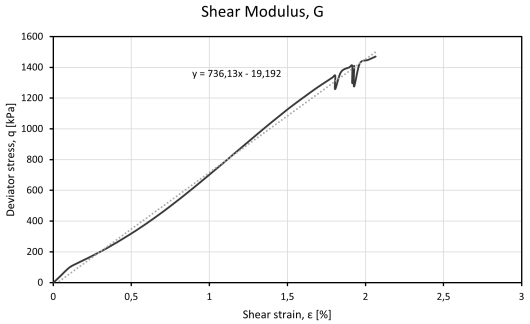

(f) SoSEAL 0.5% Al-OM flocs serie 2.

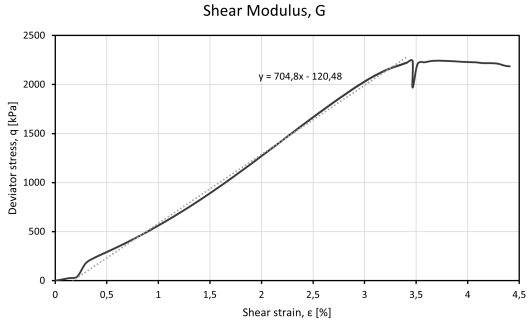

(g) SoSEAL 1% Al-OM flocs serie 1.

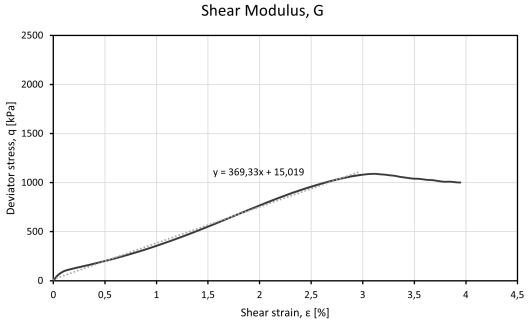

(h) SoSEAL 1% Al-OM flocs serie 2.

Figure D.3: Derivation of the shear Modulus, G, from the shearing phase of the triaxial test series.

E

Derivation of strength parameters

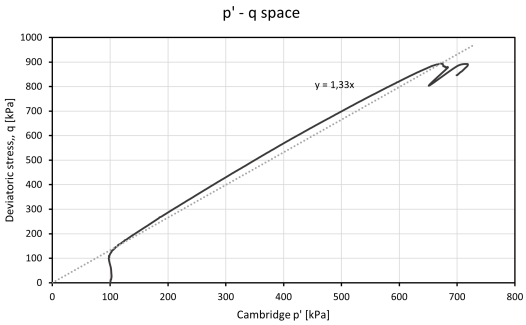

(a) Sand 0% Al-OM flocs serie 1.

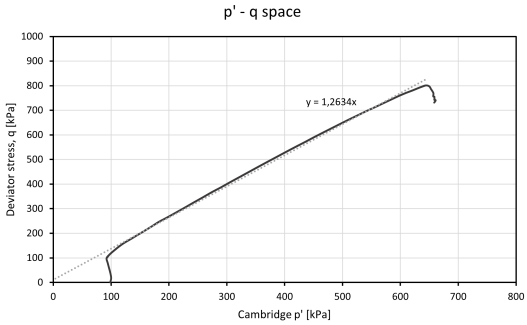

(b) Sand 0% Al-OM flocs serie 2.

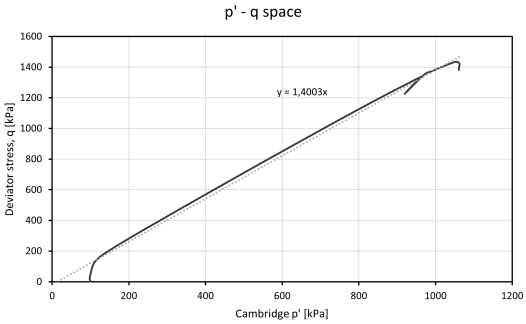

(c) SoSEAL 0.1% Al-OM flocs serie 1.

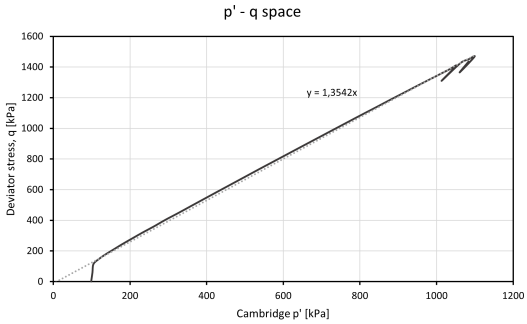

(d) SoSEAL 0.1% Al-OM flocs serie 2.

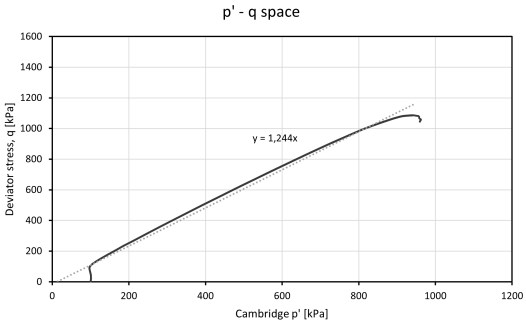

(e) SoSEAL 0.5% Al-OM flocs serie 1.

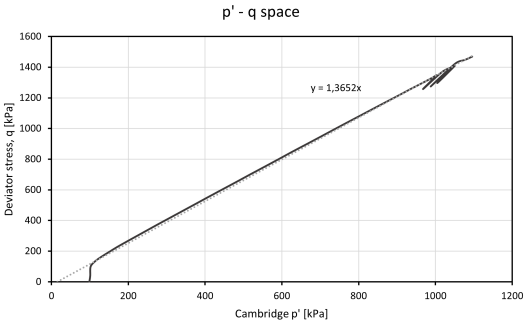

(f) SoSEAL 0.5% Al-OM flocs serie 2.

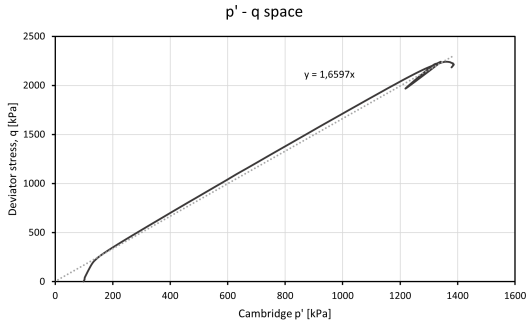

(g) SoSEAL 1% Al-OM flocs serie 1.

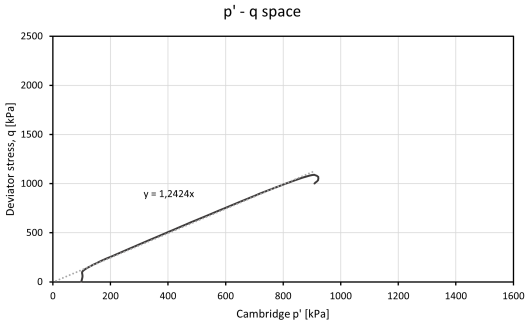

(h) SoSEAL 1% Al-OM flocs serie 2.

Figure E.1: Derivation of the Critical State Parameters, from the shearing phase of the triaxial test series.

F

Circles of Mohr

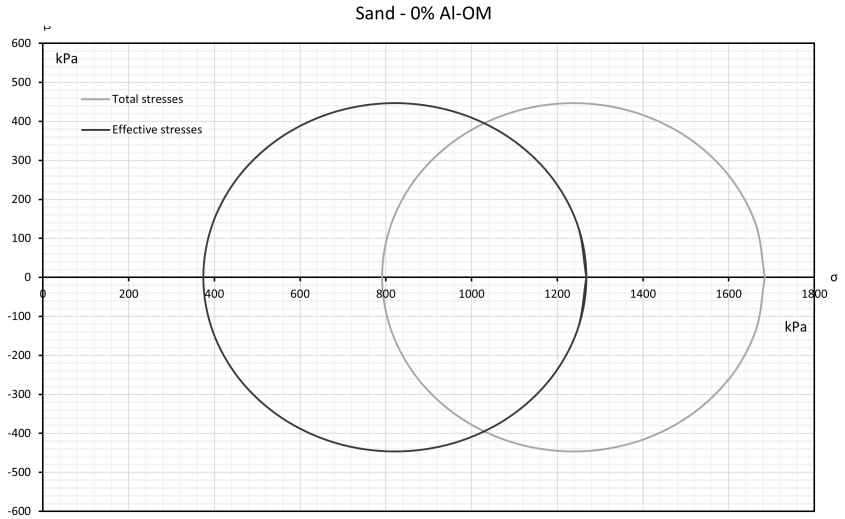

Figure F.1: Effective and total stress circle of Mohr; sand 0% Al-OM flocs from triaxial test series 1.

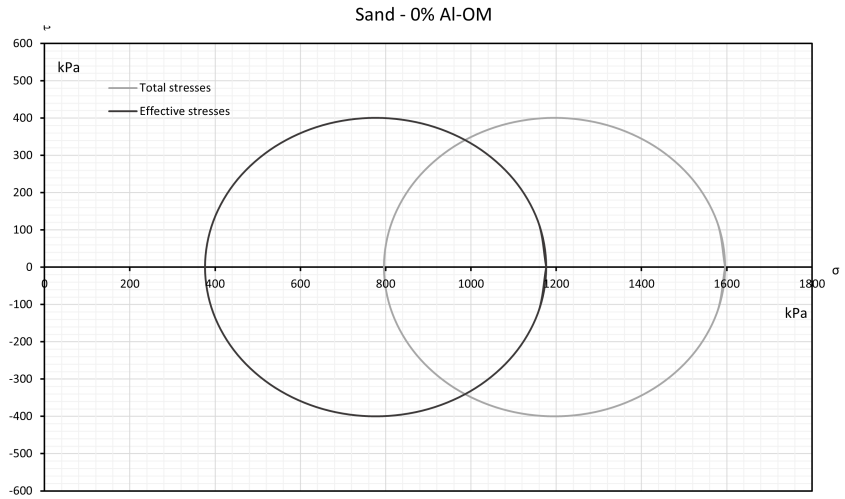

Figure F.2: Effective and total stress circle of Mohr; sand 0% Al-OM flocs from triaxial test series 2.

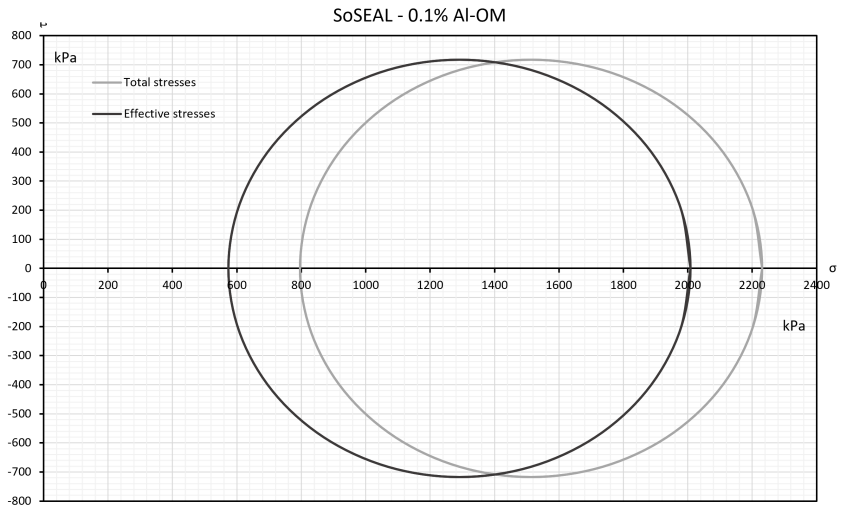

Figure F.3: Effective and total stress circle of Mohr; SoSEAL 0.1% Al-OM flocs from triaxial test series 1.

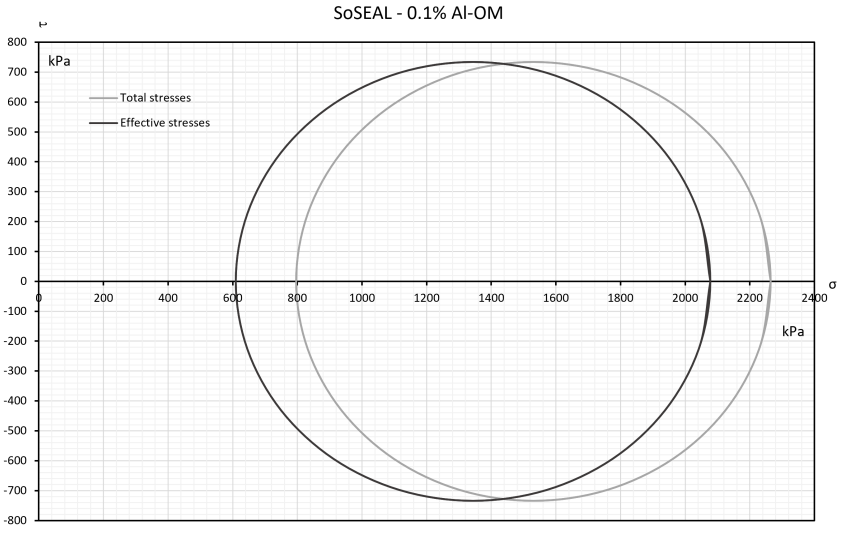

Figure F.4: Effective and total stress circle of Mohr; SoSEAL 0.1% Al-OM flocs from triaxial test series 2.

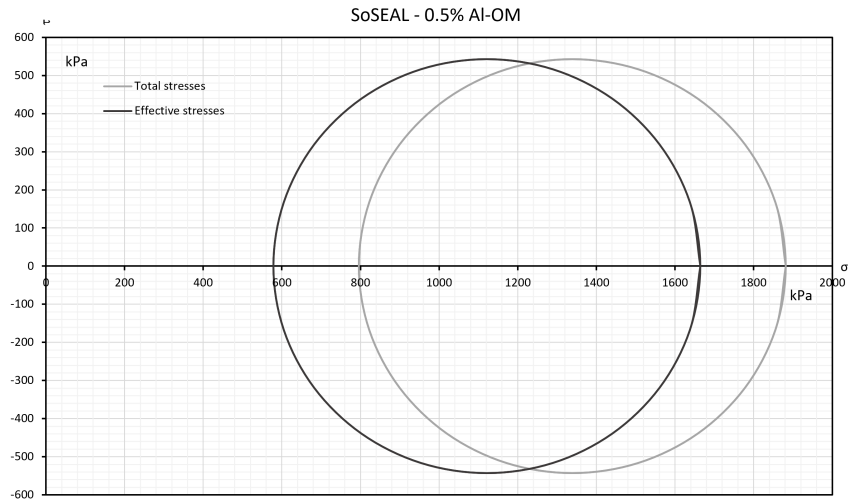

Figure F.5: Effective and total stress circle of Mohr; SoSEAL 0.5% Al-OM flocs from triaxial test series 1.

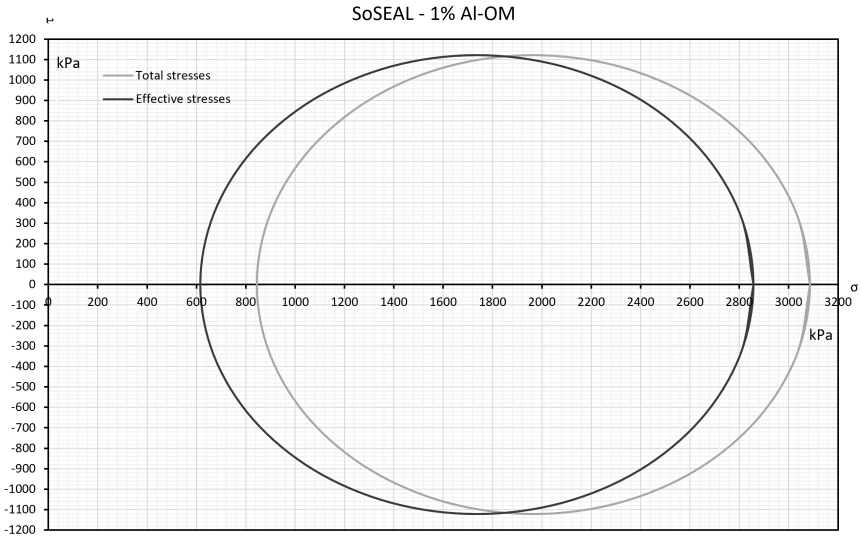

Figure F.6: Effective and total stress circle of Mohr; SoSEAL 1% Al-OM flocs from triaxial test series 1.

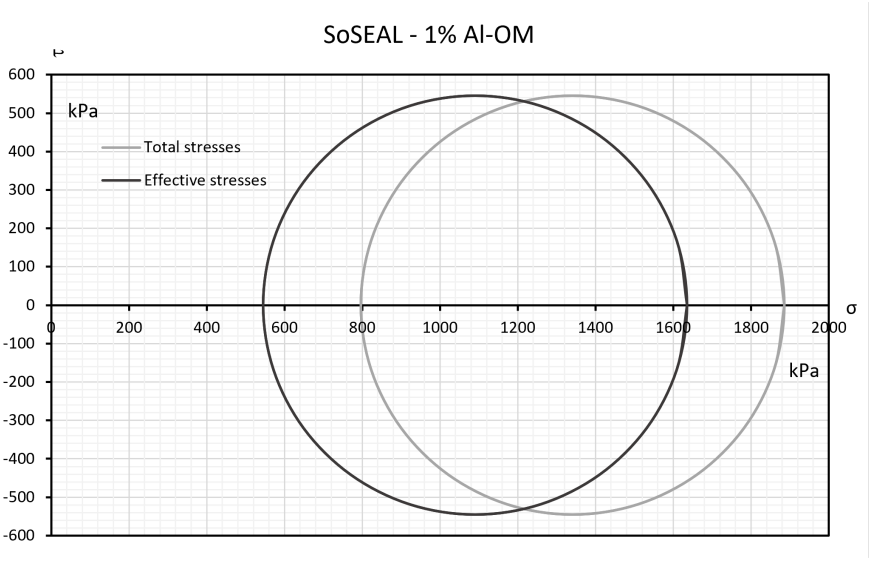

Figure F.7: Effective and total stress circle of Mohr; SoSEAL 1% Al-OM flocs from triaxial test series 2.

G

Component Distribution

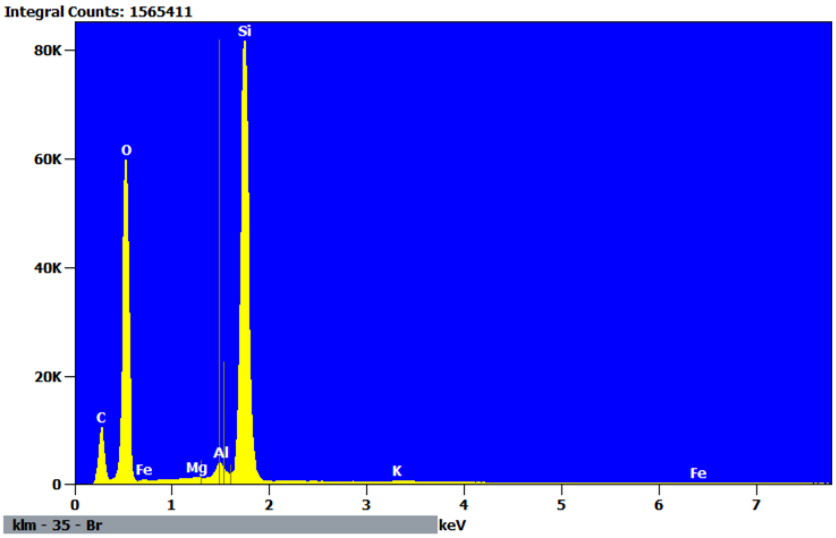

Figure G.1: Component distribution diagram of sand with 0% Al-OM flocs.

Element	**Weight %**	**Weight % error**	**Norm. Wt. %**	**Norm. Wt. % Err**	**Atom %**	**Atom % Error**	**Formula**	**Compnd %**
C	13.66	±0.07	13.66	±0.07	20.18	±0.22	C	13.66
O	53.14	±0.26	53.14	±0.26	58.94	±0.57	O	53.14
Mg	0.07	±0.01	0.07	±0.01	0.05	±0.01	Mg	0.07
Al	0.98	±0.02	0.98	±0.02	0.65	±0.02	Al	0.98
Si	31.69	±0.11	31.69	±0.11	20.02	±0.14	Si	31.69
K	0.12	±0.01	0.12	±0.01	0.06	±0.01	K	0.12
Fe	0.33	±0.06	0.33	±0.06	0.10	±0.04	Fe	0.33
Total	100		100		100			100

Table G.1: Component distribution of sand with 0% Al-OM flocs.

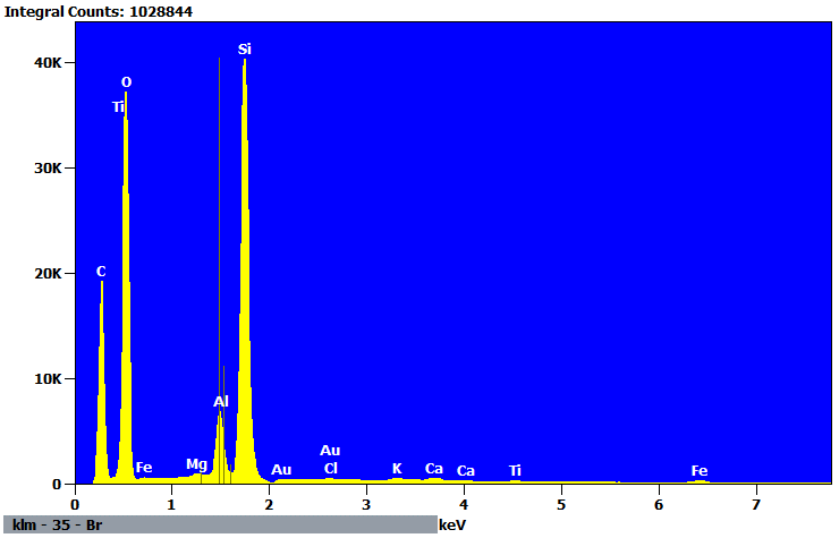

Figure G.2: Component distribution diagram of SoSEAL with 0.1% Al-OM flocs.

Element	Weight %	Weight % error	Norm. Wt. %	Norm. Wt. % Err	Atom %	Atom % Error	Formula	Compnd %
C	25.13	±0.13	25.13	±0.13	34.68	±0.36	C	25.13
O	48.50	±0.25	48.50	±0.25	50.25	±0.51	O	48.50
Mg	0.16	±0.02	0.16	±0.02	0.11	±0.02	Mg	0.16
Al	2.88	±0.03	2.88	±0.03	1.77	±0.03	Al	2.88
Si	21.26	±0.07	21.26	±0.07	12.55	±0.09	Si	21.26
Cl	0.12	±0.01	0.12	±0.01	0.05	±0.01	Cl	0.12
K	0.24	±0.02	0.24	±0.02	0.10	±0.02	K	0.24
Ca	0.38	±0.03	0.38	±0.03	0.16	±0.02	Ca	0.38
Ti	0.15	±0.02	0.15	±0.02	0.05	±0.01	Ti	0.15
Fe	0.83	±0.07	0.83	±0.07	0.35	±0.04	Fe	0.83
Au	0.35	±0.04	0.35	±0.04	0.03	±0.01	Au	0.35
Total	100		100		100			100

Table G.2: Component distribution of SoSEAL with 0.1% Al-OM flocs.

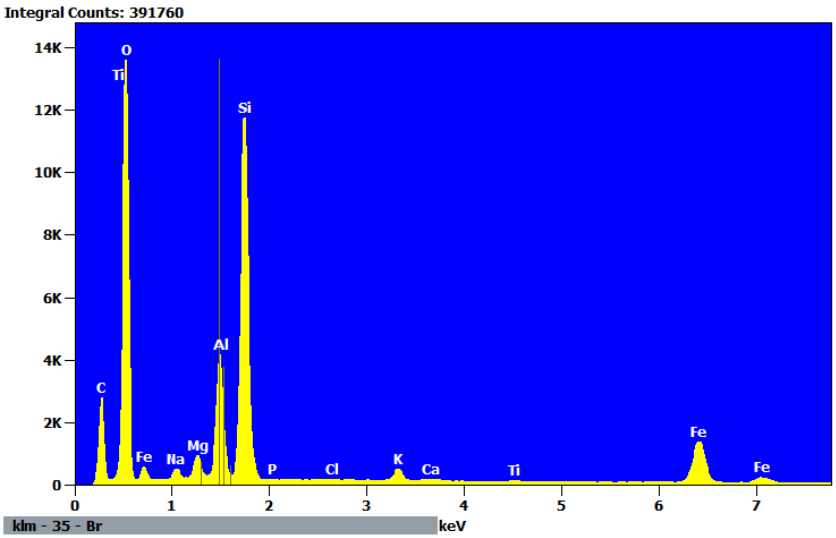

Figure G.3: Component distribution diagram of SoSEAL with 0.5% Al-OM flocs.

Element	Weight %	Weight % error	Norm. Wt. %	Norm. Wt. % Err	Atom %	Atom % Error	Formula	Compnd %
C	11.38	±0.09	11.38	±0.09	19.57	±0.32	C	11.38
O	40.04	±0.24	40.04	±0.24	51.67	±0.61	O	40.04
Na	0.78	±0.04	0.78	±0.04	0.70	±0.07	Na	0.78
Mg	1.21	±0.03	1.21	±0.03	1.02	±0.05	Mg	1.21
Al	6.01	±0.06	6.01	±0.06	4.60	±0.09	Al	6.01
Si	19.57	±0.10	19.57	±0.10	14.38	±0.14	Si	19.57
P 0.13	±0.02	0.13	±0.02	0.09	±0.02	P	0.13	
Cl	0.13	±0.02	0.13	±0.02	0.08	±0.02	Cl	0.13
K	1.16	±0.02	1.16	±0.02	0.61	±0.03	K	1.16
Ca	0.24	±0.02	0.24	±0.02	0.12	±0.02	Ca	0.24
Ti	0.16	±0.03	0.16	±0.03	0.07	±0.03	Ti	0.16
Fe	19.20	±0.27	19.20	±0.27	7.10	±0.20	Fe	19.20
Total	100		100		100			100

Table G.3: Component distribution of SoSEAL with 0.5% Al-OM flocs.

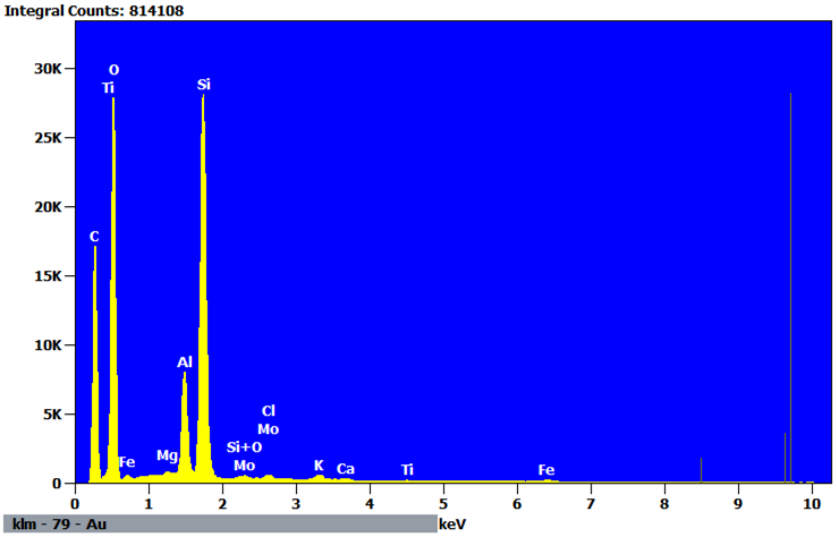

Figure G.4: Component distribution diagram of SoSEAL with 1% Al-OM flocs.

Element	Weight %	Weight % error	Norm. Wt. %	Norm. Wt. % Err	Atom %	Atom % Error	Formula	Compnd %
C	27.22	±0.14	27.22	±0.14	37.33	±0.39	C	27.22
O	46.44	±0.24	46.44	±0.24	47.80	±0.50	O	46.44
Mg	0.12	±0.01	0.12	±0.01	0.08	±0.02	Mg	0.12
Al	4.56	±0.03	4.56	±0.03	2.78	±0.04	Al	4.56
Si	18.99	±0.07	18.99	±0.07	11.13	±0.09	Si	18.99
Cl	0.33	±0.02	0.33	±0.02	0.15	±0.02	Cl	0.33
K	0.42	±0.01	0.42	±0.01	0.18	±0.01	K	0.42
Ca	0.18	±0.01	0.18	±0.01	0.07	±0.01	Ca	0.18
Ti	0.16	±0.03	0.16	±0.03	0.07	±0.03	Ti	0.16
Fe	1.13	±0.09	1.13	±0.09	0.33	±0.05	Fe	1.13
Mo	0.40	±0.04	0.40	±0.04	0.07	±0.01	Mo	0.40
Total	100		100		100			100

Table G.4: Component distribution of SoSEAL with 1% Al-OM flocs.